ABSTRACT

N_8^- POLYNITROGEN STABILIZED ON CARBON-BASED SUPPORTS AS METAL-FREE ELECTROCATALYST FOR OXYGEN REDUCTION REACTION IN FUEL CELLS

by
Zhenhua Yao

The sluggish oxygen reduction reaction (ORR) kinetics at the cathode is one of the key factors limiting the performance of polymer electrolyte membrane fuel cell (PEMFC). Platinum-based materials are the most widely studied catalysts for this ORR reaction while their large-scale practical application in fuel cells is hindered due to their scarcity and low stability. Therefore, highly active, low cost and robust non-Pt catalysts are being developed to overcome the drawbacks. Recently, a novel polynitrogen N_8^- (PN) stabilized on multiwall carbon nanotube (MWNT) was synthesized under ambient condition for the first time by our group and demonstrated high ORR activities. It is promising for replacing platinum-based catalysts. However, the substrate effect was not covered in our previous work. Moreover, the PN synthesis mechanism and its catalytic properties for ORR and ORR mechanisms are still not fully understood.

The main objectives of this research are to investigate the catalytic properties of PN on different carbon-based substrates, to identify the active sites and mechanisms of ORR, and eventually to provide guidelines for optimizing the synthesis of PN-series catalysts as well as increasing the efficiency of ORR.

Polynitrogen N_8^- (PN) deposited on multiwalled carbon nanotubes (PN-MWNT) are synthesized by cyclic voltammetry (CV) with UV irradiation and further used for oxygen reduction reaction (ORR). Compared to the sample synthesized without UV, a

larger amount of N_8^- is synthesized and is found to distribute more uniformly on MWNT with 254nm UV irradiation (PN-MWNT-254nm); this indicates the production of more azide radicals as the precursors for synthesis of N_8^- by photoexcitation of azide ions is a rate-limiting step for PN synthesis. The PN-MWCNT-254nm sample shows higher ORR current density than that from a commercial Pt catalyst. Kinetic studies indicate a four-electron pathway on N_8^- while a two-electron one on N_3^- . *In situ* Shell-Isolated Nanoparticle-Enhanced Raman Spectroscopy (SHINERS) analysis reveals that the side-on and end-on O_2 adsorption occurs at N_8^- and N_3^-, respectively, confirming the electron transfer process. Calculation results from natural bonding orbital (NBO) analysis are used to identify the possible active sites for oxygen chemisorption and further clarify the ORR mechanism.

PN deposited on graphene (G), nitrogen-doped graphene (NG) and boron-doped graphene (BG) are synthesized experimentally. The formation of PN on G, NG and BG is confirmed by ATR-FTIR and temperature-programmed desorption (TPD). Moreover, a larger amount of N_8^- is obtained on NG and BG substrates than that over pure G. Electrochemical tests show that PN-NG and PN-BG possess superior activity toward the ORR and favored a four-electron pathway.

This work provides facile strategies to efficiently synthesize PN under ambient condition and deep understanding of its intrinsic oxygen reduction activity.

N_8^- POLYNITROGEN STABILIZED ON CARBON-BASED SUPPORTS AS METAL-FREE ELECTROCATALYST FOR OXYGEN REDUCTION REACTION IN FUEL CELLS

by
Zhenhua Yao

A Dissertation
Submitted to the Faculty of
New Jersey Institute of Technology
in Partial Fulfillment of the Requirements for the Degree of
Doctor of Philosophy in Chemical Engineering

Otto H. York Department of Chemical and Materials Engineering

May 2019

.

APPROVAL PAGE

N_8^- POLYNITROGEN STABILIZED ON CARBON-BASED SUPPORTS AS METAL-FREE ELECTROCATALYST FOR OXYGEN REDUCTION REACTION IN FUEL CELLS

Zhenhua Yao

Dr. Xianqin Wang, Dissertation Advisor Associate Professor of Chemical and Materials Engineering, NJIT	Date
Dr. Zafar Iqbal, Committee Member Research Professor of Chemistry and Environmental Science, NJIT	Date
Dr. Edward L. Dreyzin, Committee Member Distinguished Professor of Chemical and Materials Engineering, NJIT	Date
Dr. Kamalesh K. Sirkar, Committee Member Distinguished Professor of Chemical and Materials Engineering, NJIT	Date
Dr. Xiaoyang Xu, Committee Member Assistant Professor of Chemical and Materials Engineering, NJIT	Date

BIOGRAPHICAL SKETCH

Author: Zhenhua Yao

Degree: Doctor of Philosophy

Date: May 2019

Undergraduate and Graduate Education:

- Doctor of Philosophy in Chemical Engineering,
  New Jersey Institute of Technology, Newark, NJ, 2019

- Master of Science in Industrial Catalysis,
  Tianjin University, Tianjin, P. R. China, 2007

- Bachelor of Science in Applied Chemistry,
  Baoji University of Arts and Sciences, Baoji, P. R. China, 2004

Major: Chemical Engineering

Presentations and Publications:

M. Hu, Z. Yao, L. Ma, Z. He, X. Wang, The role of hydroxyapatite in TiO_2/ hydroxyapatite catalyst for photocatalytic degradation of gaseous formaldehyde, J. Taiwan Inst. Chem. Engrs., 85(2018) 91-97.

M. Hu, Z. Yao, X. Wang, Graphene-based nanomaterials for catalysis, Ind. Eng. Chem. Res., 56 (2017) 3477-3502.

M. Hu, Z. Yao, L. Li, YH. Tsou, L. Kuang, X. Xu, W. Zhang, X. Wang, Boron-doped graphene nanosheet-supported Pt: a highly active and selective catalyst for low temperature H_2-SCR, Nanoscale 10 (2018), 10203-10212.

M. Hu, Z. Yao, K. Hui, K. Hui, Novel mechanistic view of catalytic ozonation of gaseous toluene by dual-site kinetic modeling, Chem. Eng. J., 308 (2017) 710-718.

EM. Benchafia, Z. Yao, G. Yuan, T. Chou, H. Piao, X. Wang, Z Iqbal, Cubic gauche polymeric nitrogen under ambient conditions, Nat. Commun., 8 (2017) 930-936.

Z. Yao, M. Hu, Z. Iqbal, X. Wang, N_8^- Polynitrogen stabilized on boron doped graphene as metal-free electrocatalysts for oxygen reduction reaction, Applied Catalysis B, under review.

Z. Yao, X. Wang, Support effects on nanocatalysts for clean energy production, to be submitted.

Z. Yao, Z. Wu, M. Hu, M. Benchafia, Z. Iqbal, X. Wang, N_8^- synthesis with UV irradiation and its high activity for oxygen reduction, to be submitted.

Z. Yao, M. Hu, Z. Iqbal, X. Wang, The role of doped-nitrogen for stabilizing N_8^- polynitrogen and its high performance for oxygen reduction reaction, to be submitted.

Z. Yao, M. Hu, X. Wang, Pt/B-graphene catalyst for low temperature H_2-SCR, Oral Presentation at the 254th ACS National Meeting, Washington, D.C., August 2017.

M. Hu, Z. Yao, L. Ma, Z. He, X. Wang, The role of hydroxyapatite in TiO_2/ hydroxyapatite catalyst for photocatalytic degradation of gaseous formaldehyde, Poster at the Annual Symposium of Catalysis Society of Metropolitan New York, NY, March 2017

Dedicated to my beloved husband, Maocong Hu, handsome son, Jia Hu, and lovely daughter, Jiayi Hu

谨以此文献给我的丈夫胡茂从，儿子胡嘉和女儿胡佳伊

ACKNOWLEDGMENT

I would like to express my deepest gratitude to my advisor, Dr. Xianqin Wang for giving me a golden opportunity to pursue Ph.D. research in her lab to fulfill my dream. I would also like to thank her for invaluable assistance, motivation, advice and guidance throughout my graduate studies.

I would like to thank the members of my committee, Dr. Zafar Iqbal, Dr. Edward L. Dreyzin, Dr. Kamalesh K. Sirkar and Dr. Xiaoyang Xu, for their time reading my dissertation, attending my defense, and providing valuable comments. Special thanks go to Dr. Iqbal and Dr. Xu, for their generous support on instrument usage.

This work was supported NSF CBET-1804949 grant. I would also like to thank the Department of Chemical and Materials Engineering for the financial support during my graduate studies.

I would like to thank the staff, especially Shawn Yetman, at NJIT for his technical support and valuable discussions. I would like to thank Ms. Laying Wu at Montclair State University for her great help on the SEM&TEM measurements. I would like to thank Dr. Ryan Thorpe at Rutgers University for his help on XPS data collection.

My thanks to my past and current group members, Zhiyi Wu, Sherry-Ann Tim Kee, Basil Rawah, and Maocong Hu for their help and companionship. I am also grateful to Yung-Hao Tsou, He Zhu, Zhongyu Li, EI Mostafa Benchafia and Biao Leng for their help and companionship in my graduate studies.

Last, but not least, my deepest thank to my parents, Jiqing Yao and Sanrong Zhang, for their love, support, and sacrifice throughout my life.

TABLE OF CONTENTS

TABLE OF CONTENTS
(Continued)

TABLE OF CONTENTS
(Continued)

LIST OF TABLES

LIST OF FIGURES

LIST OF FIGURES
(Continued)

LIST OF FIGURES
(Continued)

CHAPTER 1

INTRODUCTION

1.1 Background

The growing global energy demand and environmental impact of fossil energy resources has led to energy security and global climate change issues [1, 2]. Fuel cell is one promising solution owing to its high efficiency in energy conversion and low emission of pollutants [3]. Among several types of fuel cells, polymer electrolyte membrane fuel cell (PEMFC) has been considered as one of the most promising alternative technologies for both automotive and stationary applications [4, 5]. Two types of electrochemical reactions occur at the electrodes of PEMFC, hydrogen oxidation reaction (HOR, Equation 1.1) occurs at the anode while oxygen reduction reaction (ORR, Equation 1.2) occurs at the cathode. The relatively sluggish kinetics of oxygen reduction reaction (ORR) is regarded as one of the key factors that limits the performance of PEMFC.

$$Anode \qquad 2H_2 \rightarrow 4H^+ + 4e^- \qquad (1.1)$$

$$Cathode \qquad O_2 + 4H^+ + 4e^- \rightarrow 2H_2O \qquad (1.2)$$

To date, platinum-based materials are known as the most active catalysts for ORR [6, 7]. However, Pt is scarcely available and costly, and is subjective to be poisoned and deactivated by methanol and CO, which hinder its large-scale practical application in fuel cells [8, 9]. Therefore, the development of low cost non-Pt ORR catalysts with high performance is of great interest for the commercialization of fuel cells [7, 10]. As an alternative candidate, nonprecious metal catalysts, such as Fe-, Co-, Cu-, and Ni-based materials, were developed for this purpose [11]. However, challenges still remain on

improving their activities and stabilities to meet the requirement for practical applications. Moreover, metal (i.e., active species) leaching during usage is inevitable in the liquid phase reaction environment of PEMFC for these catalysts as well as for Pt. The pursuit of more efficient, more durable and less costly ORR catalysts will continue to be pursued.

Along with the intensive research efforts in developing nonprecious metal ORR catalysts, a new class of metal-free, carbon-based materials with abundant free flowing electrons and large surface area, such as heteroatom doped carbon nanotubes (CNT) and graphene, have been recently discovered, these alternative ORR catalysts could dramatically increase the efficiency and reduce the cost of fuel cells [12]. Moreover, the active phase leaching issue was overcome due to the characteristic doping structure of the active sites in the carbon substrates of these catalysts. Consequently, considerable efforts have been directed toward the development of metal-free carbon materials for oxygen reduction reaction.

1.1.1 N-doped carbon materials

Nitrogen-doped carbon materials (NCMs) such as carbon nanotubes (CNTs) [12, 13], graphene [14-16], mesoporous carbon [17, 18], and carbon fibers [19, 20] have been reported to exhibit excellent electrocatalytic activity and high durability for ORR due to their unique electronic properties [12, 13]. Moreover, the NCMs possess strong tolerance to CO poisoning and show long-term operational stability [12, 21]. The explosion of interest in this topic started in 2009, Gong *et al.* for the first time reported that vertically aligned nitrogen-doped CNTs (i.e., VA-NCNTs, Figure 1.1a) could act as extremely effective metal-free ORR catalysts with much higher electrocatalytic activities (Figure 1.1b), lower overpotential, long-term operation stability and smaller methanol crossover

effect than that of a commercial Pt/C catalyst (20% platinum on Vulcan XC-72R) [12]. The rotating ring-disk electrode (RRDE) voltammograms results (electrochemical performance evaluation) are shown in Figure 1.1b. The nitrogen-doped CNT electrode (VA-NCNT/GC) exhibited a steady-state diffusion current of ORR that was almost twice of that obtained at the nitrogen-free CNT electrode (VA-CCNT/GC). The onset potential was -0.08V and the current density was 4.1mA/m^2 for VA-NCNT/GC, compared with -0.085V and 1.1mA/m^2 for Pt-C/GC. Thus, the VA-NCNT/GC electrode is much better than both the Pt-C/GC and VA-CCNT/GC electrodes for ORR. Furthermore, they used density functional theory (DFT) calculations to identify the active sites for ORR. The results indicated that charge transfer interactions between nitrogen and adjacent carbon atoms led to the high ORR activity. Due to the stronger electronic affinity of nitrogen compared to carbon, the carbon atoms adjacent to nitrogen dopants possessed a high positive charge density (Figure 1.1c). And this nitrogen-induced charge delocalization changed the chemisorption mode of O_2 from the end-on adsorption (Pauling model) at the nitrogen-free CNT (CCNT) surface (top, Figure 1.1d) to a side-on adsorption (Yeager model) at the NCNT electrode surface (bottom, Figure 1.1d) [12]. The side-on adsorption could effectively weaken the O-O bonding, which led to a four-electron transfer pathway, and finally facilitated oxygen reduction [22, 23].

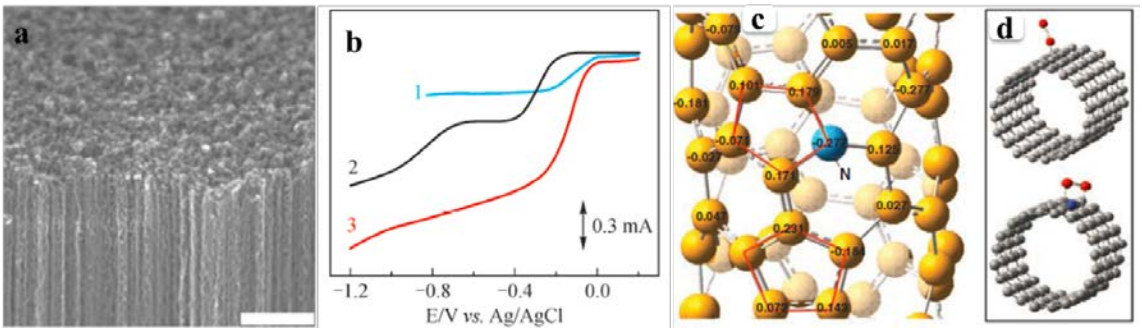

Figure 1.1(a) SEM image of the as-synthesized VA-NCNTs on a quartz substrate. (b) ORR performance of the Pt-C/GC (curve 1), VA-CCNT/GC (curve 2), and VA-NCNT/GC (curve 3) electrodes. (c) Calculated charge density distribution for the NCNTs. (d) Schematic representations of possible adsorption modes of an oxygen molecule at the CCNTs (top) and NCNTs (bottom).
Source: [12].

Following this pioneering work, different approaches were developed to fabricate NCNTs and investigate their electrocatalytic activity [21, 24-26]. Nagaiah *et al.* [24] synthesized nitrogen-doped CNTs (NCNTs) by treating HNO_3-oxidized CNTs (OCNTs) in NH_3 flow at different temperatures (200°C, 400°C, 600°C, 800°C) for 6h. NCNTs treated at 800 °C showed improved electrocatalytic activity for oxygen reduction including positive onset potential and increased reduction currents as compared with commercially available Pt/C catalysts. Tang *et al.* [25] synthesized NCNTs via the chemical vapor deposition (CVD) at 950 °C using methyl cyanide, ethanol, and ferrocene as liquid precursors and Ar/H_2 as carrier gases. TEM images revealed that the NCNTs were composed of individual nanocups stacked together to form long nanofibers. The cyclic voltammetry (CV) results of ORR indicated that the stacked NCNTs exhibited similar catalytic activity with Pt/CNTs in ORR, the NCNTs' reduction process was a combination of two-electron and four-electron pathways while Pt/CNTs follow a four-electron pathway. Yang *et al.* [21] prepared NCNTs by directly annealing oxidized CNTs and

tripyrrolyl[1,3,5]triazine (TPT) mixture in nitrogen. Their results indicated that nitrogen can be doped into CNT sidewall in the form of pyridinic-N, pyrrolic-N, graphitic-N, and oxidized-N. Moreover, the NCNT-900 (annealed at 900 °C) which possessed the highest graphitic-N content showed superior electrocatalytic performance, long durability and excellent methanol tolerance for ORR.

As the mother form of all graphitic materials, graphene is a building block for carbon materials of all other dimensionalities. Superior to CNTs, the one atomic-thick graphene sheets with a two-dimensional (2D) planar geometry will further facilitate electron transport, and make it an attractive candidate as a metal-free ORR catalyst [14, 27]. Qu *et al*. first reported the use of nitrogen-doped graphene (N-graphene) as metal-free catalysts for oxygen reduction [14]. The N-graphene (Figure 1.2a) film was prepared by chemical vapor deposition (CVD) of methane at 1000 °C within a quartz tube, in the presence of ammonia. The rotating ring-disk electrode (RRDE) voltammograms results (Figure 1.2b) indicated that the steady-state catalytic current density at the N-graphene electrode was found to be ca. 3 times higher than that of the Pt/C electrode. The long-term operation stability, tolerance to crossover effect and CO poisoning were also better than that at the Pt/C electrode. Thus, the N-doped graphene electrode is a promising metal-free catalyst for the ORR [14].

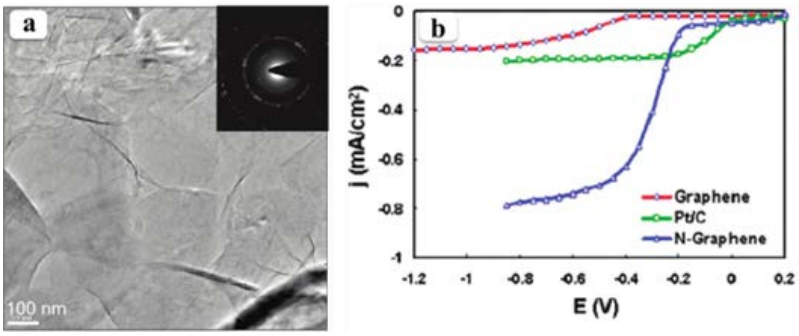

Figure 1.2(a) TEM image of the CVD-grown N-graphene film on a grid. (b) ORR performance of the graphene (red curve), Pt/C (green curve), and N-graphene (blue curve) electrodes.
Source: [14].

After that, numerous research studies had been conducted on NG for ORR. Some of the typical works were summarized in Table 1.1.

Table 1.1 Summary of Nitrogen-doped Graphene (NG) Catalyst for ORR

Synthesis Method and Reactants	N-Content (at.%)	Electrocatalytic Performance	Electron Transfer Number*	Ref.
Thermal treatment of glucose and urea	33	NG shows competitive ORR activities with Pt/C and much better crossover resistance and excellent stability	3.2–3.7	[28]
N plasma treatment on graphene	8.5	Higher ORR activity than graphene, and higher durability and selectivity than Pt/C	-	[29]
Covalent functionalize GO using organic molecules and thermal treatment	0.72–4.3	The NG nanosheet exhibited a good electrocatalytic activity through an efficient 4e- pathway	3.63	[30]
CVD of N-containing aromatic precursor molecules	2.0–2.7	The N dopants in the graphene reduce the ORR overpotential, thereby enhancing the catalytic activity	3.5–4.0	[31]
GO treatment by ammonia hydroxide, heating under ammonia gas, and reaction with melamine	6.0–6.8	Pyridinic N plays a vital role in ORR	3.2–3.7	[32]
Annealing of GO with ammonia and N-containing polymers	2.91–7.56	The higher limiting current density compared to Pt	2.85–3.65	[16]
Hydrothermal process using urea and holey GO	8.6	Superb ORR with 4e- pathway and excellent durability	3.85	[33]

Table 1.1 Summary of Nitrogen-doped Graphene (NG) Catalyst for ORR (Continued)

Synthesis Method and Reactants	N-Content (at.%)	Electrocatalytic Performance	Electron Transfer Number*	Ref.
Thermally annealing GO with melamine	8.05	The nG-900 exhibits lower activity and onset potential than Pt/C, albeit higher than graphene; excellent stability	3.3–3.7	[34]
Redox GO with pyrrole then thermal treatment	6	Shows comparable onset potentials with Pt/C	3.3	[35]
Pyrolysis of graphene oxide and polyaniline	2.4	High activity toward ORR with a superior long-term stability and tolerance to methanol crossover	3.8–3.9	[36]
Pyrolysis of GO and polydopamine	2.78–3.79	Much more enhanced ORR activities with positive onset potential and larger current density than graphene	3.89	[37]
Microwave heating of graphene under NH_3 flow	4.05–5.47	The doping of graphite N enhanced the activity of the catalysts in the ORR	3.03–3.3	[38]
CVD growth of graphene and post-doping with a solid N precursor of graphitic C_3N_4	6.5	Excellent activity, high stability, and very good crossover resistance for ORR	3.96-4.05	[39]

* is the number of electrons transferred per oxygen molecule in the oxygen reduction reaction.

The reported results showed that the electrocatalytic activity of the nitrogen-doped carbon materials (NCMs) was mainly dependent on the forms of the doped nitrogen atoms [16, 24, 40]. Different doping forms were shown in Figure 1.3 [41, 42], including pyridinic-N, pyrrolic-N, quaternary-N (or graphitic-N) and N-oxides of pyridinic N. Several research groups reported that the pyridinic N, which possessed one lone pair of electrons in addition to the one p electron donated to the aromatic π system, facilitated O_2 adsorption and was the active site to enhance the ORR [40]. However, some other studies suggested that more graphitic nitrogen rather than the pyridinic ones favored ORR [24, 43, 44]. In Nagaiah *et al.*'s work, XPS studies and polarization curves revealed that the quaternary nitrogen played an important role for the enhanced activity of ORR [24], which was consistent with Liu's results [44]. Kim's group investigated ORR at the edge of a

graphene nanoribbon (GNR) by the periodic density functional theory (DFT) calculations and pointed out that the outermost graphitic nitrogen site in particular gave the most desirable characteristics for improved ORR activity, and hence the active site [43]. Even though pyridinic nitrogen might not be the active site for ORR, it is a marker for edge plane exposure, which contained more defects for facilitating ORR [45, 46]. Lai *et al.* studied the active center structure of nitrogen-doped graphene for ORR and found that the graphitic N content determined the limiting current density while the pyridinic N content improved the onset potential [16]. Although pyrrolic nitrogen was reported to have an insignificant or even a negative effect on ORR for a long time [47, 48], Dai's group suggested that both pyridinic and pyrrolic nitrogen might favor ORR process. Their experimental results and theoretical calculations indicated that both types of nitrogen could induce charge delocalization of the surrounding carbon atoms and then facilitate oxygen chemisorption. Specially, the carbon atoms around pyrrolic nitrogen would have much higher positive charges than those around pyridinic nitrogen [12, 14].

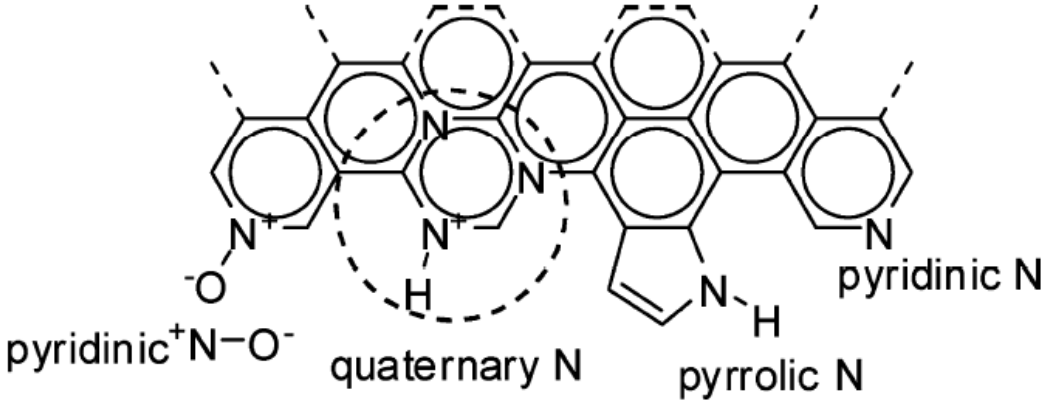

Figure 1.3 Schematic representation of the different nitrogen species in N-graphene.
Source: [42].

Nevertheless, the roles of different types of nitrogen are still controversial. In addition, it is a challenge to precisely control the exact locations of nitrogen atoms in the nanocarbon structures and chemical nature of the catalytic sites of the N-doped nanocarbon electrodes [46]. Therefore, further work needs to be done to optimize the synthesis method for NCMs, as well as to fully understand the relationship of the specific nitrogen species with the ORR performance.

1.1.2 B, P or S-doped carbon materials

As mentioned above, nitrogen doped carbon materials shown enhanced catalytic activity toward ORR due to the N-doping-induced charge transfer mechanism [12]. Inspired by this result, much attention has been paid to the electron-deficient boron dopant [49-53]. Yang *et al.* first reported the ORR on boron doped carbon nanotubes (BCNTs) (Figure 1.4) [53]. BCNTs were synthesized with tunable boron content of 0-2.24 at% by chemical vapor deposition (CVD), using benzene, triphenylborane (TPB), and ferrocene as precursors and catalyst. The experimental results indicated onset potentials shifted positively and the current density increased with increasing boron content. Besides, the ORR was a dominant two-electron pathway on BCNTs. Like NCNTs, the BCNTs catalysts also exhibited excellent stability and immunity towards methanol crossover effect and CO poisoning. Sheng *et al.* synthesized boron doped graphene (BG) via a catalyst-free thermal annealing approach in the presence of boron oxide and found the boron atoms in graphene could act as active sites and activate the O-O bond cleavage. In addition, the BG catalyst showed long-term stability and good CO tolerance superior to that of Pt-based catalysts although its ORR performance was still inferior to the latter [52].

DFT calculations were employed to further understand the electrocatalytic activity of BCNTs [53]. The results indicated that the positively charged boron atom was favorable to capture O_2 molecule, and some π^* electrons in the conjugated system accumulated on the vacant $2P_z$ of boron dopant, then the electrons could easily transfer to the chemisorbed O_2 molecules with boron as a bridge. The transferred charge weakened the O-O bonds and facilitated the ORR on BCNTs. Although the performance of boron doped carbon materials were not yet as good as the commercial Pt/C catalyst, it could be further enhanced by optimizing the synthesis method.

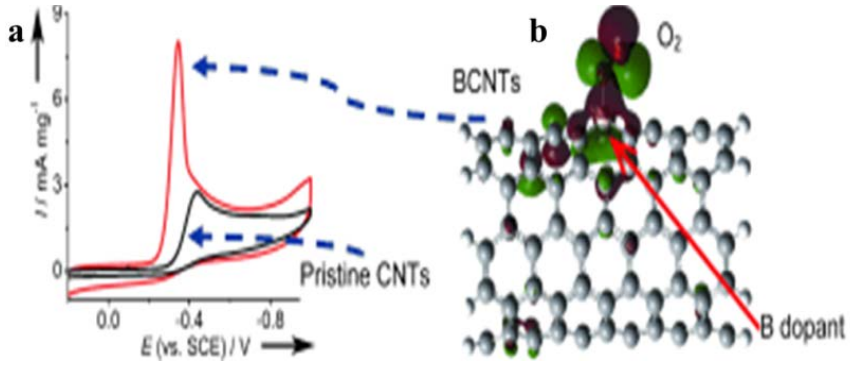

Figure 1.4(a) ORR performance evaluated by CV. (b) Important molecular orbitals involved in the O_2 adsorption on BCNT(5,5).
Source: [53].

Like boron (electronegativity=2.04), phosphorus (electronegativity=2.19) also can be introduced into the carbon (electronegativity=2.55) hexagonal network of graphitic sheets and induce the catalytic activity for ORR. Liu *et al.* first prepared the P-doped graphite layers by pyrolysis of toluene and triphenylphosphine (TPP) [54]. The P-doped graphite/GC electrode exhibited outstanding durability and almost no methanol crossover effect. The onset potential of the P-doped graphite/GC electrode for the ORR was higher than that for the Pt-C/GC electrode at about +0.01 V, whereas the oxygen reduction current densities of the P-doped graphite/GC were lower than those of the Pt–C/GC. Liu *et al.* also

prepared phosphorus-doped carbon nanospheres and phosphorus-doped MWCNTs with good electrocatalytic performance for ORR and DFT calculations suggested the excited electrons in P-doped graphene sheet could transfer much easily to O_2 and significantly quicken the rate of the electrocatalytic ORR [55, 56]. These types of P-doped carbon materials will provide an opportunity to design and develop various metal-free, efficient ORR catalysts for potential applications in fuel cells.

Experimental results and theoretical studies indicated that the different electronegativity between the dopant and the carbon atom would change the electroneutrality of carbon materials to create charged sites, which is favorable for O_2 adsorption and further to enhance ORR performance, regardless of whether the dopant has a higher or lower value of electronegativity than that of C [12, 53, 57]. Thus it would be very interesting to test if S-doped material can induce the ORR activity where the doped element had the similar electronegativity with carbon. The electronegativity of sulfur is 2.58 and the electronegativity of carbon is 2.55. Yang *et al.* synthesized sulfur-doped graphene (S-graphene) through directly annealing graphene oxide (GO) and benzyl disulfide (BDS) in argon [58]. Their results showed that all S-graphene samples had more positive onset potentials and higher limiting current density than those of the corresponding non-doped graphenes. Moreover, onset potential for S-graphene annealed at 1050°C was close to that of the Pt/C catalyst, and its current density (at -0.8 V) was higher than that of Pt/C. Furthermore, S-graphene had a good ability for avoiding crossover effects and superior durability compared with Pt/C. In this case, the doping-induced charge redistribution may contribute insignificantly to the enhanced ORR catalytic activity of S-graphene due to that the electronegativity of sulfur and carbon are nearly the same. It’s

believed that the doping-induced spin density distribution was the dominant factor to regulate the observed ORR activity [58] which was supported by Zhang *et al.*'s report [22]. Their density functional theory (DFT) simulations suggested that the nitrogen doping introduced asymmetry spin density and atomic charge density, as long as the spin density and the electroneutrality of carbon were broken, the high asymmetric spin density and atomic charge density would promote high electrocatalytic activities for the ORR [22]. The detailed relationship between the catalytic activity and the microstructure for the S-graphene needs to be further investigated.

1.1.3 Co-doping carbon materials

Heteroatom doping (N-, B-, P-, S-) carbon materials have shown remarkable performance in oxygen reduction reaction as mentioned above, and two key factors to transform sp^2 carbon into metal-free ORR electrocatalysts by doping are summarized according to the aforementioned experimental results and theoretical calculations: (1) breaking the electroneutrality of sp^2 carbon to create charged sites favorable for O_2 adsorption despite whether the dopants are electron-rich (as N) or electron-deficient (as B); and (2) activating carbon π electrons for effective utilization by O_2 [53]. With this strategy, intuition suggests that co-doping with B and N is a possible route to further optimize the carbon-based metal-free ORR electrocatalysts. Recently some researchers investigated the nitrogen and boron co-doping carbon catalysts for enhancing ORR performance. Ozaki *et al.* first prepared the BN-doped carbons as ORR catalyst and suggested that the higher ORR activity was controlled by the effect of both the edge-N and B-N-C-type moieties in co-doping [59]. Wang *et al.* synthesized vertically aligned BCN (VA-BCN) nanotubes (vertically aligned carbon nanotubes VA-CNTs doped with B and N) and found that

VA-BCN NTs showed significantly improved electrocatalytic activity (e.g., current density) for the oxygen reduction reaction compared to undoped VA-CNTs, and VA-CNTs doped with only B or N (VA-BCNT, VA-NCNT), which could be attributed to a synergetic effect resulted from co-doping of CNTs with boron and nitrogen. In addition, the VA-BCN nanotubes electrode showed an even more positive half-wave potential and higher diffusion current density in LSV curves compared to the Pt/C electrode. Moreover, the VA-BCN nanotube electrode exhibited better tolerance to methanol and carbon monoxide and more excellent durability for ORR performance than a commercial Pt/C electrode [60]. Zhao *et al.* further investigated the B and N co-doping effect, the results indicated that the separated B and N co-doping could activate π electrons and enhance the ORR activity, whereas bonded B and N caused neutralization of the extra electron from N and the vacant orbitals from B, leading to poor ORR performance [61].

Like B-N dually doped [60, 61] metal-free electrocatalysts for ORR, S-N-co-doped, P-N-co-doped, halogen-N-co-doped and halogen-P-co-doped carbon material had also attracted attention of numerous researchers [62-72]. Although the synergistic effects were observed for the enhancement of ORR performance, the mechanisms of the catalytic processes and optimizations of the co-doping strategies for improving ORR performance are still incomplete, which need to be further explored.

1.1.4 Polynitrogen (PN) stabilized on carbon nanotube

Polynitrogen (PN) compounds have attracted much attention due to their potential use as a high energetic material. Although many possible stable structures have been predicted by theoretical calculations, few reports on experimental detection of PN have been published, while they are either short-lived or can only be synthesized under harsh conditions.

Theoretical calculations suggested that a polymeric nitrogen chain N_8 could be stabilized in a carbon nanotube under ambient conditions by a charge transfer interactions between the nitrogen chain and the carbon nanotube (Figure 1.5a) [73]. Hirshberg *et al.* predicted that N_8 species alone could exist under ambient conditions without substrates [74]. Recently, our group firstly synthesized PN (N_8^-) on a positively charged sidewalls of multi-walled carbon nanotube (MWNT) sheet substrate under ambient conditions using cyclic voltammetry (CV) and used it for ORR (Figure 1.5b). Fourier transform infrared spectroscopy (FTIR), Raman spectroscopy and temperature-programmed decomposition (TPD) results confirmed the presence of N_8^- on MWNTS. The N_8^- vibrational frequencies data from FTIR & Raman were consistent with DFT calculation results [74, 75]. ORR experiments with PN-MWNT catalyst suggested superior electro-catalytic activity compared to the commercial Pt/C catalyst (Figure 1.5d). In this PN catalyst, N-N sites were shown to be the active site and ORR activity was enhanced. In this study, N-N sites were synthesized on carbon nanotubes without forming C-N covalent bonds, and it was proved that lone pairs from synthesized N_8^- are very active and could play the role as electron donor which can serve as the active sites for ORR. It's also worth noting that N-N active sites here reported is completely different with aforementioned C-heteroatom-doped sites.

Since doping nitrogen into carbon lattice would decrease the material conductivity, the enhancement of ORR activity that can be achieved by increasing the amount of nitrogen doping is limited. By contrast, N_8^- can stabilize on MWNT without significantly changing MWNT bonding configurations. Thus, the good conductivity of carbon material can be maintained, and the encapsulation of more N_8^- may lead to better ORR activity.

The facile preparation and good performance for ORR made the N_8^- polynitrogen species supported on MWNT can be a potential candidate to replace Pt-based catalysts for fuel cells [75].

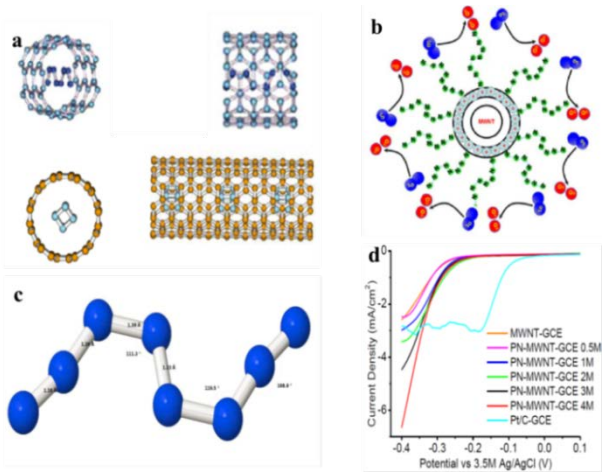

Figure 1.5 (a) The existence of N_8 encapsulation in CNT predicted by theoretical calculation [73]. (b) A novel cathode catalyst PN on carbon nanotube. (c) Calculations showing a N_8^- structure. (d) ORR results of PN-MWNT-GCE synthesized with different azide concentrations and commercial Pt/C catalyst.
Source: [75].

As mentioned above, the novel PN (N_8^-) materials only consist of inexpensive nonmetallic elements, exhibit high ORR activity and are environmental friendly. It is promising for replacing platinum-based catalysts. However, the relationship between ORR performance and PN structure, and the mechanism of the ORR over this catalyst are still not fully understood, which may hinder the optimization of the PN catalysts for ORR.

1.2 Objectives

The objectives of this dissertation were to investigate the catalytic properties of PN supported on different substrates for ORR and further identify its active sites and mechanisms.

The catalytic properties of PN for ORR was investigated in alkaline electrolytes and compared with that of commercial Pt/C catalyst. The substrates effects were discussed to promote PN catalysts synthesis.

The active sites and mechanisms of the ORR over PN catalysts were systematically investigated by combining kinetics study, NBO analysis and *in situ* Shell-Isolated Nanoparticle-Enhanced Raman Spectroscopy (SHINERS) characterization.

CHAPTER 2

N_8^- POLYNITROGEN SYNTHESIS WITH UV IRRADIATION AND ITS HIGH ACTIVITY FOR OXYGEN REDUCTION REACTION

2.1 Introduction

Polynitrogen N_8^- (PN) deposited on multiwalled carbon nanotubes (PN-MWNT) is a novel all nitrogen-based catalyst that can be used as the catalyst for ORR [75]. This material is metal free, low in cost, and can be prepared conveniently. We have reported electrochemical synthesis of N_8^- on MWNT under ambient conditions [75]. During synthesis, dissolved azide ions can be oxidized to form azide neutral radicals. N_8^- can be synthesized by further reaction of these radicals and stabilized on the positively charged MWNT. The reaction route can be denoted as:

$$N_3^- \rightarrow N_3\bullet \rightarrow N_8^-$$

Except for electrochemical oxidation, UV irradiation may also be used to produce azide radicals from azide anions, and the azide radicals possibly have the chance to be the precursors for the synthesis of N_8^-. Production of N_3 neutral radicals by photolysis of sodium azide solution was reported previously [76, 77]. Subsequently Hayon *et al.* discussed the possibility of forming unstable N_6 or N_4 radicals in solution by reaction of two N_3 neutral radicals produced by photolysis [78]. A more recent study suggested that various all-N materials might be obtained by photoexcitation of sodium azide under high pressure [79]. Except for sodium azide, photolysis of other nitrogen precursors, such as HN_3 [80], ClN_3 [81] and solid N_2 [82] had also been reported and linear N_3, cyclic N_3, N and N_4 radicals were detected. These results prompted us to combine the electrochemical synthesis method with UV irradiation to synthesize N_8^-.

To choose the suitable UV wavelength for the investigation, time dependent density functional theory (TDDFT) was carried out to construct the UV-Vis absorption spectrum of azide anion in the gas phase. The spectrum showed the lowest energy optical peak at 288 nm corresponding to the transition from the ground state to the first excited state. The highest intensity peak in the 233 nm region was in total agreement with other experimental reports [83-85]. The highest energy peak at 147 nm can be found in the work of McDonald *et al*. [85] in which internal azide transitions are reported at about 145-150 nm.

In this study, a 254nm mercury lamp (UVP R-52g, power: 100W) was used for investigation of the UV effect, as 254nm lies in the absorption band with the highest intensity in the 233 nm region [86]. As a comparison, a 365nm mercury lamp (UVP B-100AR, power: 100W) was also used, and the light emitted should not be absorbed by azide solution. Although UV absorption at higher energy (145-150nm) might produce more active azide radicals, UV light with the wavelength below 200 nm can be strongly absorbed by oxygen in the air [87] or water [88] in the solution, the wavelength was not investigated in this study.

2.2 Experimental

In this section, Polynitrogen N_8^- (PN) deposited on multiwalled carbon nanotubes (PN-MWNT) were synthesized by cyclic voltammetry (CV) method with UV irradiation. All the materials and chemicals were commercially available and were used without further purification.

2.2.1 Preparation of MWNT Electrodes

Here, two methods were used to prepare MWNT electrodes. One method for preparing MWNT electrodes was to deposit MWNT ink on glassy carbon electrodes (MWNT-GCE, the diameter of GCE is 3 mm, purchased from CH Instruments). Before preparation, the GCE was polished on polishing pads with different grades of alumina paste (1, 0.3, 0.05μm, respectively, CH Instruments) to obtain a mirror finish and then thoroughly washed with distilled water. After that, 10mg of MWNT powder (-COOH functionalized multi-walled carbon nanotubes, purchased from Nanolab) and 5mL ethanol containing a Nafion solution (0.5 wt%, DuPont) were mixed and sonicated for 30 minutes using an ultrasonic processor (Cole-Parmer, 130 watts) to obtain a MWNT ink suspension. 5μL of the ink suspension was deposited onto the surface of a pre-polished GCE denoted as MWNT-GCE and dried overnight in air. For comparison, Pt/C-GCE was prepared by deposition of 10 mg commercial Pt/C fuel cell catalyst (10% Pt on Vulcan XC-72, Sigma-Aldrich) on GCE with the same procedures as for MWNT-GCE.

Another method for preparing MWNT electrodes was to use MWNT sheets as electrodes directly. 50 mg of MWNT powder, 250 mg of surfactant sodium dodecyl sulfate (SDS, from Aldrich) and 50 ml distilled water were mixed and under sonication for 30 minutes. Then the mixture was vacuum-filtered using the PTFE membranes (10μm pore size, purchased from Millipore) and thoroughly washed with distilled water and methanol to remove residual SDS. After drying in air, round-shaped MWNT sheets were obtained by peeling off from the PTFE membrane.

2.2.2 Preparation of PN-MWNT

PN deposited on MWNT was synthesized by CV under ambient conditions which was reported in our group's previous paper [75]. CV technique was performed with a three-electrode setup using an electrochemistry analyzer CHI 832c to measure the current by scanning the potential cyclically with a constant rate within a certain range.

MWNT-GCE or MWNT sheet was dipped into 40mL 2M NaN_3 (Aldrich)-buffer solution (PH=4.0), which was used as the working electrode. Pt and Ag/AgCl were used as the counter electrode and reference electrode, respectively. The CV scan rate was set to be 1 mV/s and the potential range was set to be between +0.8V and -0.8V. The sample was scanned for 12 CV cycles, and then was dried overnight in the air. PN deposited on MWNT-GCE or MWNT sheets were synthesized under UV irradiation on top of the electrolyte during CV scanning, and the samples were denoted as PN-MWNT-GCE 254nm, PN-MWNT sheet 254nm, PN-MWNT-GCE 365nm, and PN-MWNT sheet 365nm, respectively, which corresponded to the wavelength of the UV light. MWNT sheets were used to synthesize PN-MWNT sheet with or without UV to produce large amount of PN-MWNT sheet samples for following characterization (i.e., Raman, FTIR and TPD).

2.2.3 Characterization of PN-MWNT

Raman spectroscopy was performed with a Thermo Scientific DXR Raman microscope. FTIR was carried out using a Nicolet ThermoElectron FTIR spectrometer combined with a MIRacle ATR platform assembly and a ZnSe plate, and denoted as ATR-FTIR. Temperature programmed decomposition (TPD) was carried out using the AutoChem II 2920 (Micromeritics) system. Samples were heated in flowing helium from room

temperature to 850 °C at a heating rate of 10 °C /min. The released species were monitored with an on-line mass spectrometer (QMS 200, Stanford Research Systems). Shell-Isolated Nanoparticle-Enhanced Raman Spectroscopy (SHINERS) spectra were recorded with a HR-800 (HORIBA Jobin Yvon) spectrometer integrated with a confocal microscope. The excitation wavelength was 638 nm from a He-Ne laser. A custom-made spectroelectrochemical cell with a Pt wire counter electrode and an SCE reference electrode was used for the SHINERS measurements of ORR. 0.01M KOH solution was used as the electrolyte, which was deaerated with argon gas before injected into the spectroelectrochemical cell.

2.2.4 Electrochemical measurements

The electrocatalytic activity toward the ORR was evaluated by a rotating disk electrode (RDE) setup (ALS Co., Ltd) using linear sweep voltammetry (LSV) measurements. For LSV measurements, the scanning rate was 5mV/s with various rotating speeds. The PN-MWNT-GCE electrode synthesized with and without UV irradiation were dried in air and used as the working electrode directly. Pt and Ag/AgCl were used as the counter electrode and reference electrode, respectively. 0.1M KOH solution was used as the electrolyte. Prior to the experiments, oxygen or nitrogen was bubbled into the electrolyte for at least 30 minutes until saturated; during the experiments, oxygen or nitrogen was flowed over the electrolyte to maintain saturation.

2.3 Results and Discussion

Raman spectroscopy was carried out to confirm the formation of PN deposited on MWNT with UV irradiation after 12 CV cycles and the results are shown in Figure 2.1. The

vibrational mode at 1080 cm^{-1} was detected from PN-MWNT and PN-MWNT 254nm, which can be assigned to N_8^- [75]. However, the line was much less obvious from PN-MWNT 365nm, which suggested that less N_8^- was synthesized. ATR-FTIR spectra in Figure 2.2 showed a clear line at about 2050 cm^{-1}, which can be assigned to N_8^- [75], and the peak intensity followed the order of PN-MWNT sheet 254nm > PN-MWNT sheet > PN-MWNT sheet 365nm. The peak near 2100 cm^{-1} can be assigned to the azide ion asymmetric stretching mode from unreacted sodium azide [75], and the peak intensity corresponding to the residual N_3^- amount followed the trend PN-MWNT 365nm > PN-MWNT > PN-MWNT 254nm. The lines around 1500 cm^{-1}, 1640 cm^{-1} and 3300 cm^{-1} can be assigned to the residual water trapped in the MWNT sheet. To investigate the thermal stability of the PN samples, TPD was carried out over different samples and the results are shown in Figure 2.3 and Table 2.1. Nitrogen desorption from the decomposition of N_8^- was detected between 400 ^oC and 450 ^oC. The desorption amount suggested that the synthesis of N_8^- was significantly improved with UV 254nm irradiation, while less N_8^- was synthesized with UV 365nm irradiation, compared to the sample without UV. The desorption peak from PN-MWNT 254nm was much narrower than that from PN-MWNT, suggested that synthesized N_8^- was more uniformly deposited on MWNT with UV irradiation. The Raman, FTIR and TPD results are consistent and confirm that the synthesis amount of N_8^- can be enhanced with 254nm UV irradiation because absorption of the 254nm UV light facilitates electrochemical oxidation of azide ions to azide neutral radicals. 365nm UV light could not be absorbed by azide ions, and heating by the UV lamp may inhibit adsorption of azide species and increase the desorption of final product, thus leading to a less amount of N_8^- synthesized on the substrate.

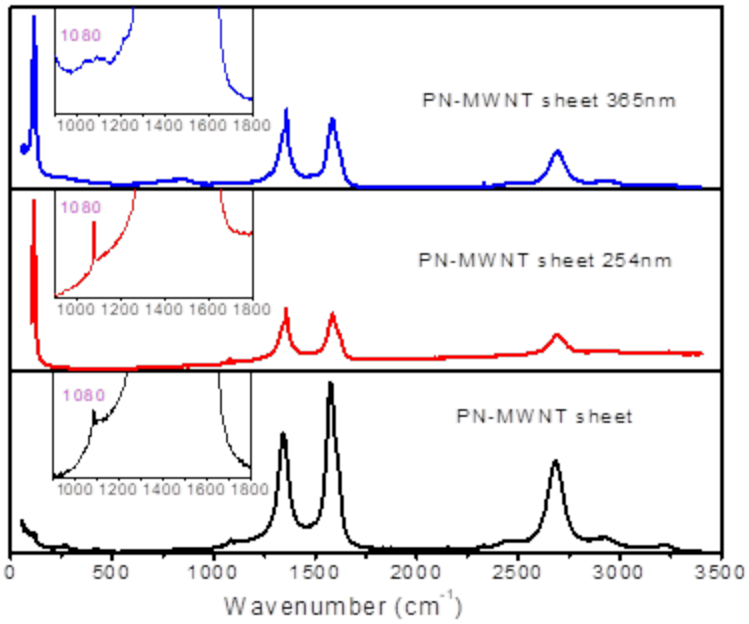

Figure 2.1 Raman spectra of PN-MWNT samples.

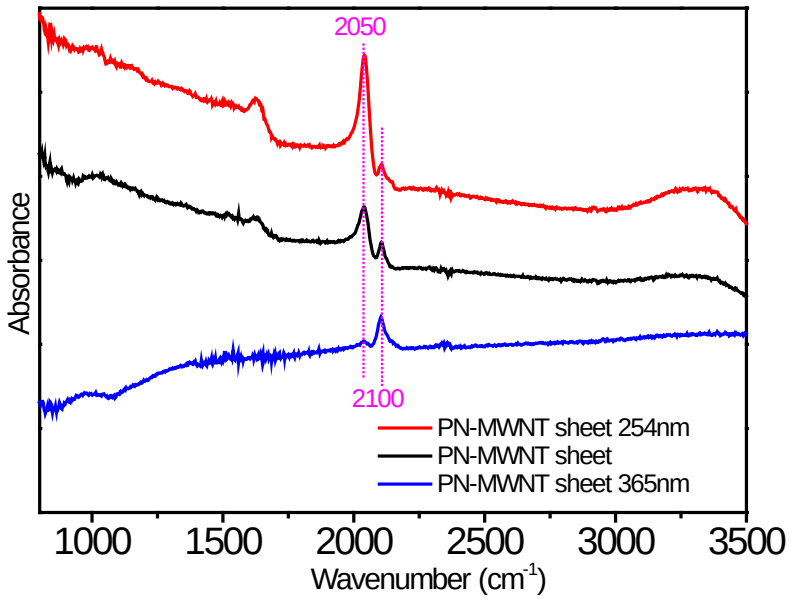

Figure 2.2 ATR-FTIR spectra of PN-MWNT samples.

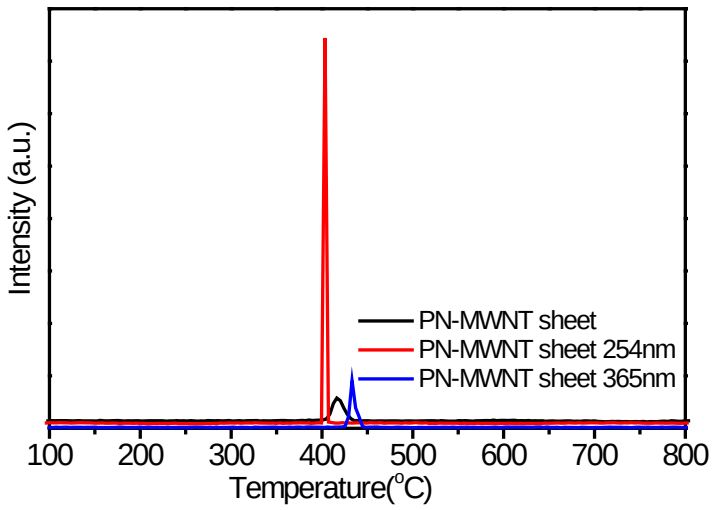

Figure 2.3 N^{14} signal normalized by sample weight from TPD scans for PN-MWNT samples.

Table 2.1 Nitrogen Desorption Amount (mmol/grams of sample)

Entry	Sample	Nitrogen desorption amount
1	PN-MWNT sheet	1.0
2	PN-MWNT sheet 254nm	3.9
3	PN-MWNT sheet 365nm	0.9

[a] calculated by integration of the TPD results and comparing the peak areas with those from injection of pure nitrogen under the same experiment conditions.

The electrocatalytic activities of the as-prepared PN-MWNT-GCE electrodes toward ORR were evaluated by LSV measurement using RDE setup at different rotating rates in O_2-saturated 0.1 M KOH electrolyte at a scan rate of 5 mVs^{-1}. As can be seen in Figure 2.4a~d, the catalytic current density of all three samples increased with increasing rotating rate due to the enhanced diffusion of electrolytes [89]. In addition, the current density followed the trend PN-MWNT-GCE 254nm > PN-MWNT-GCE > PN-MWNT-GCE 365nm in the potential range of -0.6V~-0.8V. This current density

sequence is consistent with the amount of synthesized N_8^- achieved from Raman, FTIR and TPD results, suggesting the larger N_8^- formed on MWNT led to higher reduction current density. Actually, our previous study had proved that the larger amount of N_8^- deposited uniformly on MWNT the more accessible active sites on the PN-MWNT electrode can provide for the dissolved oxygen to be reduced on the surface and lead to the improved electrocatalytic activity [75]. Comparison of LSV curves obtained at different electrodes with a rotating rate of 1500 rpm is presented in Figure 2.5. Although the onset potential of PN-MWNT-GCE 254nm is still lower than that of the commercial Pt/C catalyst (10% platinum on Vulcan XC-72 (E-Tek)), the current density of PN-MWNT-GCE 254nm is even higher than that of Pt/C catalyst at the potential of -0.8V. Moreover, it's worth noting that nitrogen loading percentage in PN-MWNT-GCE 254nm (5.46 wt.%. calculated based on Entry 2 of Table 5) is much lower than that of platinum (10 wt.%) in commercial Pt/C catalyst, which indicated the potential replacement of Pt electrode by metal free PN-MWNT catalysts.

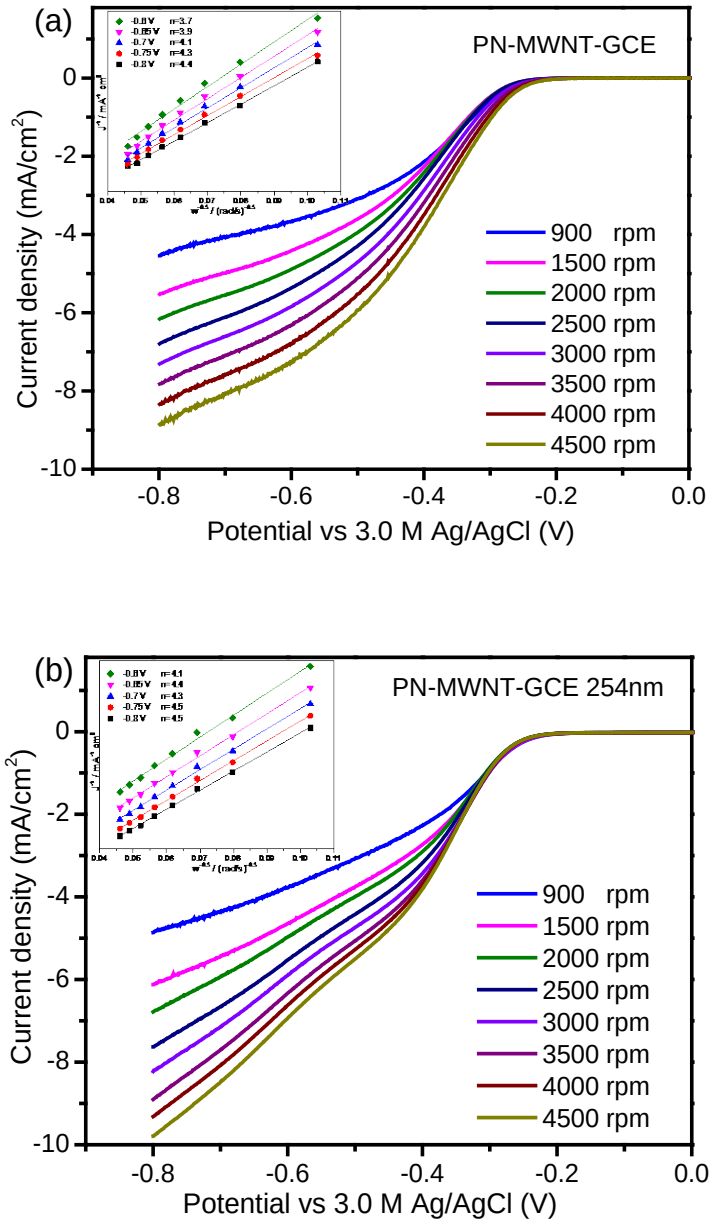

Figure 2.4 LSV curves of ORR on GCE at different rotation rates in oxygen-saturated 0.1 M KOH solution (scan rate: 5 mV/s). (a) PN-MWNT-GCE, (b) PN-MWNT-GCE 254nm, (c) PN-MWNT-GCE 365nm, (d) N_3^-- MWNT-GCE. The insets in a, b, c and d show corresponding Koutecky-Levich plots (1/J vs. $1/\omega^{0.5}$). (Continued)

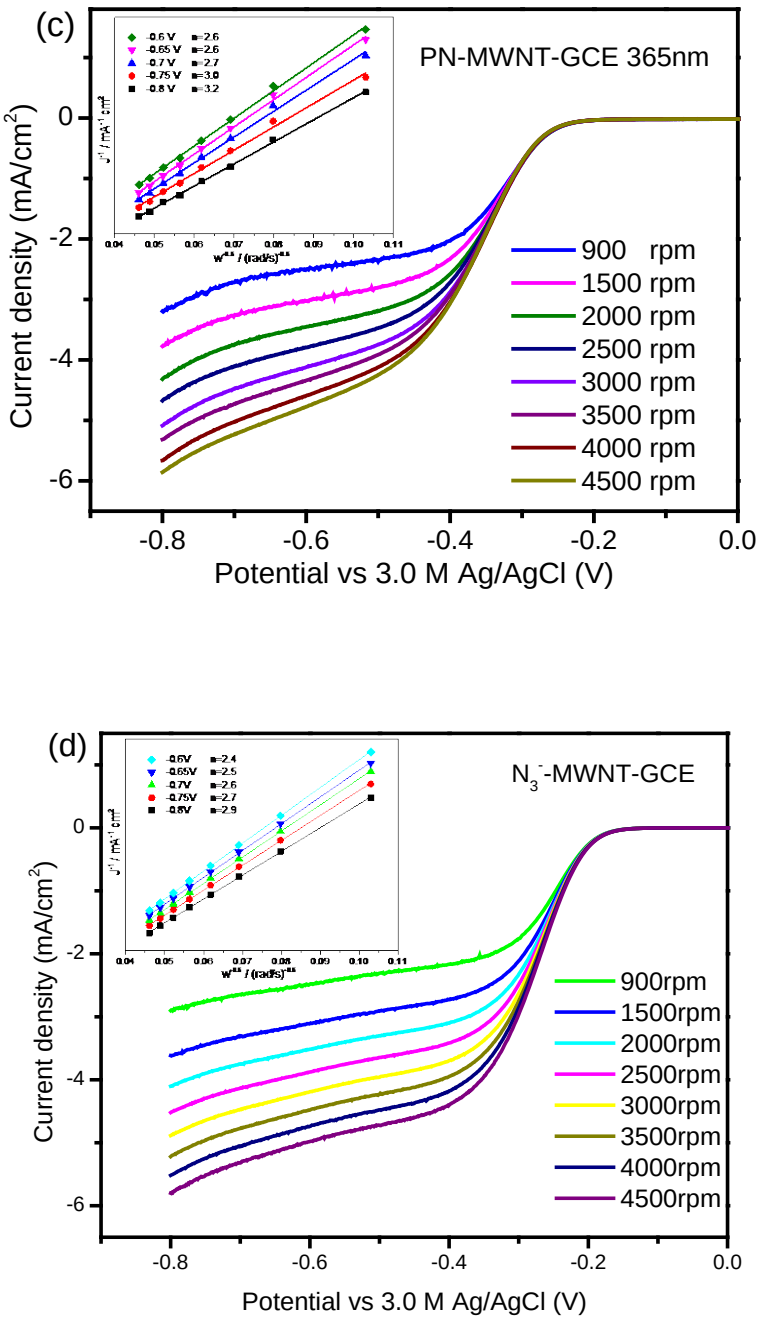

Figure 2.4 (Continued) LSV curves of ORR on GCE at different rotation rates in oxygen-saturated 0.1 M KOH solution (scan rate: 5 mV/s). (a) PN-MWNT-GCE, (b) PN-MWNT-GCE 254nm, (c) PN-MWNT-GCE 365nm, (d) N_3^-- MWNT-GCE. The insets in a, b, c and d show corresponding Koutecky-Levich plots (1/J vs. $1/\omega^{0.5}$).

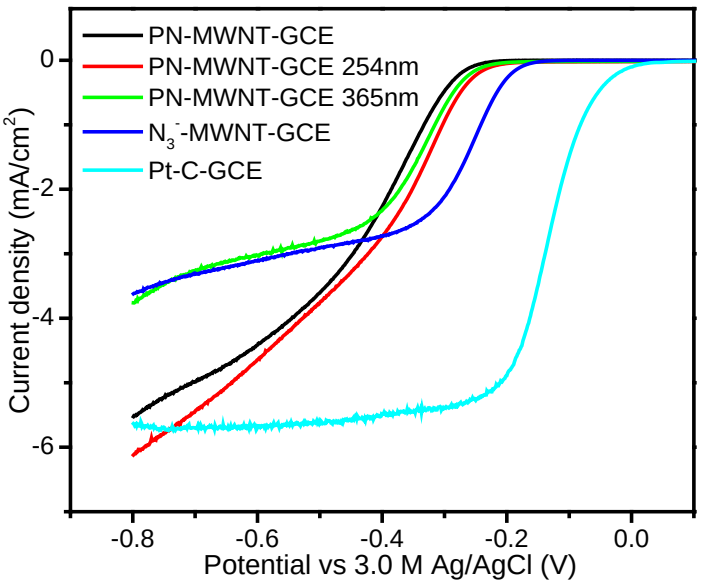

Figure 2.5 LSV curves of ORR on PN-MWNT-GCE, PN-MWNT-GCE 254nm, PN-MWNT-GCE 365nm, N_3^--MWNT-GCE and Pt-C-GCE electrode in oxygen-saturated 0.1 M KOH solution with a rotation speed of 1500 rpm (scan rate: 5 mV/s).

It is widely accepted that the ORR has two reduction pathways based on the different electron transfer number (n): (i) four-electron ($4e^-$) pathway to produce water, and (ii) two-electron ($2e^-$) pathway with the formation of peroxide as intermediate compounds. Obviously, the four-electron ($4e^-$) process is highly preferred and indicates better electrocatalytic ORR performance of a given catalyst. Kinetic study can determine the electron transfer number (n) by Koutecky-Levich (K-L) equation as following, which can be used to identify the possible ORR pathway [23, 90].

$$\frac{1}{J} = \frac{1}{J_L} + \frac{1}{J_k} = \frac{1}{B\omega^{0.5}} + \frac{1}{J_k} \qquad (2.1)$$

$$B = 0.62nFC_o(D_o)^{2/3}\nu^{-1/6} \qquad (2.2)$$

Where J is the measured current density, J_K and J_L are the kinetic and diffusion limiting current density, respectively. B is the Levich constant, n is the number of electrons transferred per oxygen molecule in the reaction, F is the Faraday constant (F=96485C

cm^{-1}), C_o is the bulk concentration of O_2 (C_o=1.2×10^{-3}mol L^{-1}), D_o is the diffusion coefficient of O_2 (D_o=1.9×10^{-5} cm s^{-1}), ν is the kinematic viscosity of the electrolyte (ν =0.01cm^2 s^{-1}), ω is the angular velocity (rad s^{-1}). According to K-L equation, the n of different catalysts can be derived from the slope of 1/J vs. $1/\omega^{0.5}$ plots (inset of Figure 2.4a~c). Before conducting fitting analysis for the PN samples, the n of commercial Pt/carbon catalyst was obtained via the K−L equation to be 4.4-4.5 which suggested a four-electron process on the Pt/C electrode. The experiment confirmed the reliability of the data collected and validity of the fitting method [91, 92]. From the fitting lines shown in Figure 2.4a~c inset, all plots give good linearity and parallelism, indicating a first-order reaction for ORR toward dissolved oxygen [93]. Moreover, the n value at the PN-MWNT-GCE electrode was derived to be 3.7-4.4, which indicated that it was through a four-electron process on the N_8^- [89, 93]. The similar n value (4.1-4.5) was achieved on sample PN-MWNT-GCE 254 nm, which suggested that the pathway of this sample was also through a dominant four-electron process. However, the n value for PN-MWNT-GCE 365 nm was 2.6-3.2 lying between the two-electron and four-electron reduction processes, which suggests that the ORR may proceed by a coexisting pathway involving both the two-electron and four-electron transfers [90]. ORR on N_3^- is a two-electron pathway while ORR on N_8^- is through a four-electron pathway (proved by PN-MWNT-GCE results) in consideration of coexisting of a large amount of residual N_3^- and a small amount of produced N_8^- on PN-MWNT-GCE 365 nm from the FTIR and Raman results. To confirm this assumption, the LSV measurement was also performed on N_3^--MWNT-GCE electrode. The N_3^--MWNT-GCE electrode was prepared by dipping the MWNT-GCE electrode in the 2M NaN_3 electrolyte for 11 hours and then dried in atmosphere overnight.

The ORR polarization curves and fitting results are shown in Figure 2.4d. The derived n value for N_3^--MWNT-GCE electrode was 2.4-2.9, which led to a characteristic two-electron process and further confirmed the aforementioned hypothesis.

The different transferred electrons number n derived in the above kinetic study indicated that the mechanisms behind are different. One of the widely adopted approaches to explore the mechanism of ORR is to probe the O_2 chemisorption mode on the catalyst which was originally proposed by Gong *et al.* through combining experiment and DFT calculation. The work concluded that the side-on adsorption (Yeager model) favored four-electron pathway while the end-on adsorption (Pauling model) led to a two-electron process [12]. In this study, the O_2 chemisorption mode was determined by *in situ* Shell-Isolated Nanoparticle-Enhanced Raman spectroscopy (SHINERS) [21, 94-96] through monitoring the surface reaction process. In the most recent work, Galloway *et al.* [95] utilized SHINERS for the same reaction on Pt electrode and they assigned the peaks centered at 456 and 490 cm^{-1} to the O_2 flat (i.e. side-on) and end-on adsorption, respectively. Figure 2.6a~b presents the *in situ* SHINERS spectra of ORR on PN-MWNT-GCE and N_3^--MWNT-GCE. On the PN-MWNT-GCE surface, two peaks were observed at 377 and 683 cm^{-1}. The former one can be ascribed to the side-on adsorption of O_2, which is close to the reported wavenumber of the side-on peak (the slight difference may due to the different catalysts used in two studies, i.e. PN vs Pt), which suggested a four-electron pathway involved. The latter peak can be attributed to peroxide species [97]. Furthermore, it's found that this peak was very weak indicating that the generated peroxide species can be negligible. Therefore, it can be concluded that the dominant pathway on PN-MWNT-GCE was through four-electron process, which is

consistent with observed n-value of ~4 in the above kinetic study. The SHINERS spectra of N_3^--MWNT-GCE also have two peaks. The lower wavenumber peak shifts to 486 cm^{-1} while the higher wavenumber peak is almost the same (677 cm^{-1}) comparing with that of PN. The 486 cm^{-1} is close to the reported wavenumber of the end-on peak (490 cm^{-1}) suggested the reaction is through two-electron process. The 677 cm^{-1} is also assigned to peroxide species [97] and is significantly stronger compared to that on PN sample, indicating that the generated peroxide species was abundant. Accordingly, the ORR mechanism is via a two-electron process, which further confirms the above kinetic study.

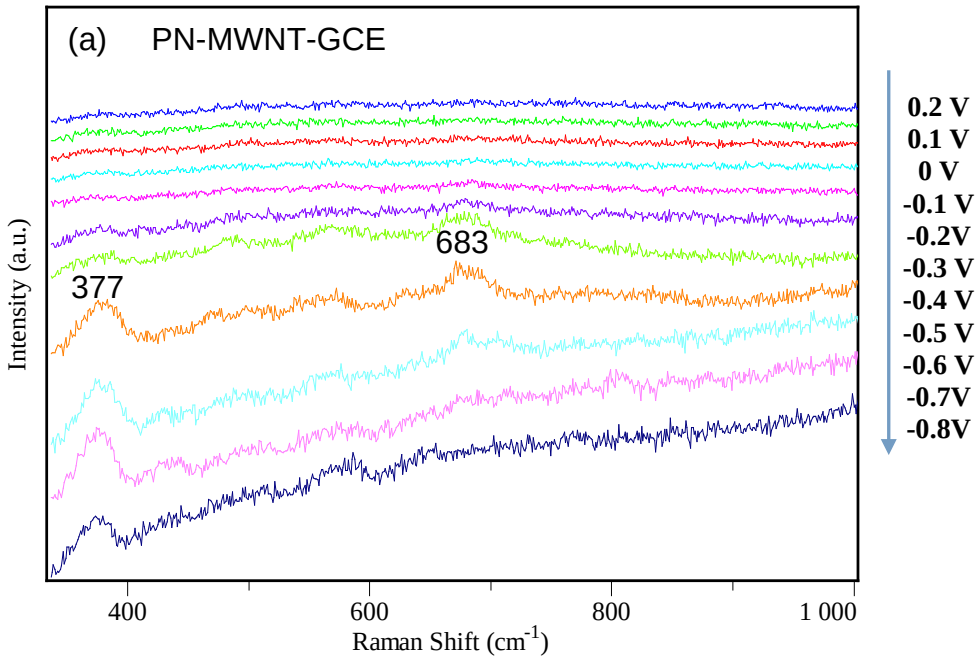

Figure 2.6 *In situ* SHINERS spectra of ORR on (a) PN-MWNT-GCE and (b) N_3^--MWNT-GCE. (Continued)

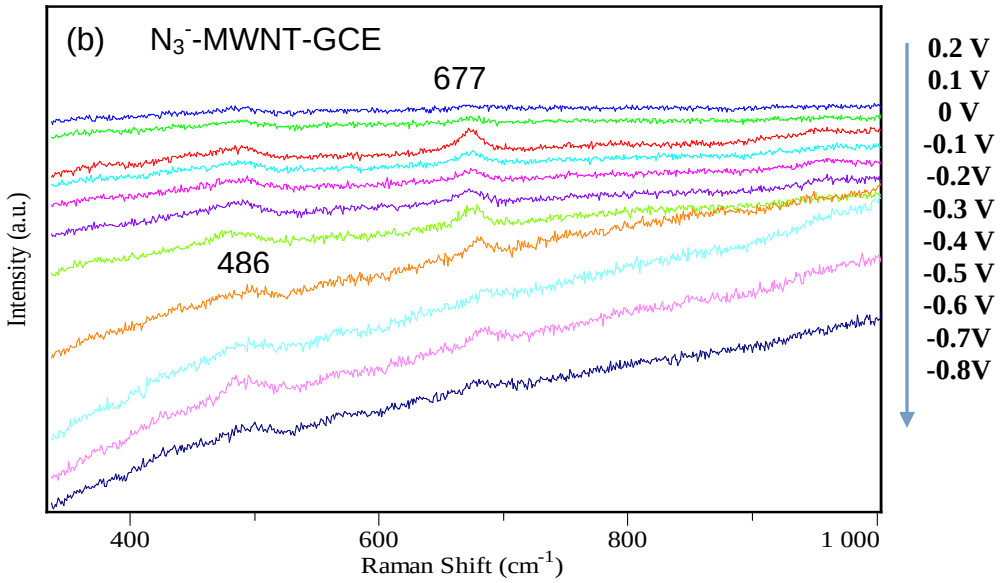

Figure 2.6 (Continued) *In situ* SHINERS spectra of ORR on (a) PN-MWNT-GCE and (b) N_3^--MWNT-GCE.

To further clarify the mechanism of oxygen reduction on the PN samples, natural bonding orbital (NBO) analysis [75] combining with the above kinetic and SHINERS results were employed to investigate the possible O_2 adsorption sites. Based on the calculation results by our previous study, the partial charge distribution on N_8^- is presented in Figure 2.7 [75]. It's believed that the most active sites are N1 and N2 located in the center of the chain with adjacent position that have more negative charges than other nitrogen atoms, where oxygen would be activated via direct bonding with the electrons of the N1 and N2 [47]. Moreover, SHINERS analysis suggested that oxygen adsorbed on N_8^- was by the side-on model, thus it's reasonable to propose that the adsorption of O_2 occurred on the N1 and N2 nitrogen atoms. The O-O bonding would be effectively weakened and easily broken by this side-on adsorption [12], which represents an efficient four-electron transfer pathway in ORR [47, 98]. Therefore, the ORR mechanism would be through four-electron transfer pathway on the N_8^-. N_3^- is a linear centrosymmetric anion

with more negative charges on the two end nitrogen atoms that are more active for oxygen adsorption [99, 100]. SHINERS analysis demonstrated that oxygen was adsorbed on N_3^- by the end-on model, it's rational to conclude that this adsorption occurred on the end nitrogen atom. As a result, the end-on chemisorption mode of O_2 led to a dominant two-electron transfer pathway in ORR [47, 98]. The mechanism of oxygen reduction on N_3^- and N_8^- based on different O_2 chemisorption mode are illustrated in Figure 2.8.

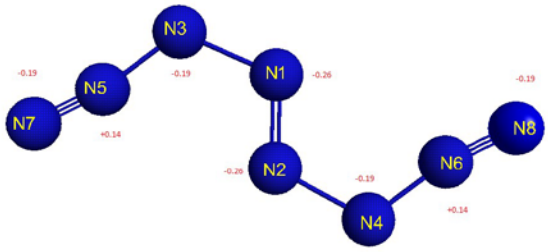

N atom	N1	N2	N3	N4	N5	N6	N7	N8
Charge distribution	-0.26	-0.26	-0.19	-0.19	0.14	0.14	-0.19	-0.19

Figure 2.7 NBO partial charge distribution on an N_8^- anion [75].

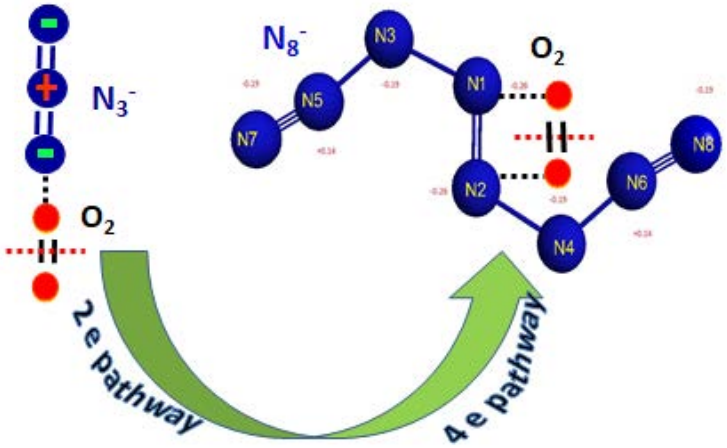

Figure 2.8 Mechanism for oxygen reduction on N_3^- and N_8^- based on different O2 chemisorption mode.

2.4 Summary

In this section, electrochemical synthesis of N_8^- on MWNT with UV irradiation and its application in ORR were investigated. Compared to the synthesis without UV, a larger amount of N_8^- was prepared with the irradiation of 254nm UV light, possibly because photoexcitation assisted the generation of azide radicals as the precursors for the synthesis of N_8^-. Moreover, the synthesized N_8^- with 254nm UV irradiation distributed more uniformly on MWNT. The larger amount of N_8^- on MNWT provided more active sites for ORR in 0.1M KOH, which enhanced the ORR current density. The results indicated that UV irradiation can be a facile strategy to improve the synthesis of N_8^- on MWNT. Optimization of the UV energy and the power of the UV lamp for the synthesis may lead to even a higher amount of N_8^- synthesized and ORR performance. Kinetic study revealed that it was through a four-electron process at the N_8^- while the O_2 reduction catalyzed at the N_3^- is a two-electron reduction process. The oxygen chemisorption model gained by SHINERS analysis suggested that the side-on and end-on adsorption occurred at N_8^- and N_3^- , respectively indicating the consistent electron transfer process with kinetic study. Finally, the ORR mechanism was further clarified by introducing NBO analysis to assign the possible active sites. The two atoms of the N_8^- (N1 and N2) calculated by NBO analysis were considered as the active sites for ORR, which facilitated the four-electron pathway by weakening the O-O bonding with side-on adsorption. In contrast, the end nitrogen atom of N_3^- was regarded as the active site, which favored the two-electron reduction at the N_3^- by end-on adsorption. This work provides a novel route for PN synthesis with high efficiency under ambient condition and understanding of its intrinsic oxygen reduction activity.

CHAPTER 3

N_8^- POLYNITROGEN STABILIZED ON NITROGEN DOPED GRAPHENE AS METAL-FREE ELECTROCATALYST FOR OXYGEN REDUCTION REACTION

3.1 Introduction

As discussed in the previous chapter, PN-MWNT catalyst had superior electro-catalytic activity compared to the commercial Pt/C catalyst. The facile preparation and good performance for ORR made the PN catalyst can be a potential candidate to replace Pt-based catalysts for ORR. The previous results showed that PN amount determined the current density of ORR. Therefore, it is important to increase the amount of N_8^-.

A theoretical study showed that a charge transfer mechanism can stabilize polymeric nitrogen chain N_8 inside carbon nanotubes. The charge transfer between carbon nanotube and nitrogen chain N_8 leads to a net positive charge on the inner wall of the nanotube and a net negative charge on the N_8 chain, therefore it can create an effective electric field inside the nanotube, which, in turn, stabilizes the N_8 chain [73]. Therefore, the substrate plays a crucial role for stabilizing PN [73, 75]. Recently Abou-Rachid and Liu's groups demonstrated that a polymeric nitrogen chain could be stabilized between multiple graphene layers [101] and multilayer BN matrix [102-104] under ambient conditions owing to the charge transfer from hosting materials to polymeric nitrogen by theoretical calculations [103]. Since graphite structure does not involve geometric parameters, such as radius and chirality in carbon nanotubes, graphene based matrix may be a promising support to stabilize the polynitrogen by charge transfer interaction between graphene matrix and nitrogen chain [101], which sparks us to synthesize polynitrogen N_8^- (PN) on graphene based matrix at ambient conditions.

Graphene, as a two dimensional graphitic material, is a one atomic-thick atom sheets with a 2D planar geometry which will further facilitate electron transport, and make it an attractive support for electrochemical applications [42, 105-108]. However, pure graphene is difficult to uniformly anchor catalyst nanoparticles due to its high graphitization, low structural defects and smooth surface. More importantly, the interaction between catalyst particles and graphene is not strong, which will lead to limited catalytic properties of nanoparticle catalysts [109, 110]. One solution to the problem is to introduce the heteroatom dopants such as nitrogen (N), boron (B), phosphorus (P), sulfur (S) and others into graphene matrix. Since heteroatom doping can produce much more defect sites in the basal planes and edges of graphene sheets, modify the density of electronic states of graphene and adjust the mechanical properties, which will directly enhance its electrocatalytic activity and stability of catalyst nanoparticles [110-115]. Among numerous dopants, nitrogen atom with a similar atomic radius (0.70 Å) as carbon (0.77 Å) and a more negative electronegativity ($\chi_N = 3.04$) than C ($\chi_C = 2.55$), which makes it easily incorporate into the graphene matrix via substitutional doping without destroying the planar structure of graphene [110, 116]. On the other hand, our previous results have indicated that positively charged sites of catalyst support are favored for stabilization of negative N_8^- (PN) [75] . In nitrogen doped graphene, electron transfer happens from C to N atom due to the higher electronegativity of N than C and creates partial positive charge on adjacent C atom [117], which can become the active centers for the synthesis of PN. Based on these qualities, it is of significant interest for us to synthesize PN supported on nitrogen doped graphene and investigate its electrochemical performance, a subject that has not been studied yet.

In this section, PN deposited on nitrogen-doped graphene (PN-NG) were synthesized using cyclic voltammetry (CV) method [75] at ambient conditions for the first time, NG with different nitrogen contents were prepared via a one-step facile hydrothermal method. Systematic characterizations on morphology and microstructures were conducted. Moreover, the catalytic activities of series PN-NG samples were evaluated as cathode catalysts for ORR in alkaline solution. The optimum PN-NG catalyst exhibited excellent catalytic activity, due to the incorporation of nitrogen atoms into the graphene matrix.

3.2 Experimental

3.2.1 Synthesis of graphene and nitrogen-doped graphene

Unless otherwise stated, all the materials and chemicals were commercially available and were used as received without further purification. Graphite oxide (GO) was synthesized from graphite powder by a modified Hummers method according to previously reported work [118]. Then it was dispersed into deionized water and sonicated for 30 mins to exfoliate oxidized graphite particles to GO colloid solution.

Nitrogen-doped graphene (NG) was synthesized by a facile hydrothermal method with GO as raw material and urea as chemical dopant [117, 119]. Typically, a given amount of urea was gradually added into the 120 mL of prepared GO colloid solution (2 mg/mL) then the mixture solution was vigorously stirred for 30 min at room temperature. After that, the solution was transferred into a 200 mL Teflon-lined stainless steel autoclave and hydrothermally heated at 180 °C for 12 h and then naturally cooled down to room temperature. Finally, the resulting NG hydrogel was fully washed with deionized water to

remove unreacted urea and freeze-dried for 72 hr. Here, the nitrogen content could be adjusted by controlling the mass ratio of GO/urea as 1/30, 1/50, 1/100, and 1/150, and corresponding samples obtained were denoted as N_1G, N_2G, N_3G, and N_4G respectively. The control sample was prepared under the same experimental condition using only GO without urea and was denoted as G. Round-shaped NG (or graphene) sheets were fabricated by vacuum filtration of the NG (or graphene) colloid dispersion with DMF solvent and further used to synthesize PN-NG (or PN-G) sheet.

3.2.2 Preparation of PN electrode

Polynitrogen N_8^- electrode synthesis was carried out by CV treatment with a three-electrode system followed our previous work [75] except using NG (or G) as substrates. NG (or G) ink was prepared by 10mg of the NG (or G) powder ultrasonically dispersed into 5mL DMF containing a Nafion solution (0.5 wt%, DuPont). 5μL of the ink was coated onto the surface of a pre-polished glassy carbon electrode (GCE, 3.0 mm) denoted as NG-GCE (or G-GCE) and dried in air. Then the GCE was dipped into 40mL 2M NaN_3 (Aldrich)-buffer solution (PH=4.0), which was used as the working electrode. Pt and Ag/AgCl were used as the counter electrode and reference electrode, respectively. CV [75] was performed using a CHI 832c electrochemistry analyzer with the three-electrode system to synthesize polynitrogen N_8^- on NG (or G) substrate. The resulting PN-NG-GCE and PN-G-GCE electrodes were dried in air and used as the working electrodes for ORR test. Herein, PN with different nitrogen doping content graphene samples were denoted as PN-N_1G, PN- N_2G, PN-N_3G, and PN-N_4G respectively.

PN-NG (or PN-G) sheet were prepared under the same electrochemical conditions using round-shaped NG (or graphene) sheets as working electrodes to produce a large amount of PN sheet samples for following characterization (i.e., FTIR and TPD).

3.2.3 Characterization of PN-NG

X-ray photoelectron spectroscopy (XPS) measurements were performed on Thermo K-Alpha X-ray photoelectron spectroscopy system. Raman spectroscopy was performed with a Thermo Scientific DXR Raman microscope. SEM was performed on a Hitachi S-3400N scanning electron microscope and TEM was performed on a Hitachi H7500 transmission electron microscope. FTIR spectras were collected using a Nicolet IS-10 (Thermo Fisher Scientific). The Brunauer-Emmett-Teller (BET) specific surface areas of NG and G were determined by N_2 adsorption/desorption at liquid nitrogen temperature using an AutoChem 2920 II (Micromeritics). Temperature programmed decomposition (TPD) was carried out using the AutoChem II 2920 system. Samples were heated in flowing helium from room temperature to 850 °C at a heating rate of 10 °C /min. The released species were monitored with an on-line mass spectrometer (QMS 200, Stanford Research Systems).

3.2.4 Electrochemical measurements

The electrochemical tests were carried out in a rotating disk electrode (RDE) setup (ALS Co., Ltd) using linear sweep voltammetry (LSV) measurements. For LSV measurements, the scanning rate was 5mV/s with various rotating speeds. The PN-G-GCE and PN-NG-GCE electrodes were dried in air and used as the working electrode directly. Pt wire and Ag/AgCl (KCl, 3 M) were used as the counter electrode and reference electrode, respectively. 0.1M KOH solution was used as the electrolyte. Prior to the experiments,

oxygen or nitrogen was bubbled into the electrolyte for at least 30 minutes until saturated; during the experiments, oxygen or nitrogen was flowed over the electrolyte to maintain saturation.

3.3 Results and Discussion

3.3.1 Characterization of NG

The XPS characterization was used to analyze the elemental composition and nitrogen bonding configurations of NGs. Figure 3.1a shows the XPS spectra of the NG samples in comparison to graphene. The peaks at ~284.5, 399.3 and 531.9 eV can be assigned to the binding energies of C1s, N1s, and O1s, respectively. The O1s and C1s peaks of NG samples became weaker and the N1s peak became much stronger as compared with that of G, which indicated that N had been successfully introduced into graphene matrix after hydrothermal process of the GO and urea mixture. The nitrogen amount (atomic percentages) on four nitrogen-doped graphene samples surface (N_1G, N_2G, N_3G, and N_4G) were 6.5%, 7.8%, 8.8%, and 8.5% as listed in Table 3.1. It is obvious that more nitrogen atoms could be doped into the graphene matrix along with the increase of urea dose. However, the nitrogen content in NG samples no longer increased when the mass ration of urea/GO increased up to 150:1, indicating the NG with the highest nitrogen content could be obtained under a proper mass ratio of GO/urea.

Table 3.1 Parameters Derived from XPS, BET, and Raman Spectra Measurements

Samples	Mass ratio of the urea and GO	Composition measured by XPS (atom %)							BET	Raman
		C	O	N	Pyridinic N	Pyrrolic N	Graphitic N	Oxidized N	(m^2/g)	I_D/I_G
G	0:1	87.3	12.7	--	--	--	--	--	150.6	1.05
N_1G	30:1	83.9	7.9	6.5	2.52	2.91	0.75	0.32	154.8	1.06
N_2G	50:1	83.2	7.4	7.8	2.82	3.45	1.03	0.50	161.1	1.08
N_3G	100:1	82.5	6.7	8.8	2.93	4.48	0.95	0.44	135.7	1.10
N_4G	150:1	82.1	7.4	8.5	3.26	3.92	0.76	0.56	102.5	1.12

The deconvoluted high-resolution N1s spectra of nitrogen-doped graphene (NG) sample was performed and displayed in Figure 3.1b. (The sample N_2G was taken as an example.). As can be seen, N1s peak can be divided into four types of nitrogen components which can be identified by the bonding state of the nitrogen atom, namely, pyridinic N (~398.3 eV), pyrrolic N (~399.6 eV), quaternary (i.e., graphitic) N (~401.3 eV), and N-oxides of pyridinic N (~403.8 eV) [42, 119, 120]. Specially, pyridinic N refers to N atoms at the edge of graphene planes, where each N atom is bonded to two carbon atoms and donates one p-electron to the aromatic π system. Pyrrolic N locates at five-membered ring, where each N atom bonds with two carbon atoms and donates two p-electrons to the π system. Quaternary N refers to N atoms that replace the carbon atoms in the graphene hexagonal-ring. N-oxides of pyridinic N refers to N atoms bonds with two carbon atoms and one oxygen atom [42, 121]. Although a higher mass ratio between urea and GO gives a higher total nitrogen content of NG, the contents of oxidized N are similar in all NG samples, suggesting that nitrogen doping with urea is mainly achieved in the form of pyridinic, pyrrolic and graphitic N, while the contents of the other three types of N are different and the proportions do not change regularly. It is reported that electrical conductivity of nitrogen-doped graphene decreases upon the incorporation of nitrogen into graphene lattice [119, 122]. However, the graphitic N existing in graphene could improve the conductivity of the materials, which is favorable for electron transfer through the nitrogen-doped graphene during the charge-discharge process [119, 123]. Therefore, the sample N_2G may have the highest conductivity because of its high graphitic N content, while N_4G may give poor conductivity due to the high pyridinic N content, suggesting that more defects existed in N_4G.

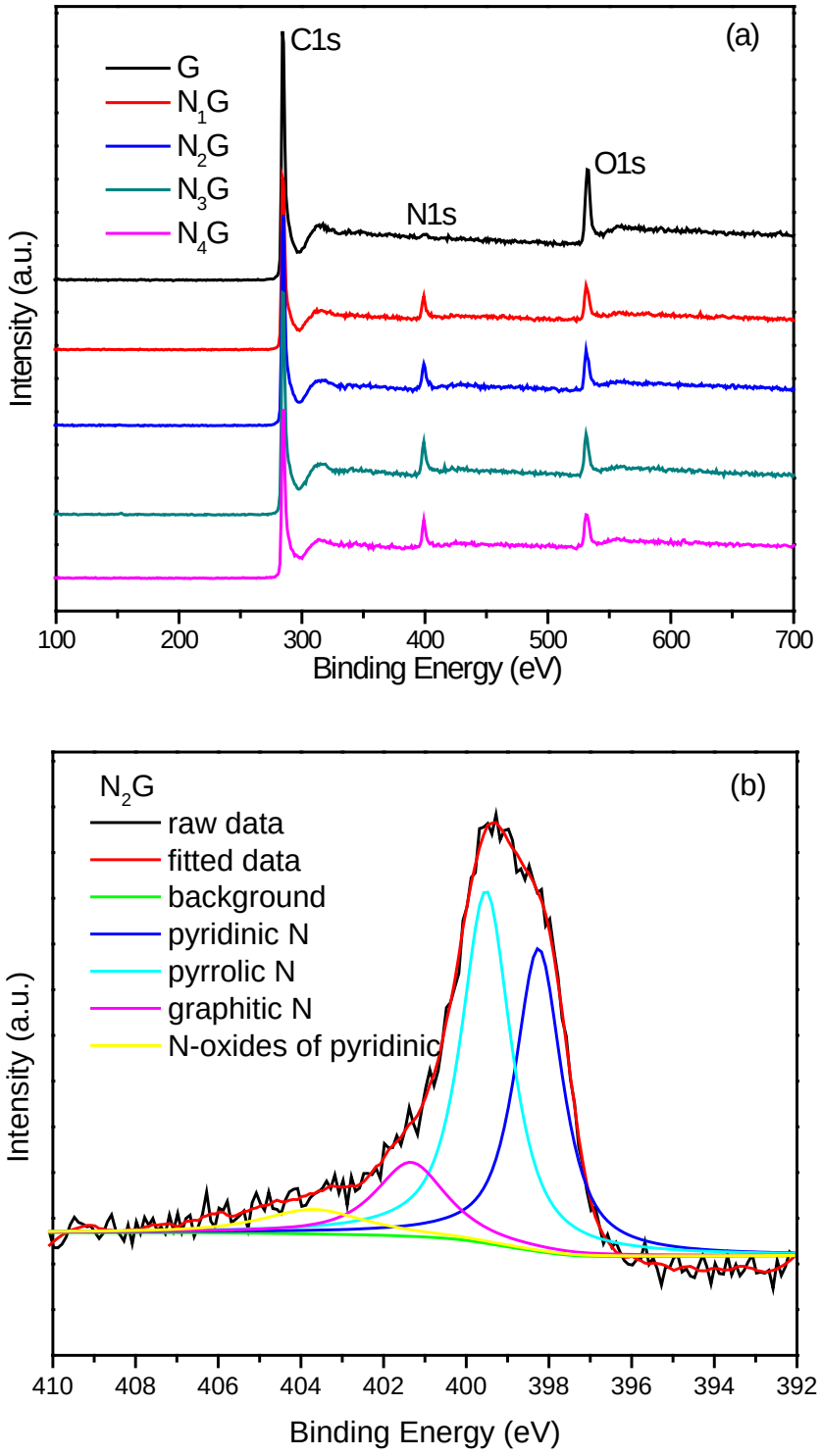

Figure 3.1 (a) XPS survey spectra of G, N_1G, N_2G, N_3G and N_4G. (b) High-resolution N1s spectrum of N_2G.

The incorporation of nitrogen in the graphene surface not only changes the surface chemical properties, but also changes the structural properties. Raman spectroscopy, a powerful method to evaluate the level of graphene defects, was carried out in this section to evaluate the quality of NG samples. The results are displayed in Figure 3.2. The data of graphene was used as reference. Two bands at ~1350 cm^{-1} and ~1590 cm^{-1} were clearly visible in the spectra of all samples, which can be assigned to D-band and G-band, respectively. The D-band was associated with the defect numbers of graphene layer such as edges, non-six-atom rings, and heteroatom doping and functionalities, while the G band was attributed to the E_{2g} phonon of sp^2-bonded graphitic carbons [42, 116]. The broad peak at around 2700 cm^{-1} indicated that the present synthesis method gave few-layers of graphene[117]. Therefore the intensity ratio of D band and G band (I_D/I_G) can reflect the defective level in graphene. Generally, a high ratio shows a high concentration of defects[124]. I_D/I_G ratios for different samples were listed in the Table 3.1. As can be seen, the addition of urea led to an increase of I_D/I_G value from 1.05 of graphene to 1.06~1.12 of NG, which indicated that the NG possess more defects than the graphene due to the incorporation of nitrogen in graphene lattice. Much higher I_D/I_G values was obtained with the increase in nitrogen amounts, indicating more nitrogen atoms were doped into the graphene matrix.

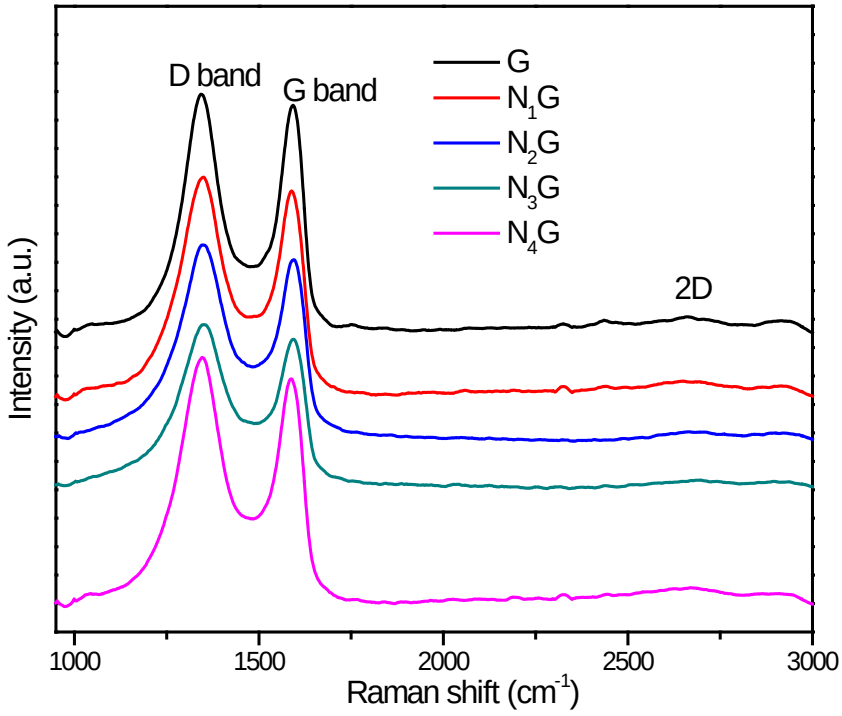

Figure 3.2 Raman spectra of G and NG samples.

The BET surface areas of different samples were measured and the results are presented in Table 3.1. Graphene had a BET surface area of 150.6 m^2/g after freeze-dried process. This value was much lower than the theoretical calculation value for a single graphene sheet (>2600 m^2/g), which could be attributed to the random agglomeration or restacking of the graphene layers during hydrothermal process [125]. The N_1G, N_2G, N_3G, and N_4G samples had a BET surface area of 154.8, 161.1, 135.7, and 102.5 m^2/g, respectively. It's obvious that surface area of NG slightly increased with increasing nitrogen amounts in NG surface until the mass ratio of urea/GO was up to 50:1, indicating a nitrogen doping process could prevent the aggregation of adjacent graphene layers [123, 126]. However, the S_{BET} decreased once the urea the mass ratio of urea/GO was increased to 100:1. Since the addition of urea not only led to nitrogen doping, but also enhanced the reduction of GO during the hydrothermal process [123]. In the case of high urea

concentration, the oxygen functional groups in GO were moved more effectively by urea addition, which led to rapid aggregation of graphene layers and lower surface areas of NG.

The morphology and structure of graphene and NG were characterized via SEM and TEM. Figure 3.3a and 3.3b clearly show a randomly oriented petal-like microstructure and wrinkles on graphene layers, a typical graphene structure, which was similar to those found in the literature for hydrothermal reduced GO [63, 127]. Like pristine graphene, N_2G were randomly and loosely stacked together displaying white fungus structure as shown in Figure 3.3c by SEM image. Lightly folded and crinkled graphene nanosheets were witnessed by TEM image in Figure 3.3d, which could be ascribed to the distortion of carbon lattice induced by the simultaneous GO reduction and nitrogen doping processes [63, 116]. Additionally, TEM image of N_2G had a low contrast under the electron beam, suggesting a less thickness of N_2G. Therefore, NG with appropriate nitrogen content obtained by this hydrothermal method could well maintain graphene morphology and structure. Such structures, providing high specific area, abundant exposed active sites, better electrolyte permeability and mass transport, are highly desirable for electrocatalysis process [128, 129]. However, N_4G with high nitrogen doping content illustrated flake-like graphite bulks (Figure 3.3 e) and its TEM image exhibited fragile and thick layers of graphene nanosheets (Figure 3.3 f), which indicated that inherent graphene structure of NG had been destroyed by excessive nitrogen doping and couldn't meet the requirements of an electrocatalyst support. Such morphology and structure results were consistent with aforementioned BET surface area data.

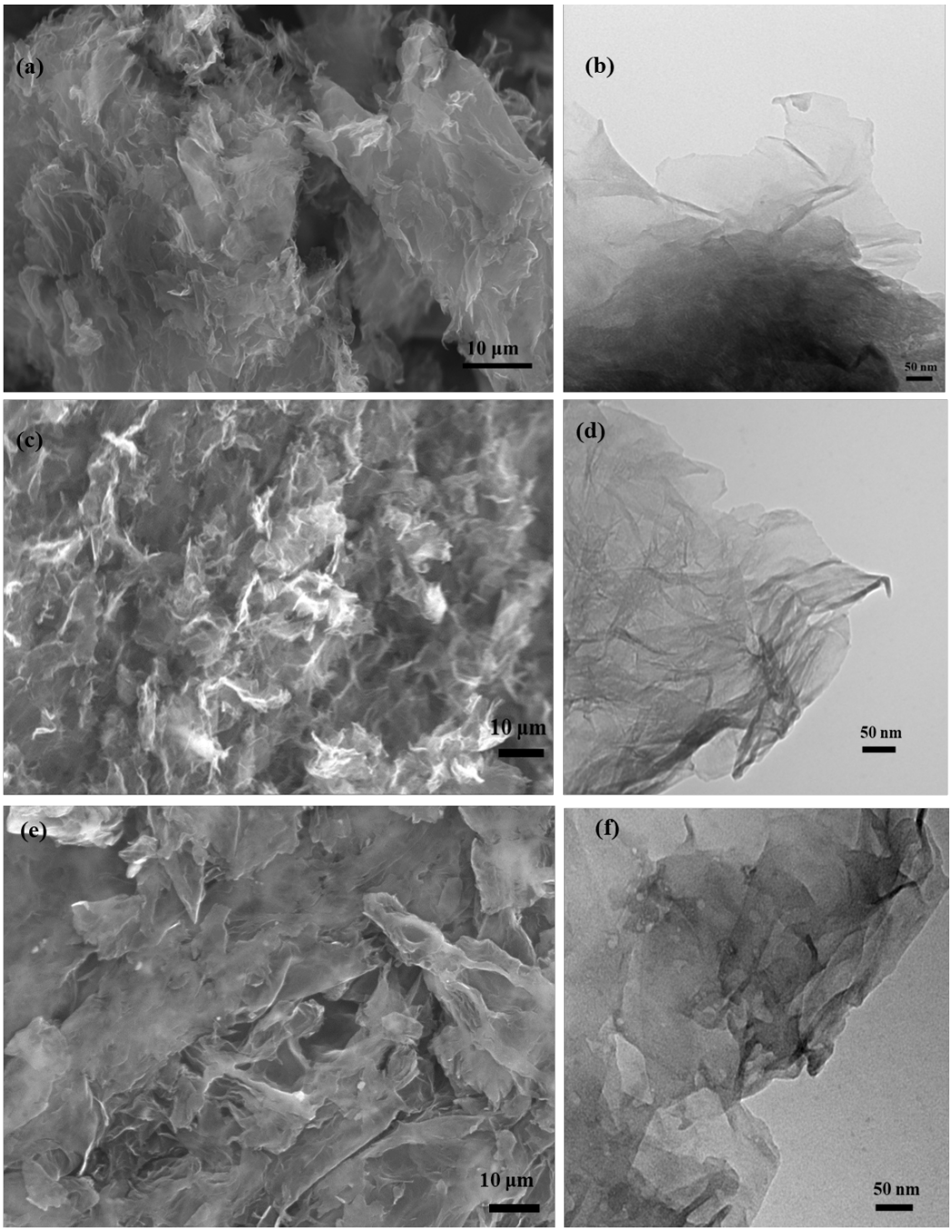

Figure 3.3 SEM and TEM images of G and NG. (a) (c) (e) SEM images of G, N_2G, N_4G. (b) (d) (f) TEM images of G, N_2G, N_4G.

3.3.2 Characterization of PN-NG

FTIR spectra (Figure 3.4) confirmed the formation of PN on NG and graphene sheet after CV synthesis. The spectra of all samples exhibited a clear peak at around 2050 cm^{-1}, which was determined as the characteristic peak of N_8^- in our previous study [75], demonstrated that polynitrogen chain N_8^- were successfully synthesized on all graphene and NG substrates. In addition, the peak intensity of 2050 $cm^{-1}$from PN-N_2G sheet sample was the strongest, while the peak intensity followed the order of PN-N_2G sheet > PN-N_1G sheet > PN-G sheet > PN-N_3G sheet > PN-N_4G sheet. The peak near 2100 cm^{-1} can be assigned to the azide ion asymmetric stretching mode from unreacted sodium azide [75]. Peaks around 1630 cm^{-1} and 3300 cm^{-1} are from residual water trapped in the graphene sheet [75].

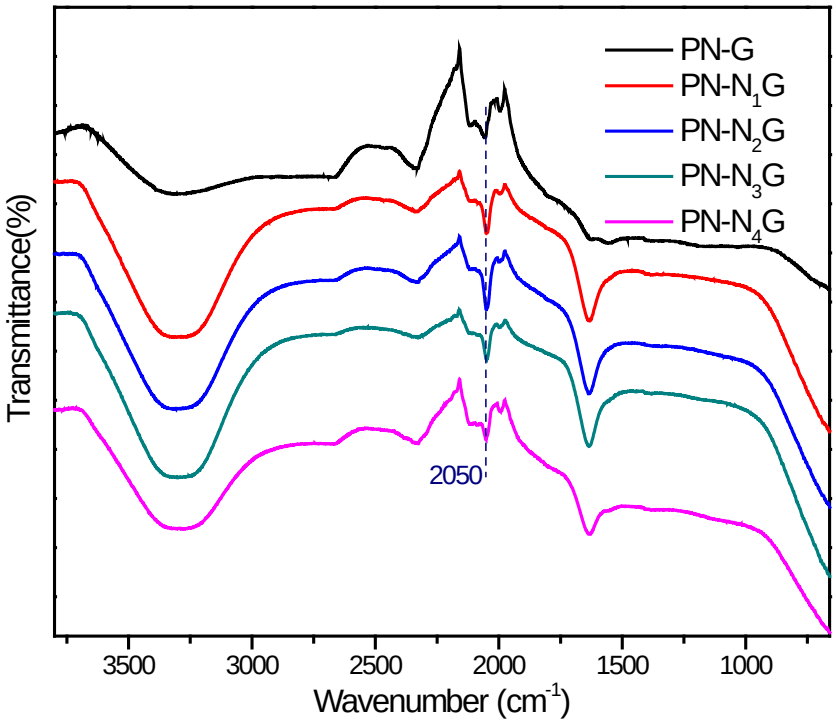

Figure 3.4 FTIR spectra for PN-NG samples. The graphene (or NG) backgrounds have been subtracted from the samples.

TPD was performed to investigate the thermal stability of the PN samples and the results are shown in Figure 3.5 and Table 3.2. The TPD spectra of the PN sheets suggested that the polynitrogen species N_8^- on the graphene and NG substrates were thermally stable and did not decompose until 400 ^oC. The nitrogen desorption amount from the decomposition of N_8^- followed the order of PN-N_2G sheet > PN-N_1G sheet > PN-G sheet > PN-N_3G sheet > PN-N_4G sheet, which was consistent with FTIR results, suggesting that a moderate incorporation of nitrogen in graphene lattice could improve the synthesized N_8^- amount. Since nitrogen doping could increase the electropositivity of adjacent carbon by electron clouds shifting from carbon to nitrogen, which further enhanced the charge transfer interaction between NG and the polynitrogen chain N_8^- (PN). It led to more PN stabilized on NG substrate. However, an excess of nitrogen doping resulted in more defects in its microstructure that led to a low conductivity of N_4G, which had negatively effects on the production of PN during the electrochemical oxidation from azide, such that less N_8^- produced and more N_3^- would be residual on the high nitrogen content graphene matrix of N_4G. Another hand, surface area and microstructure of NG as described above by the BET, SEM and TEM measurements, indicating that N_3G and N_4G with high amount of nitrogen doping had low surface areas and compactly stacked bulks. In such structures, a part of positively charged carbon sites adjacent to doped nitrogen, as “active sites” to stabilize the PN chain, were wrapped between the graphene layers and became inaccessible for PN stabilization. As a result, a lower amount of N_8^- was obtained on N_3G and N_4G. By contrast, the high surface area and loosely stacked graphene structure of N_2G exposed more active sites for PN chain stabilization, with harvesting of a higher amount of synthesized N_8^-.

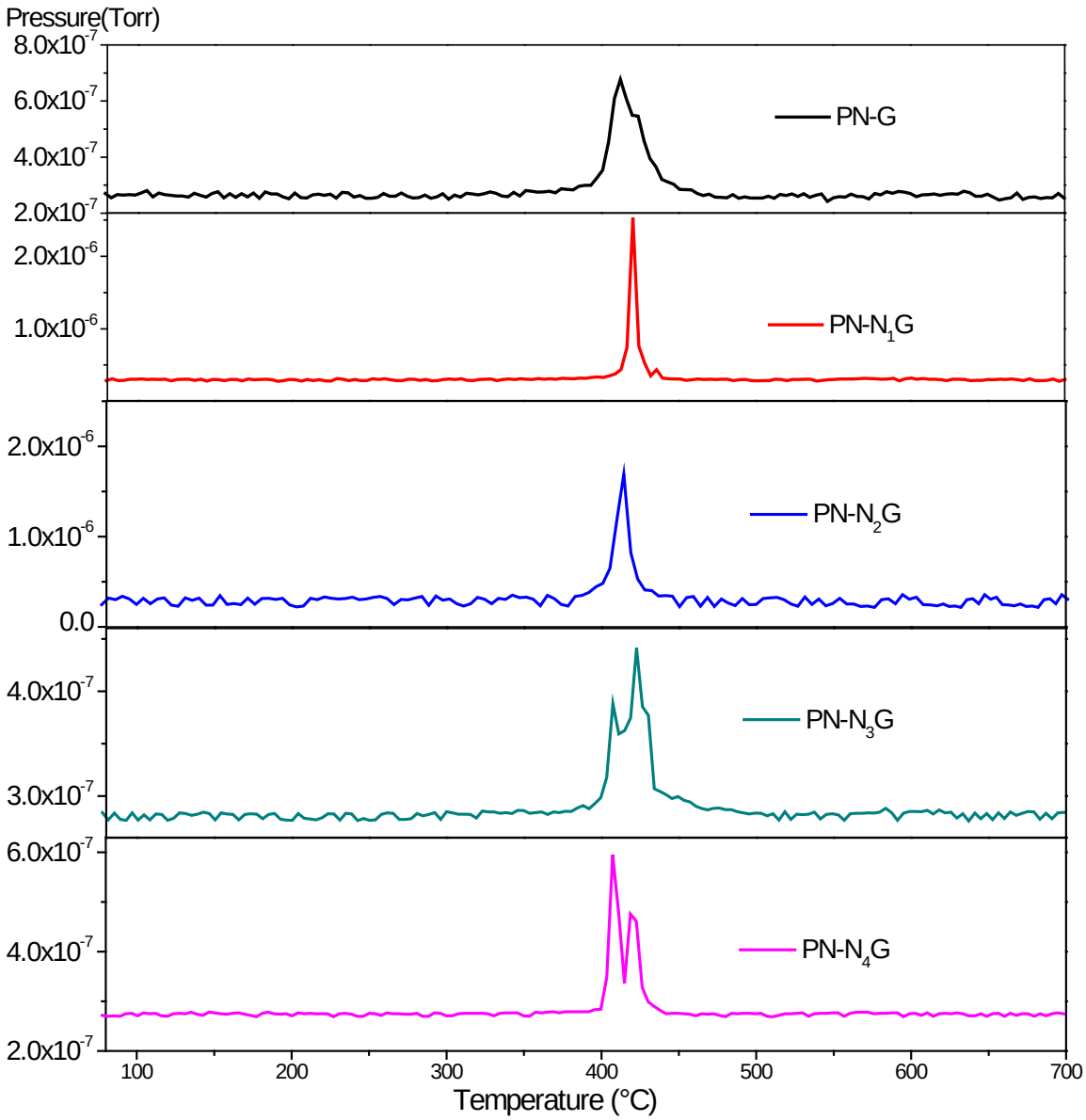

Figure 3.5 N^{14} signal from TPD scans for PN-NG samples. The curves have been normalized by sample weight.

Table 3.2 Nitrogen Desorption Amount (mmol/grams of sample)

Entry	Sample	Nitrogen desorption amount [a]
1	PN-G sheet	0.78
2	PN-N_1G sheet	0.86
3	PN-N_2G sheet	1.10
4	PN-N_3G sheet	0.47
5	PN-N_4G sheet	0.44

[a] calculated by integration of the TPD results and comparing the peak areas with those from injection of pure nitrogen under the same experiment conditions.

3.3.3 Electrocatalytic performance

Linear sweep voltammetry (LSV) measurements were carried out on a rotating disk electrode (RDE) at different rotating speeds to evaluate the electrocatalytic performance over PN-G and PN-NG electrodes. A series of ORR polarization curves from 900 to 4500 rpm at different catalysts (Figures 3.6a~e) show a typically increased current density with increasing rotation speeds. Moreover, an enhanced current density followed the order of PN-N_4G-GCE < PN-N_3G-GCE < PN-G-GCE < PN-N_1G-GCE < PN-N_2G-GCE at a certain potential. This current density sequence was in good agreement with that for synthesized N_8^- amounts confirmed from FTIR and TPD. The more N_8^- amount gave the higher current density, indicating that the enhancement of ORR activity comes from the increasing amount of N_8^-, the active species for ORR. This result was also in good agreement with our previous study, the larger amount of N_8^- deposited on MWNT substrate, the more accessible active sites the PN-MWNT electrode could provide for oxygen reduction on the surface, which led to better electrocatalytic activity of ORR[75].

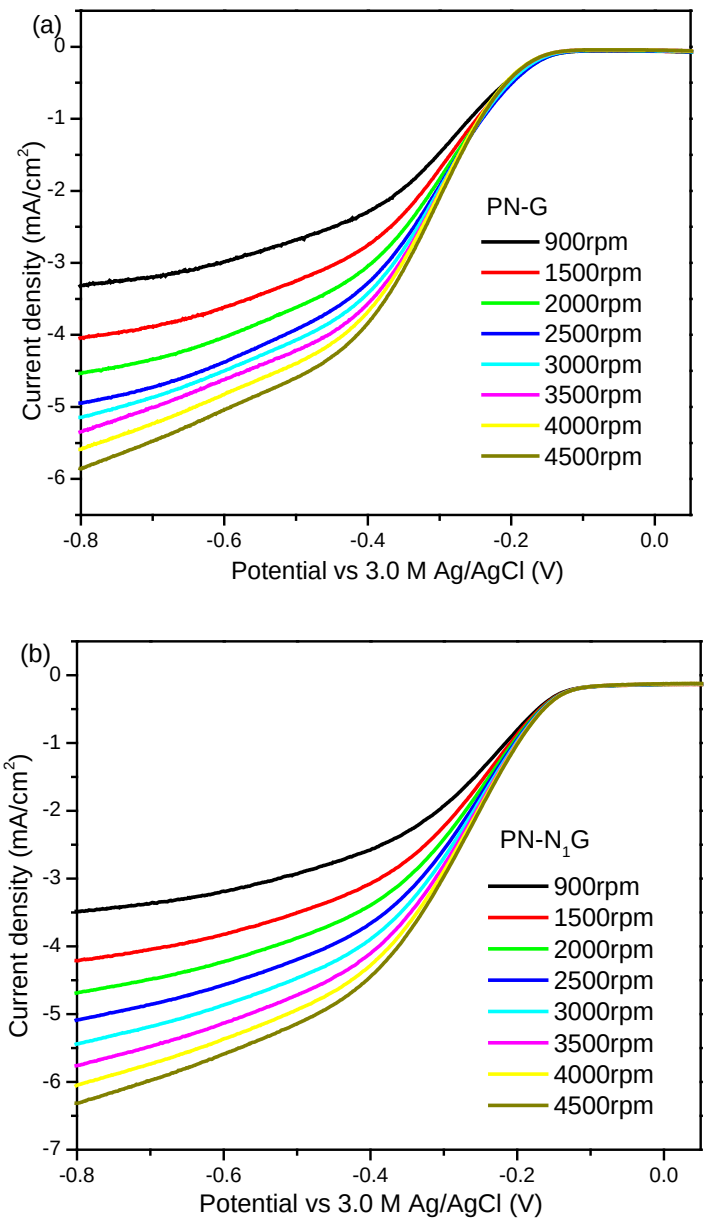

Figure 3.6 LSV curves of ORR on PN-NG samples at different rotation rates in oxygen-saturated 0.1 M KOH solution (scan rate: 5 mV/s). (a) PN-G-GCE, (b) PN-N_1G-GCE, (c) PN-N_2G –GCE, (d) PN-N_3G –GCE, (e) PN-N_4G –GCE . (Continued)

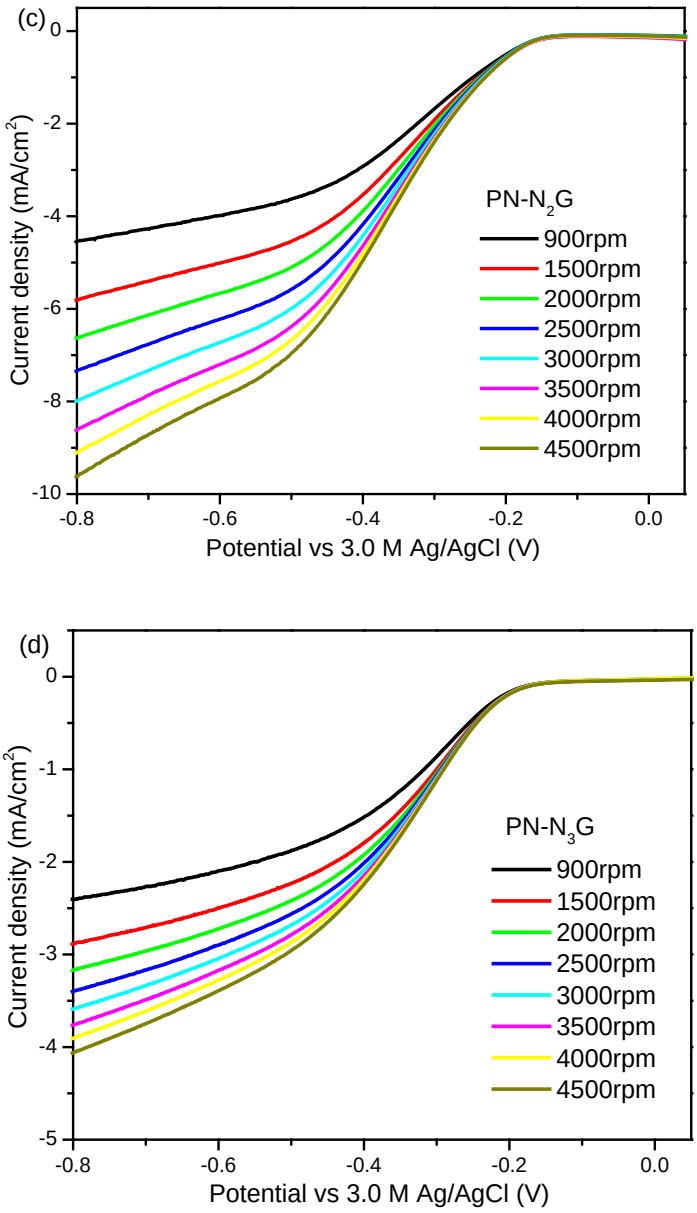

Figure 3.6 LSV curves of ORR on PN-NG samples at different rotation rates in oxygen-saturated 0.1 M KOH solution (scan rate: 5 mV/s). (a) PN-G-GCE, (b) PN-N_1G-GCE, (c) PN-N_2G –GCE, (d) PN-N_3G –GCE, (e) PN-N_4G –GCE . (Continued)

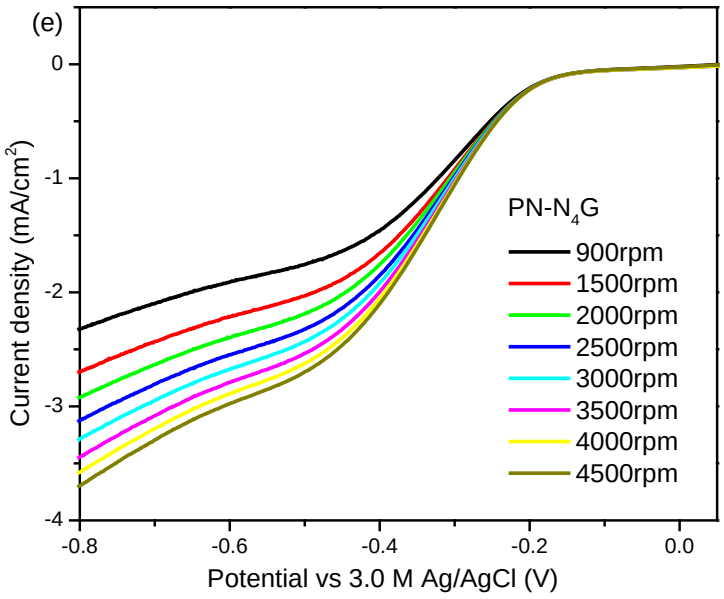

Figure 3.6 (Continued) LSV curves of ORR on PN-NG samples at different rotation rates in oxygen-saturated 0.1 M KOH solution (scan rate: 5 mV/s). (a) PN-G-GCE, (b) PN-N_1G-GCE, (c) PN-N_2G –GCE, (d) PN-N_3G –GCE, (e) PN-N_4G –GCE .

To gain further insight into the kinetics of oxygen reduction reaction on PN-G and PN-NG electrodes, the transferred electron number per oxygen molecule involved in the ORR process was determined by the Koutecky-Levich (K-L) equation [23, 121], which relates the current density J to the rotation rate of the electrode ω. Figures 3.7a~e exhibit the Koutecky-Levich (K-L) plots of 1/J vs. $1/\omega^{0.5}$ obtained at various potentials for all four samples. The linear and parallel fitting lines implied a first-order reaction toward the concentration of dissolved oxygen and similar electron transfer numbers for ORR in the selected potential range [93, 130, 131]. For PN-G-GCE electrode, the values of n were derived to be 3.7-3.8 at the potential ranging from -0.6 to -0.8 V, indicating a four-electron process dominated ORR on N_8^- [89, 93]. For both PN-N_1G-GCE and PN-N_2G-GCE electrodes, n values were determined to be 3.7-3.9 and 4.0-4.2, respectively. These results indicated that PN-N_1G-GCE and PN-N_2G-GCE also favored a four-electron reduction

process. For PN-N_3G-GCE and PN-N_4G-GCE electrodes, the n values were 2.6-3.1 and 2.7-2.9, which revealed that the ORR on these two samples had two pathways, the two-electron pathway (as discussed in following section) on N_3^- and the four-electron pathway on N_8^- [90, 117], in consideration of coexisting of a large amount of residual N_3^- and a small amount of produced N_8^- on PN-N_3G-GCE and PN-N_4G-GCE as revealed by FTIR and TPD.

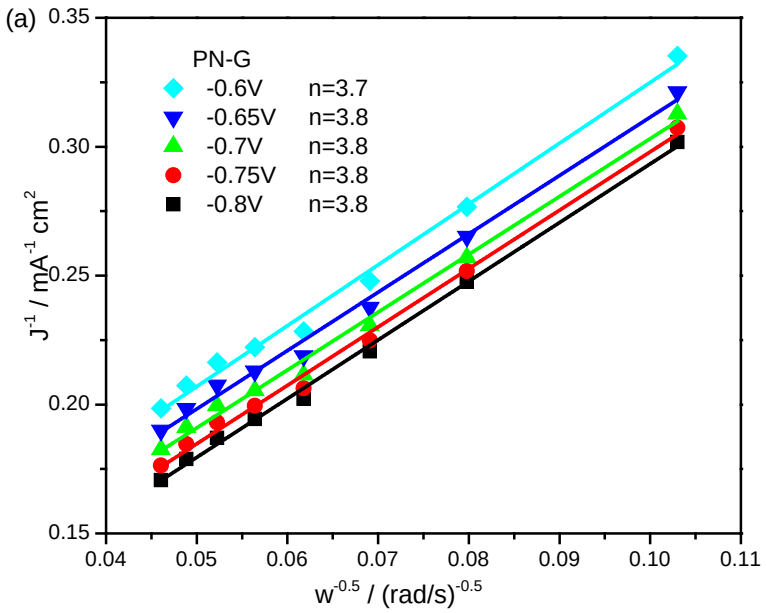

Figure 3.7 Koutecky-Levich Plots for PN-NG samples at different potentials. (a) PN-G-GCE, (b) PN-N_1G-GCE, (c) PN-N_2G –GCE, (d) PN-N_3G –GCE, (e) PN-N_4G –GCE. (Contiuned)

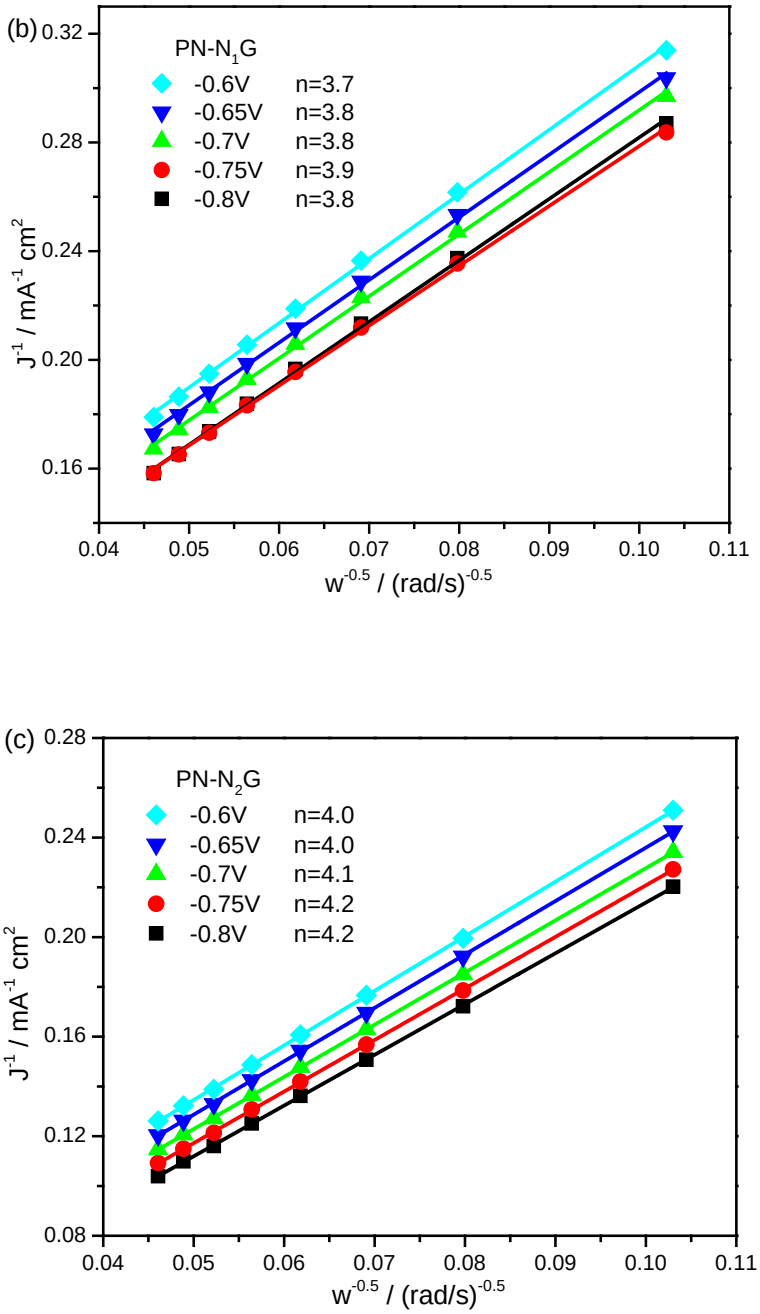

Figure 3.7 Koutecky-Levich Plots for PN-NG samples at different potentials. (a) PN-G-GCE, (b) PN-N_1G-GCE, (c) PN-N_2G –GCE, (d) PN-N_3G –GCE, (e) PN-N_4G – GCE. (Contiuned)

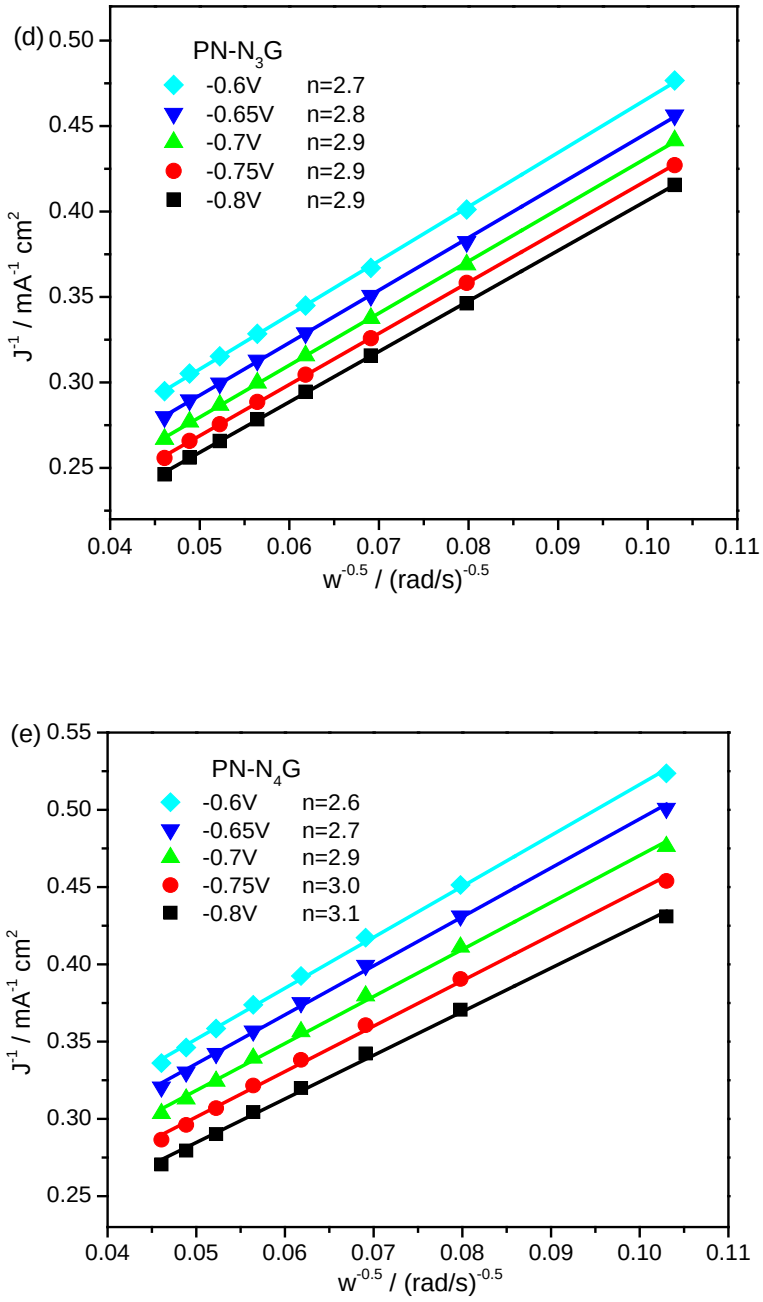

Figure 3.7 (Contiuned) Koutecky-Levich Plots for PN-NG samples at different potentials. (a) PN-G-GCE, (b) PN-N_1G-GCE, (c) PN-N_2G –GCE, (d) PN-N_3G –GCE, (e) PN-N_4G –GCE.

To confirm the hypothesis mentioned above, the electrocatalytic performance of several PN samples and graphene substrates were compared in Figure 3.8 and 3.9. The current density followed the order of PN-N_2G-GCE > N_2G-GCE > PN-G-GCE >

NaN_3-N_2G-GCE > G-GCE. The electrons transferred number n (Figure 3.9) for ORR on G, NaN_3-N_2G and N_2G were found to be 2.5-2.9, 2.6-3.0 and 3.5-3.9 in the potential range of -0.6V~-0.8V, confirming the two-electron pathway over N_3^- and G. Comparing the current densities and n for the same carbon supports with and without PN deposition (PN-N_2G-GCE & N_2G-GCE, PN-G-GCE & G-GCE), PN catalyst contributed appreciably to the ORR activity enhancement. Comparing the current densities and n for PN catalysts with and without nitrogen doping in carbon support (PN-N_2G-GCE and PN-G-GCE), the increased current density should be ascribed to the nitrogen doping. Obviously, the synergistic effect between PN and NG had greatly enhanced the ORR performance on PN-N_2G-GCE electrode.

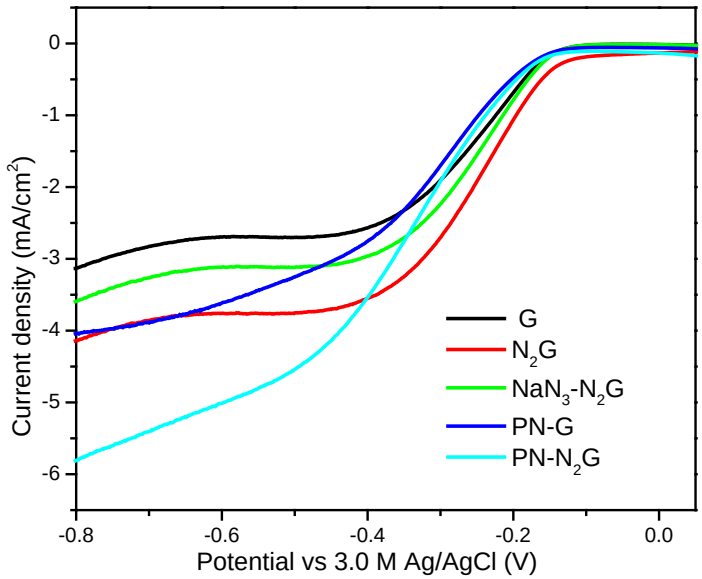

Figure 3.8 LSV curves of ORR on G-GCE, N_2G-GCE, NaN_3-N_2G-GCE, PN-G-GCE, and PN-N_2G-GCE electrode in an Oxygen-saturated 0.1 M KOH solution with a rotation speed of 1500 rpm (scan rate: 5 mV/s).

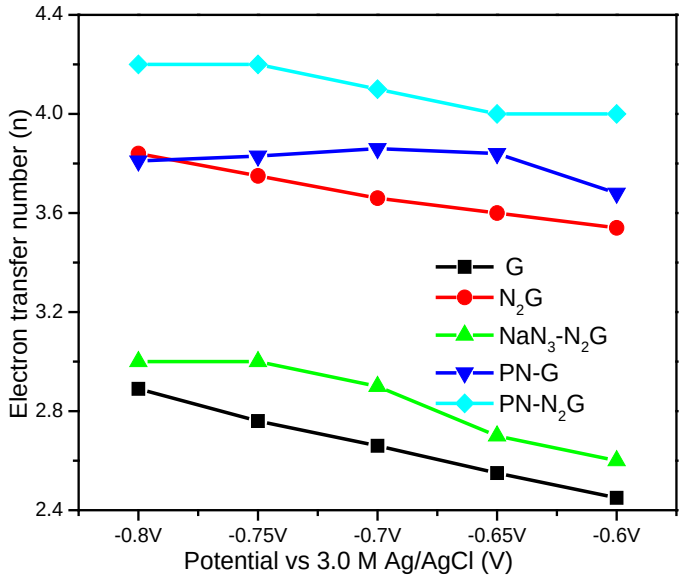

Figure 3.9 Electron transfer number n of G-GCE, N_2G-GCE, NaN_3-N_2G-GCE, PN-G-GCE, and PN-N_2G-GCE calculated from Koutecky-Levich equation.

To clarify the oxygen reduction mechanism at the PN samples over graphene and NG matrix, natural bonding orbital (NBO) analysis was applied to investigate the chemisorption mode of O_2. Our previous study [75] calculated the partial charge distribution on chain structure N_8^- species and the results indicated the most active sites should be N1 and N2 locating in the center of the chain with adjacent position. Both of them had more negative charges than other nitrogen atoms in the chain (See Figure 2.7 in chapter 2), where oxygen would be activated via direct bonding with the electrons of the N1 and N2 [47, 75]. Moreover, the existence of the two adjacent active sites made it's reasonable to propose a parallel diatomic adsorption (side-on adsorption, Yeager model) of oxygen onto the N_8^- during ORR. In this case, the O-O bonding would be effectively weakened and easily broken [12], which led to a four-electron transfer pathway in ORR [132, 133]. This result is highly in good agreement with the four-electron transferred number observed in above kinetic study over N_8^-. On the other hand, N_3^- is a linear

centrosymmetric anion and its two end nitrogen atoms have more negative charges [99, 100], where the single site adsorption occurred and the ruling chemisorption mode of O_2 would be the end-on adsorption (Pauling model). It would lead to a two-electron transfer pathway in ORR [132, 133]. This result is also consistent with the two-electron transferred number obtained in above kinetic study over N_3^-. In a word, the investigation of O_2 chemisorption mode on both N_8^- and N_3^- further confirmed the conclusion of the aforementioned kinetic study. The mechanism for oxygen reduction on N_3^- and N_8^- based on different O_2 chemisorption mode could be illustrated as Figure 3.10.

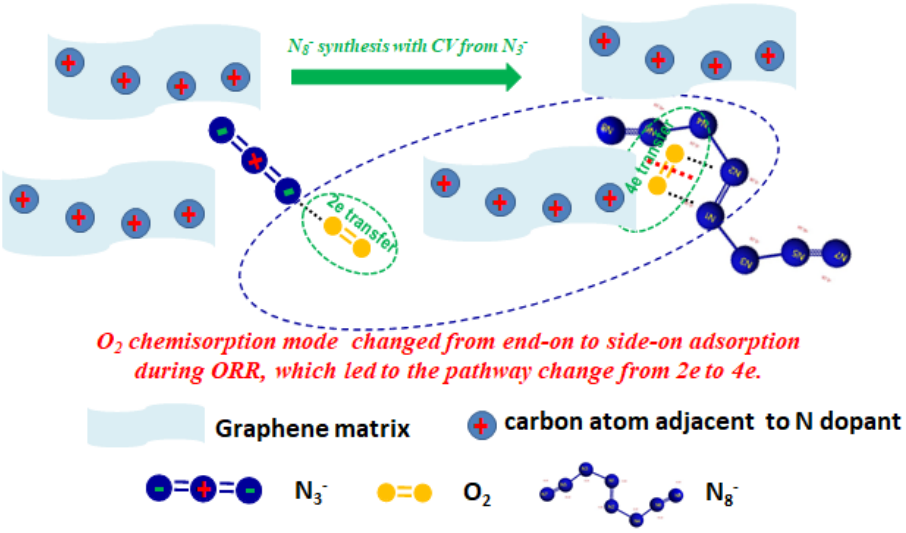

Figure 3.10 Proposed mechanism for the N_8^- synthesis on nitrogen-doped graphene and its high activity for oxygen reduction.

3.4 Summary

In this section, we demonstrated a strategy to design and prepare a total metal-free catalyst for oxygen reduction reaction. Nitrogen-doped graphene (NG) were prepared by a facile hydrothermal method with the mixture of graphene oxide and urea as catalyst support, and polynitrogen N_8^- (PN) deposited on nitrogen-doped graphene (PN-NG) were synthesized

by cyclic voltammetry (CV) and further used for oxygen reduction reaction (ORR). Compared to the graphene matrix, a larger amount of N_8^- was prepared on N_2G matrix, possibly because nitrogen doping could enhance the charge transfer ability from NG to the PN chain resulting into producing more PN on NG substrate. Moreover, a larger amount of N_8^- on N_2G provided more active sites for ORR, which enhanced the ORR current density. However, in case of an excessive amount of nitrogen doping, the decrease of the conductivity and surface area of NG matrix led to less N_8^- produced and more N_3^- would be residual on the high nitrogen doping matrix of N_4G. Kinetic study revealed that it was through a one-step four-electron process over N_8^-, which was further confirmed by the side-on O_2 chemisorption mode. The electrodes fabricated by N_8^- stabilized on nitrogen doped graphene provide promising prospects as metal-free ORR catalysts in alkaline solution.

CHAPTER 4

N_8^- POLYNITROGEN STABILIZED ON BORON DOPED GRAPHENE AS METAL-FREE ELECTROCATALYST FOR OXYGEN REDUCTION REACTION

4.1 Introduction

Boron atoms, having a comparable atomic size and three valence electrons for binding with carbon atoms, could be incorporated into the carbon matrix [110, 112, 134]. In B-doped graphene, electron transfer happened from B to C due to the lower electronegativity of B (2.04) than C (2.55). This will result into a generation of partial positive charge on B atom and lead to more facile electron transfer, which will become the active centers for the stabilization of polynitrogen N_8^- (PN) chain [75]. In this section, for the first time, polynitrogen N_8^- deposited on reduced graphene oxide (PN-G), boron-doped graphene (PN-BG) were synthesized using cyclic voltammetry method. Graphene and boron doped graphene with tunable boron content of 1.23-2.78 atom% were used as the substrates, which were prepared by a facile hydrothermal method. The PN samples were further tested as cathode catalysts for oxygen reduction reaction (ORR) in alkaline solution. The optimal PN-BG catalyst showed high activity via a four-electron pathway, making it a promising candidate as ORR electrode material.

4.2 Experimental

4.2.1 Synthesis of boron-doped graphene

All the materials and chemicals were commercially available and were used without further purification. Graphite oxide was synthesized from graphite powder following a modified Hummers method according to previously reported work [118]. Then it was dispersed into deionized water and sonicated for 30 mins to exfoliate oxidized graphite particles to graphene oxide (GO) colloid solution.

Boron-doped graphene (BG) was synthesized via hydrothermal method in the presence of $NaBH_4$ [135]. Briefly, a 15 mL of $NaBH_4$ aqueous was gradually added into the 100 mL of prepared GO colloid solution then the mixture solution was thoroughly stirred for 30 min at room temperature. The concentration of $NaBH_4$ solution was obtained by adjusting mass ratio of Boron/(Boron+Carbon) (2.5, 5, 20%). After that, the solution was transferred into a 200 mL Teflon-lined stainless steel autoclave for hydrothermal treatment at 180 ℃ for 12 h and then cooled to room temperature naturally. The precipitate was separated by centrifugation and washed several times with deionized water and absolute ethanol, respectively. Obtained BGs were dried in a vacuum oven at 60 °C overnight. Herein, three BG samples with boron content of 1.23, 2.01, and 2.87 at%, as determined by X-ray photoelectron spectroscopy (XPS), were denoted as B_1G, B_2G, and B_3G, respectively (Table 1). For comparison, reduced graphene oxide (rGO, graphene) was synthesized under the same hydrothermal condition in the absence of $NaBH_4$ and was denoted as G. Round-shaped BG (or G) sheets were fabricated by vacuum filtration of BG (or G) colloid dispersion with DMF as solvent and further used to synthesize PN-BG (or PN-G) sheet.

4.2.2 Preparation of PN electrode

Polynitrogen N_8^- electrode synthesis was performed by CV treatment with a three-electrode setup followed the same procedure as discussed in chapter 3 except using BG (or graphene) as substrates. BG (or graphene) ink was prepared by 10 mg BG (or graphene) powder ultrasonically dispersed into 5mL DMF containing a Nafion solution (0.5 wt%, DuPont). 5μL of the ink was coated onto the surface of a pre-polished glassy carbon electrode (GCE, 3.0 mm) denoted as BG-GCE (or G-GCE) and dried in air. Then GCE was dipped in 40mL 2M NaN_3 (Aldrich)-buffer solution (PH=4.0), which was used as the working electrode. Pt and Ag/AgCl were used as counter and reference electrode, respectively. Herein, the different boron doping content samples are denoted as PN-B_1G, PN- B_2G, and PN-B_3G respectively. The resulting PN-BG-GCE and PN-G-GCE electrodes were dried in air and used as the working electrodes for ORR test.

PN-BG (or PN-G) sheet were prepared under the same electrochemical conditions using round-shaped BG (or graphene) sheets as working electrode to produce large amount of PN sheet samples for following characterizations (i.e., FTIR and TPD).

4.2.3 Characterization of PN-BG

X-ray photoelectron spectroscopy (XPS), Raman, Brunauer-Emmett-Teller (BET), SEM, TEM, FTIR and Temperature programmed decomposition (TPD) were performed to characterize prepared BG substrate and PN-BG catalysts. The characterization details were the same as described in Chapter 3.

XPS measurements were performed on a Kratos Axis Ultra DLD multitechnique X-ray photoelectron spectroscopy. The binding energy for all samples was calibrated by reference C1s binding energy (284.8 eV). Raman spectroscopy was performed with a

Thermo Scientific DXR Raman microscope. SEM was performed on a Hitachi S-3400N scanning electron microscope and TEM was performed on a Hitachi H7500 transmission electron microscope. FTIR was carried out using a Nicolet ThermoElectron FTIR spectrometer combined with a MIRacle ATR platform assembly and a ZnSe plate, and denoted as ATR-FTIR. The BET specific surface areas of the graphene and BG were determined by N_2 adsorption/desorption at liquid nitrogen temperature using an AutoChem 2920 II (Micromeritics). TPD was carried out using the AutoChem II 2920 system. Samples were heated in flowing helium from room temperature to 850 °C at a heating rate of 10 °C /min. The released species were monitored with an on-line mass spectrometer (QMS 200, Stanford Research Systems).

4.2.4 Electrochemical measurements

The electrochemical tests on PN-BG samples were carried out in a rotating disk electrode (RDE) setup (ALS Co., Ltd) using linear sweep voltammetry (LSV) measurements. The measurement followed the same procedures as shown in Chapter 3.

For LSV measurements, the scanning rate is 5mV/s with various rotating speeds. PN-G-GCE and PN-BG-GCE electrodes were dried in air and used as working electrode directly. Pt and Ag/AgCl were used as the counter electrode and reference electrode, respectively. 0.1M KOH solution was used as electrolyte. Prior to the experiments, oxygen or nitrogen was bubbled into the electrolyte for at least 30 minutes until saturated; during the experiments, oxygen or nitrogen was flowed over the electrolyte to maintain saturation.

4.3 Results and Discussion

4.3.1 Characterization of BG

The boron content and boron bonding configuration in the graphene matrix were confirmed by XPS characterization. It was revealed that the atomic percentages of boron in three boron-doped graphene samples (B_1G, B_2G and B_3G) were 1.23%, 2.01%, and 2.87%, respectively (Table 4.1). It was worth noting that the boron doping content increased as the initial mass ration of $NaBH_4$ to GO dispersion increased.

Table 4.1 Parameters Derived from XPS, BET, and Raman Spectra Measurements

Sample	Mass ratio of boron /Carbon	Boron content measured by XPS	BET	Raman
		B (wt.%)	(m^2/g)	I_D/I_G
Graphene	0	-	150.5	1.05
B_1G	2.5	1.23	131.1	1.26
B_2G	5	2.01	108.3	1.37
B_3G	20	2.78	96.8	1.48

The high-resolution XPS spectra of B1s, C1s for BG samples were performed and displayed in Figure 4.1 (The sample B_1G was taken as an example.). The B1s binding energy (192.2 eV) for B_1G was higher than that for pure boron (187.0 eV) and lower than that of boron oxide (193.7 eV), suggesting that the boron atoms partially bonded to carbon atoms in sp^2-C network [111]. Furthermore, the B1s peak could be deconvoluted into two peaks at 192.05 eV and 192.35 eV, which were assigned to BC_2O and BCO_2, respectively,

two typical bonds in boron-doped graphene. The presence of BC_2O and BCO_2 bonds indicated boron atoms to replace carbon ones within graphene network and boron atoms doped at the defect sites, respectively. Compared to graphene, the two new peaks were observed on the C1s spectrum of B_1G, which could be assigned to C-B_1 and C-B_2 respectively [136, 137] indicating that boron atoms were bonded to carbon atoms in two types, which was consistent with the results of B1s. Moreover, the ratio of C-C was obviously decreased from 60.2% for graphene to 52.7% for B_1G, which resulted from the replacement of carbon atoms by boron atoms in graphene network. All of the above results demonstrated that boron atoms had been successfully doped into the graphene matrix during the hydrothermal process.

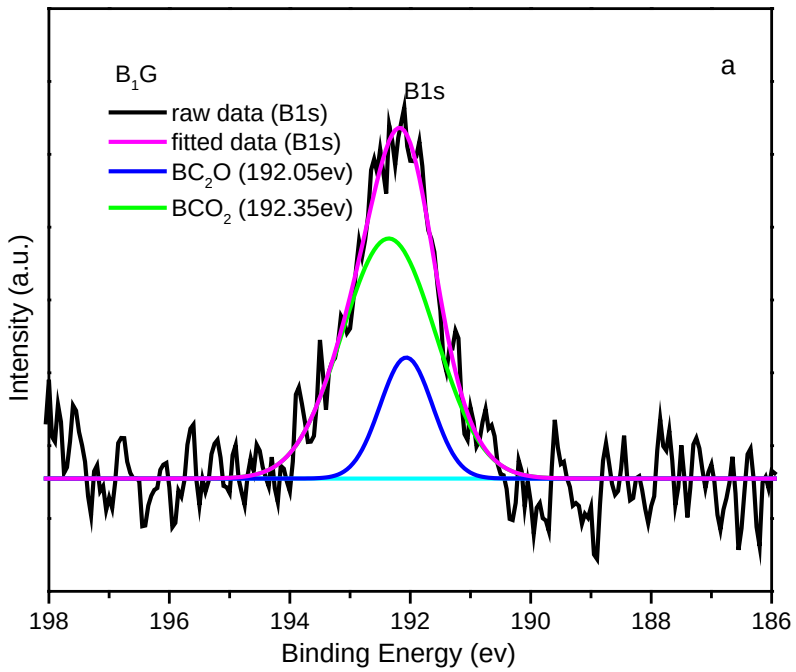

Figure 4.1 (a) B1s XPS spectra for B_1G, (b) C1s XPS spectra for graphene and B_1G. (Continued)

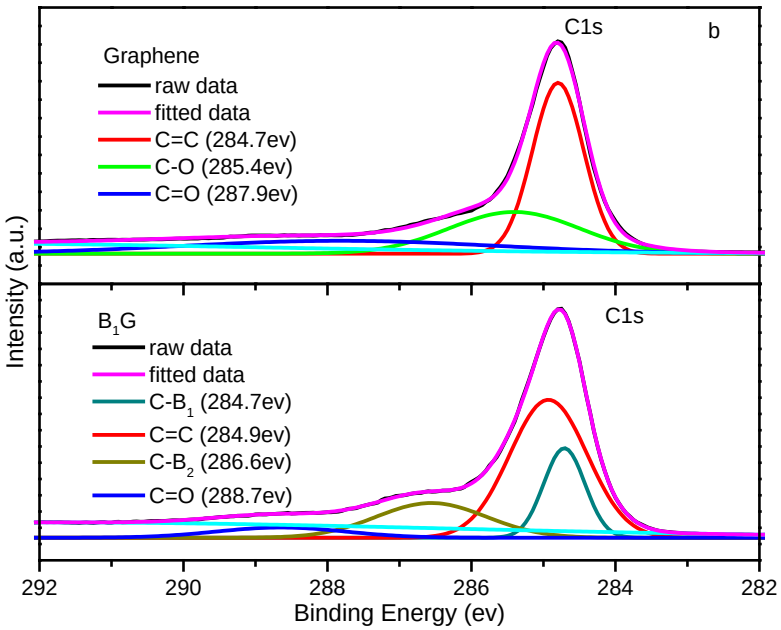

Figure 4.1 (Continued) (a) B1s XPS spectra for B_1G, (b) C1s XPS spectra for graphene and B_1G.

Raman spectroscopy was carried out to characterize the quality of boron-doped graphene samples. The results were displayed in Figure 4.2. The data of graphene was added as reference. Two characteristic peaks, D-band (1342 cm^{-1}) and G-band (1584 cm^{-1}), were observed on all samples. The intensity ratio between the D and G peaks (I_D/I_G) was widely used to reflect the defect level in graphene [124]. The I_D/I_G ratios for different samples were listed in the Table 1. Compared to graphene (1.19), BG samples held larger I_D/I_G value (1.26-1.48), indicating that the BGs possess many more defects than the graphene prepared under similar hydrothermal conditions due to boron doping. Furthermore, the increase of I_D/I_G ratio with the boron addition increase may suggest an increase in structural defects due to more boron doping into the graphene matrix in consideration of the same hydrothermal condition used.

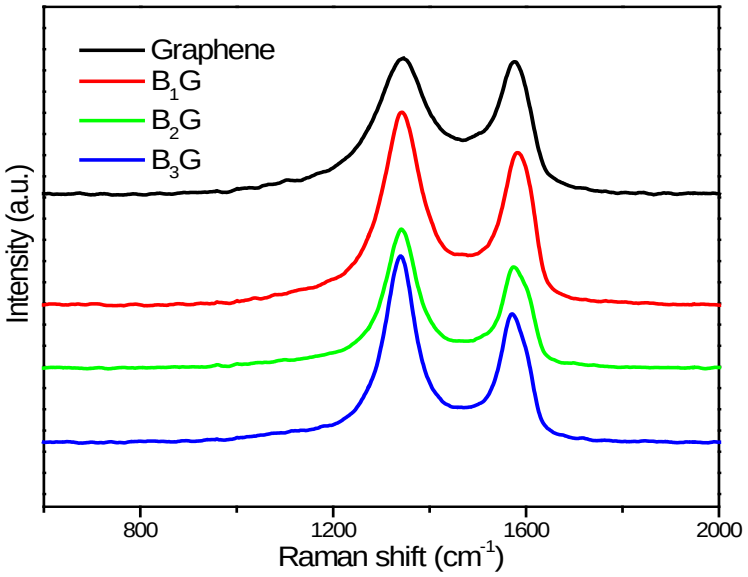

Figure 4.2 Raman spectra for G and boron-doped graphene.

The BET surface area of G, B_1G, B_2G and B_3G were observed to be 156.1, 131.1, 108.3, and 96.8m^2/g (Table 4.1), respectively which suggested that surface area of BG decreased with increase of the B content. One reasonable explanation is that in the case of high B content graphene, the introduction of B into the graphene network resulted in more residual oxygen groups of GO removing during the hydrothermal process. It led to prevailed recombination of the layers comparing to the low boron content graphene case, and consequently decreased the BET surface area.

The morphology of graphene and BG were characterized by SEM and TEM. Similar with typical graphene structures (Figure 3.3a and b), B_1G nanosheets are randomly and loosely stacked together displaying white fungus structure (Figure 4.3a). Its TEM image (Figure 4.3b) showed the wrinkled graphene sheet with a low contrast under the electron beam, indicating a thin thickness of B_1G. B_1G with low boron doping content could well maintain graphene morphology. In contrast, B_3G nanosheets with high boron

doping content were compactly stacked together (Figure 4.3c) and its TEM image exhibited fragile and thick layers of graphene sheet (Figure 4.3d). It suggests that the excessive amount of boron doping would destroy graphene structure, which may lead to the decrease of surface area and thus disable the advantage of being a catalyst support. These structural images are consistent with aforementioned BET surface area data.

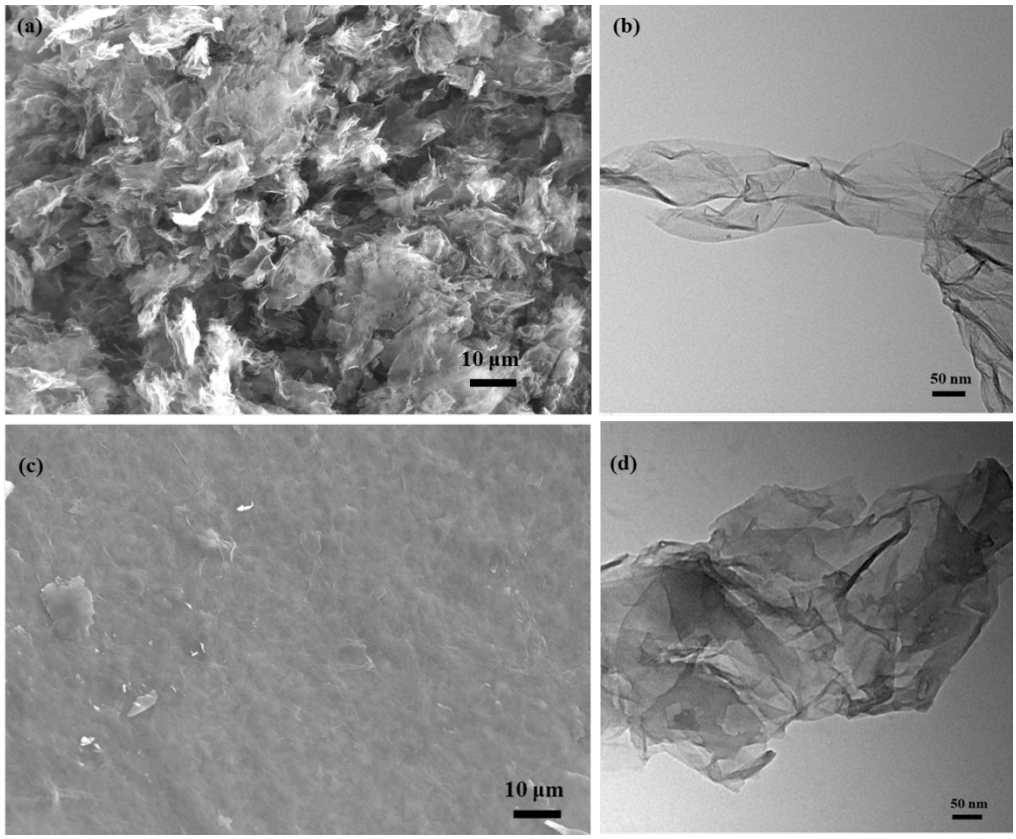

Figure 4.3 SEM and TEM images of BG (a) (c) SEM images of B_1G, B_3G, (b) (d) TEM images of B_1G, B_3G.

4.3.2 Characterization of PN-BG

The formation of PN on BG and graphene sheet after CV synthesis was confirmed by ATR-FTIR as shown in Figure 4.4. The clear line at ~ 2050 cm^{-1} was the characteristic peak of N_8^- [75], suggesting that polynitrogen chain N_8^- had been synthesized successfully.

Moreover, the peak intensity, which corresponds to the synthesized N_8^- amount, follows the trend PN-B_1G > PN-B_2G > PN-G > PN-B_3G. The line near 2100 cm^{-1} is assigned to the azide ion asymmetric stretching mode from unreacted sodium azide [75]. The peak intensity, which corresponds to the residual N_3^- amount, follows the trend PN-B_3G > PN-G > PN-B_2G > PN-B_1G. The lines around 1560 cm^{-1}, 1390 cm^{-1} and 1200 cm^{-1} can be attributed to C=C of the graphene skeleton, C-OH and epoxy C-O stretching vibrations respectively [138-140]. The lines around 1640 cm^{-1} and 3300 cm^{-1} are from residual water trapped in the graphene sheet [75].

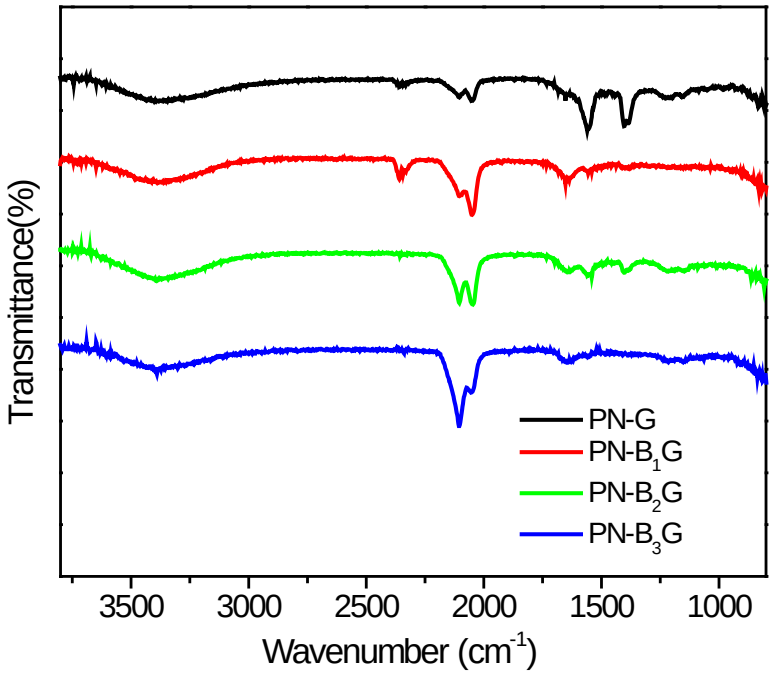

Figure 4.4 ATR-FTIR spectra for PN-BG samples. The graphene (or BG) backgrounds have been subtracted from the samples.

TPD results were shown in Figure 4.5 and Table 4.2. The TPD spectra of the PN sheets show that the polynitrogen species N_8^- on the graphene and BG substrates are thermally stable with decomposition temperature of 400 - 420 ^oC. Moreover, the desorption

amounts of nitrogen suggested that more N_8^- was synthesized on B_1G, while less N_8^- was observed on B_3G with trend of PN-B_1G > PN-B_2G > PN-G > PN-B_3G. Interestingly, two nitrogen desorption peaks were detected over PN-B_3G sample. The higher one corresponds to N_8^- stabilized on B_3G while the lower one can be attributed to azide deposited on B_3G. It was consistent with FTIR results, indicating that synthesis amount of N_8^- could be enhanced with the introduction of boron atoms in graphene network. Possibly, boron doping increased the electronegativity of carbon by electron clouds shifting from boron to carbon, which enhanced the charge transfer ability from BG to the nitrogen chain and resulted into producing more PN on BG. In the case of an excessive amount of boron doping, impurity scattering in the graphene lattice became more important. It led to the decrease of the conductivity [141, 142], which showed negatively effects on the production of PN from azide during the electrochemical oxidation process [75]. Therefore, less N_8^- produced and more N_3^- would be residual on B_3G due to the too high boron doping content. Another reasonable explanation was from the different surface area of BG samples demonstrated by the BET, SEM and TEM. The active sites to stabilize PN chain were wrapped inside the graphene layers over B_3G sample with high boron content, which became inaccessible for PN stabilization. As a result, it led to a lower amount of N_8^- synthesized. In contrast, B_1G, with high surface area, facilitated the exposure of active sites for PN chain stabilization, which resulted into a higher amount of N_8^-.

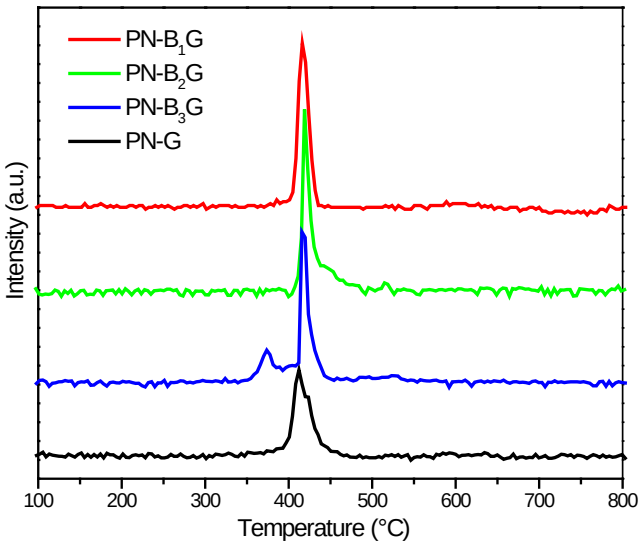

Figure 4.5 N^{14} signal from TPD scans for PN-BG samples. The curves have been normalized by sample weight.

Table 4.2 Nitrogen Desorption Amount (mmol/grams of sample)

Entry	Sample	Nitrogen desorption amount
1	PN-G sheet	0.78
2	PN-B_1G sheet	1.05
3	PN-B_2G sheet	0.87
4	PN-B_3G sheet	0.69

[a] calculated by integration of the TPD results and comparing the peak areas with those from injection of pure nitrogen under the same experiment conditions.

4.3.3 Electrocatalytic performance

To investigate the electrocatalytic performance at the PN-G and PN-BG electrode, linear sweep voltammetry (LSV) was measured in an O_2-saturated 0.1 M KOH electrolyte using a rotating disk electrode (RDE) at a scan rate of $5mVs^{-1}$. The ORR polarization curves at different rotating speeds are shown in Figure 4.6a~d. As expected, the catalytic current

density of all samples increased with increasing the electrode rotating speed due to the enhanced diffusion of electrolytes [89]. Moreover, the current density followed the trend of PN-B_1G-GCE > PN- B_2G -GCE > PN-G-GCE > PN-B_3G-GCE at a certain potential. This current density sequence was consistent with that for synthesized N_8^- amount harvested, which was observed in FTIR and TPD. It prompted us to establish the relationship between ORR activity and the amount of N_8^- formed on graphene and BG substrates, which is consistent with our previous study. It proved that the larger amount of N_8^- deposited uniformly on MWNT substrate the more accessible active sites the PN-MWNT electrode could provide for dissolved oxygen to be reduced on the surface, which led to the electrocatalytic activity enhancement [75].

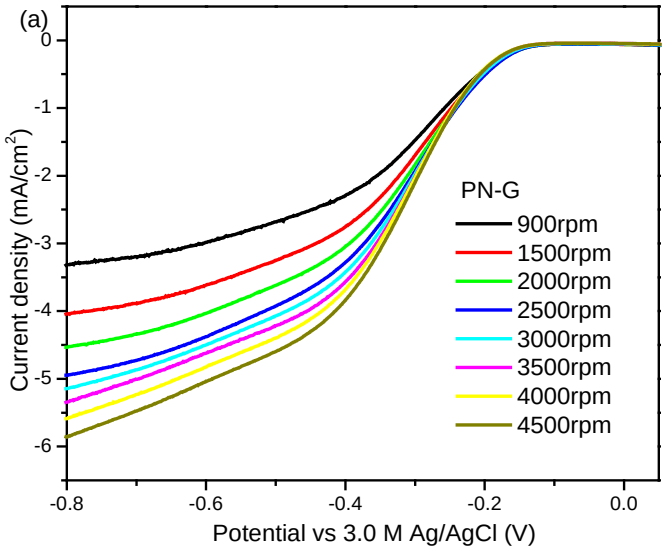

Figure 4.6 LSV curves of ORR on PN-BG samples at different rotation rates in oxygen-saturated 0.1 M KOH solution (scan rate: 5 mV/s). (a) PN-G-GCE, (b) PN-B_1G-GCE, (c) PN-B_2G –GCE, (d) PN-B_3G –GCE in an Oxygen-saturated 0.1 M KOH solution. (Continued)

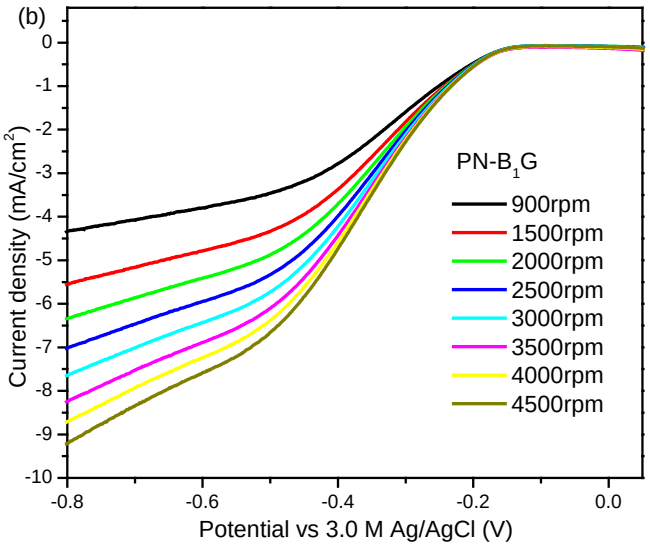

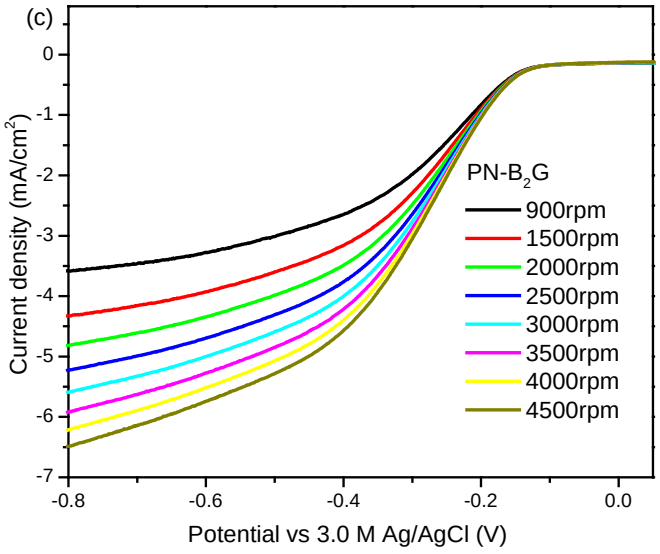

Figure 4.6 LSV curves of ORR on PN-BG samples at different rotation rates in oxygen-saturated 0.1 M KOH solution (scan rate: 5 mV/s). (a) PN-G-GCE, (b) PN-B_1G-GCE, (c) PN-B_2G –GCE, (d) PN-B_3G –GCE in an Oxygen-saturated 0.1 M KOH solution. (Continued)

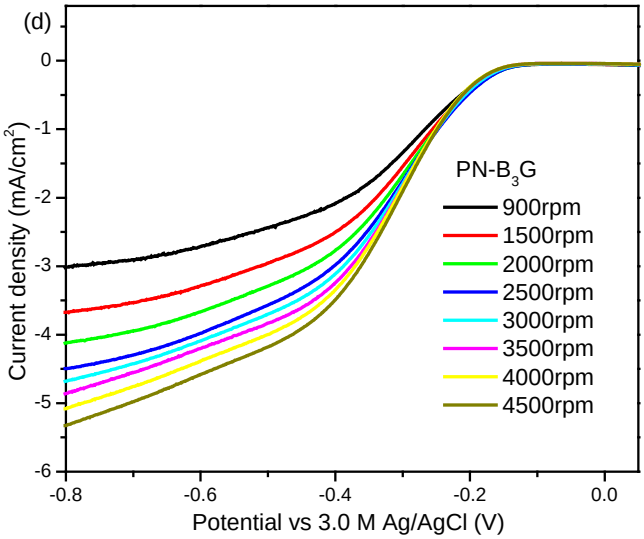

Figure 4.6 (Continued) LSV curves of ORR on PN-BG samples at different rotation rates in oxygen-saturated 0.1 M KOH solution (scan rate: 5 mV/s). (a) PN-G-GCE, (b) PN-B_1G-GCE, (c) PN-B_2G –GCE, (d) PN-B_3G –GCE in an Oxygen-saturated 0.1 M KOH solution.

Kinetics of the ORR process was evaluated by employing the Koutecky-Levich (K-L) equation [23, 90]. The Koutecky-Levich plots of 1/J vs. $1/\omega^{0.5}$ for all four samples are shown in Figure 4.7a~d. The fitting lines for all samples were well-linear and parallel, which indicated a first-order reaction toward dissolved oxygen [93, 130]. Moreover, the n value at the PN-G-GCE electrode was derived to be 3.7-3.8, which indicated that it was through a four-electron process on the N_8^- [89, 93]. The similar n values (3.8-4.0, and 3.8-3.9) were achieved on electrodes PN-B_1G-GCE and PN-B_2G-GCE respectively, which suggested that the pathways of both samples were also through a dominant four-electron process. This result, ORR on N_8^- through a four-electron transfer pathway, was highly consistent with the results of PN-MWNT and PN-NG discussed in previous chapter. However, the n value for PN-B_3G-GCE was 3.3-3.5 lying between the two-electron and four-electron reduction processes, which suggested that the ORR may

proceed by a coexisting pathway involving both the two-electron and four-electron transfers [53]. It can be attributed to the co-existence of N_3^- and N_8^- on PN-B_3G-GCE concluded by the above FTIR and TPD results. The former one went through two-electron transfer pathway (as discussed in following section) while the later one followed four-electron mechanism during ORR. To confirm the hypothesis, the electrocatalytic performance of several reference samples were further tested and illustrated in Figure 4.8 & Figure 4.9. Figure 4.8 showed an increased reduction current density in the order of PN-B_1G-GCE > PN- G-GCE > B_1G-GCE > NaN_3-B_1G-GCE > G-GCE. Clearly, the combination of PN and BG greatly enhanced the ORR performance. Moreover, electron transferred number n (Figure 4.9) of G-GCE, NaN_3-B_1G-GCE and B_1G-GCE were found to be 2.5-2.9, 2.6-3.0, and 3.4-3.7, respectively, in the potential range of -0.6V~-0.8V, which indicated the two-electron pathway over N_3^-.

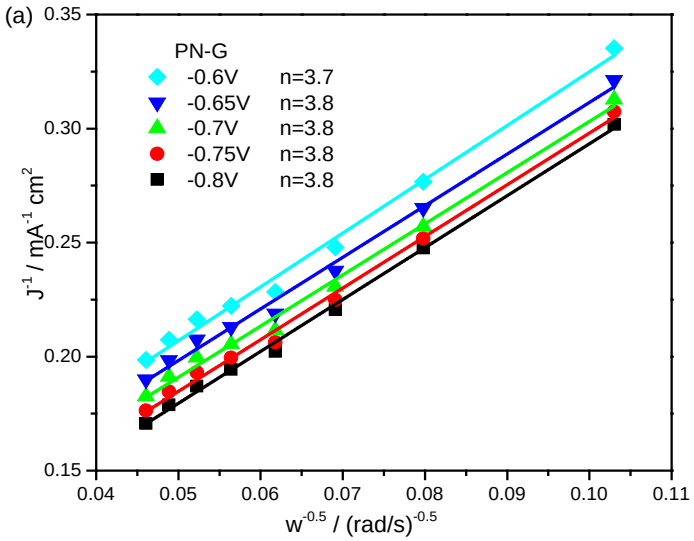

Figure 4.7 Koutecky-Levich Plots for PN-BG samples at different potentials. (a) PN-G-GCE, (b) PN-B_1G-GCE, (c) PN-B_2G –GCE, (d) PN-B_3G –GCE. (Continued)

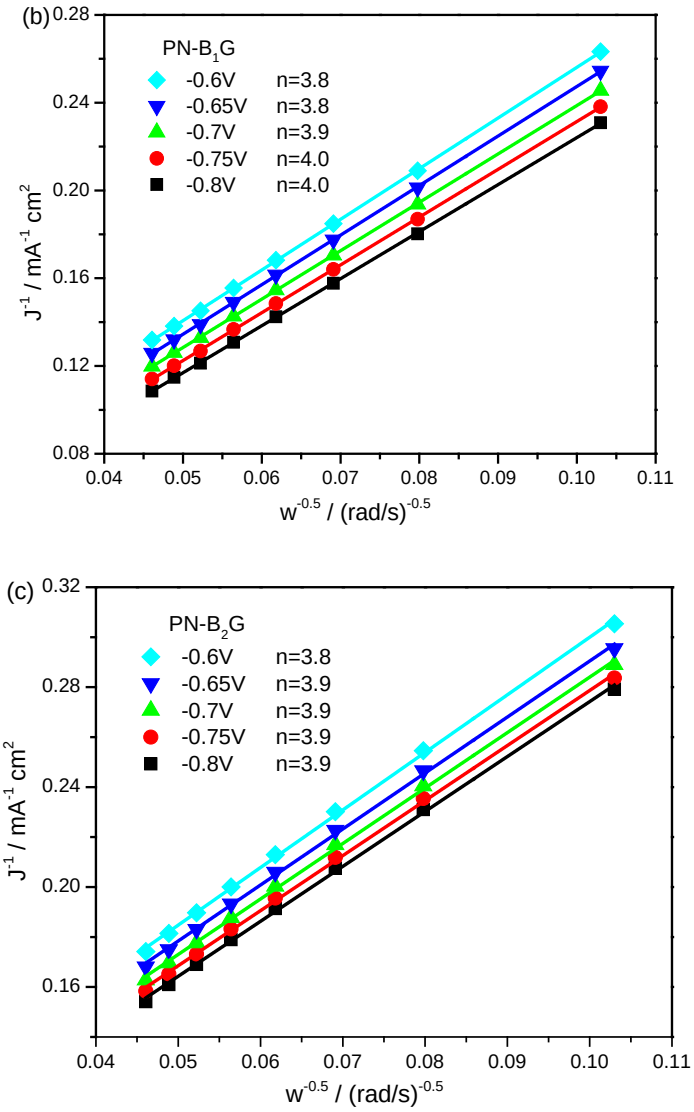

Figure 4.7 Koutecky-Levich Plots for PN-BG samples at different potentials. (a) PN-G-GCE, (b) PN-B_1G-GCE, (c) PN-B_2G –GCE, (d) PN-B_3G –GCE. (Continued)

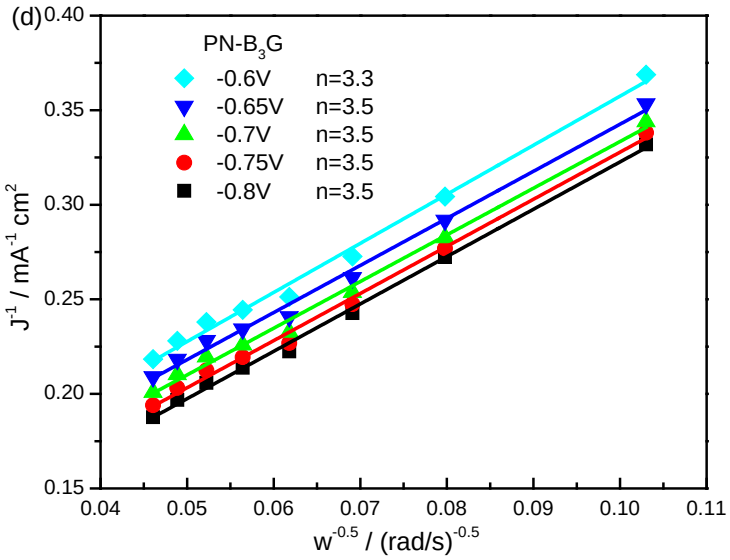

Figure 4.7 (Continued) Koutecky-Levich Plots for PN-BG samples at different potentials. (a) PN-G-GCE, (b) PN-B_1G-GCE, (c) PN-B_2G –GCE, (d) PN-B_3G –GCE.

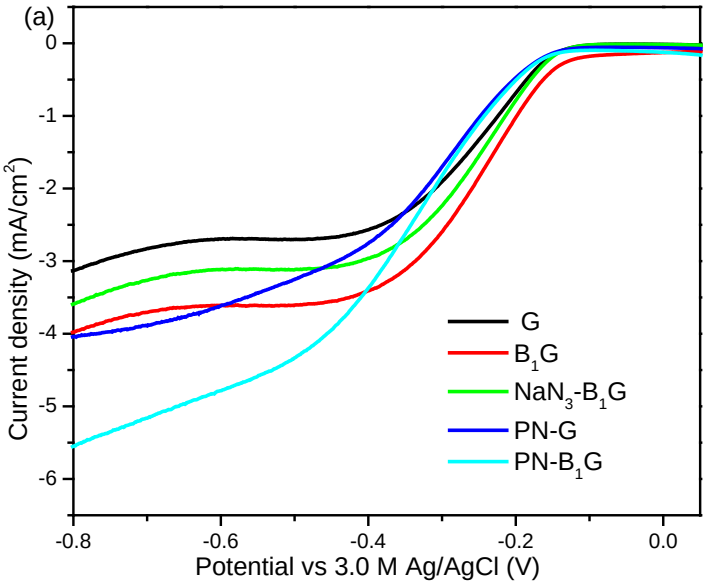

Figure 4.8 LSV curves of ORR on G-GCE, B_1G-GCE, NaN_3-B_1G-GCE, PN-G-GCE, and PN-B_1G-GCE electrode in an Oxygen-saturated 0.1 M KOH solution with a rotation speed of 1500 rpm (scan rate: 5 mV/s);

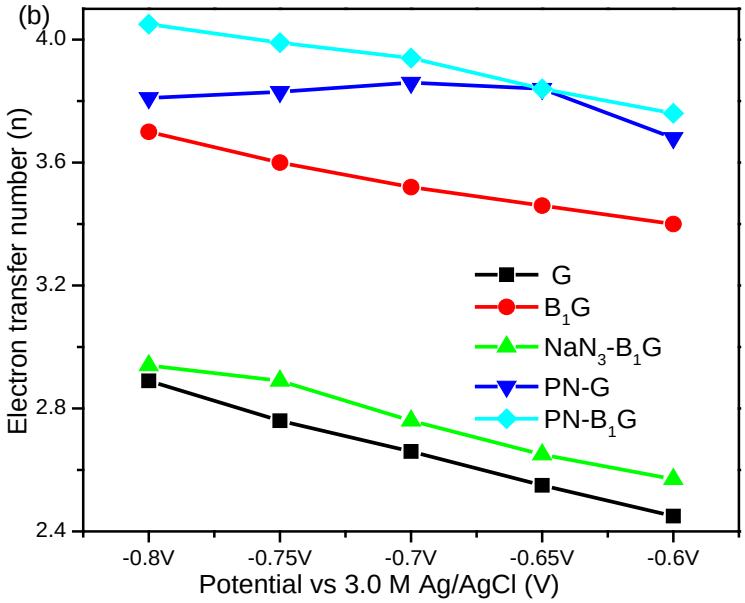

Figure 4.9 Electron transfer number n of G-GCE, B_1G-GCE, NaN_3-B_1G-GCE, PN-G-GCE, and PN-B_1G-GCE calculated from Koutecky-Levich equation.

4.4 Summary

In this section, polynitrogen N_8^- (PN) deposited on boron-doped graphene (PN-BG) and graphene (PN-G) was synthesized experimentally by cyclic voltammetry (CV) method under ambient condition. Boron-doped graphene (BG) were prepared by a facile hydrothermal method with the mixture of graphene oxide and $NaBH_4$. Compared to the graphene matrix, a larger amount of N_8^- was prepared on B_1G matrix. It was attributed to the boron doping, which enhanced the charge transfer ability from BG to PN chain resulting into producing more PN on BG. PN-BG and PN-G were further used as electrode catalysts for ORR, while the optimal former one (B_1G) showed the highest activity. It was ascribed to the larger amount of N_8^- observed on B_1G, which provided more active sites for ORR. Kinetic study revealed that it was through a one-step four-electron process over N_8^-.

This work provides a facile strategy to modify graphene structure and efficiently stabilizes PN for fuel cell applications.

CHAPTER 5

CONCLUSIONS AND PERSPECTIVES

5.1 Conclusions

PN supported on different carbon material substrates were synthesized with CV method under ambient conditions and further used as cathode catalysts for ORR in alkaline solution. Major conclusions and achievements from the results of this work are:

1. UV irradiation can be a convenient strategy to promote the synthesis of N_8^- on MWNT. Optimization of the UV energy and the power of the UV lamp for the synthesis may lead to even a larger amount of N_8^- synthesized and better ORR performance.

2. Although it has a more negative onset potential, the current density of PN-MWNT-254nm can be higher than a commercial Pt/C electrode at high potential (-0.8V).

3. The activity of PN catalysts toward ORR can be attributed to the lone pair electrons of nitrogen from N_8^-. A larger amount of PN provided more active sites for ORR in alkaline solution, which led to increased ORR activity.

4. Kinetic study revealed that it was through a one-step four-electron process on N_8^- while the O_2 reduction catalyzed at the N_3^- was a two-electron reduction process in 0.1M KOH.

5. For the first time, ORR mechanism of PN catalyst was systematically investigated by the combination of kinetic study, NBO analysis and *in situ* spectroscopy characterization (SHINERS). The most active sites of N_8^- were N1 and N2 locating in the center of the chain with adjacent position that have more negative charges, which facilitated the four-electron pathway by weakening the O-O bonding with side-on adsorption.

6. Graphene (G), boron-doped graphene (BG) and nitrogen-doped graphene (NG) were prepared by a facile hydrothermal method as catalyst substrates, and polynitrogen (N_8^-) deposited on aforementioned graphene based substrates were successfully synthesized by cyclic voltammetry (CV) approach for the first time. The resulting PN-NG and PN-BG catalysts possess good electrocatalytic activity towards ORR in 0.1M KOH.

7. The incorporation of nitrogen, boron dopants into the graphene matrix could create positive charged sites and lead to more facile electron transfer, which effectively stabilized negative N_8^- chain. Heteroatom-doped carbon nanomaterials can be used as ideal substrates for promoting PN catalysts synthesis. An appropriate amount of dopant is necessary for the enhancement of PN synthesis, but an excess of dopant brings large defect densities, poor conductivity and low surface area in microstructure that will have adverse effects.

5.2 Perspectives

Although the novel PN (N_8^-) catalyst is highly active for ORR, further improvement of the ORR activity and stability are required for its practical application. Several tasks for the future research are summarized below.

1. Further understanding the PN synthesis reaction route, and find the key point affecting the N_8^- amount produced. Such work can provide a scientific basis for designing and optimizing PN-series catalysts for ORR. Since the electrochemical synthesis is complicated and rapid process, it is difficult to detect the intermediates experimentally. Theoretical calculation could be carried out to clarify the reaction route of N_3^- to N_8^-.

2. Exploring new facile strategy to precisely control dopant content and doping forms (particularly for nitrogen doped graphene), developing co-doped graphene, and extending surface area of doped graphene, which are favored for PN synthesis.

3. The performance of these PN-series catalysts towards ORR is still not as good as that of the commercial Pt/C in terms of the onset potential. The optimization of PN catalyst is of great importance to minimize the overpotential.

4. The long-term operation stability, the tolerance to possible crossover effect and poisoning are critical criterions to evaluate the quality of the electrocatalysts, which need to be further tested for real application.

5. Up to now, the excellent electrocatalytic performance for ORR is mainly achieved in alkaline media for the PN-series catalysts, PN-series catalysts for ORR in acidic media covering the catalytic activity and reaction mechanisms are suggested in future work.

6. In current research, PN-series catalysts for ORR were tested in half-cell reaction. To enable the practical applications of PN-series catalysts, full-cell test experiment would be more appropriate and should be seriously considered in future.

7. Using ORR as a probe reaction, more electrocatalysis processes such as oxygen evolution and hydrogen evolution reactions may be concerned.

REFERENCES

[1] G. Centi, E.A. Quadrelli, S. Perathoner, Catalysis for CO_2 conversion: A key technology for rapid introduction of renewable energy in the value chain of chemical industries[J]. Energy and Environmental Science, 2013, 6 (6): 1711-1731.

[2] B.C. McLellan, G.D. Corder, D.P. Giurco, K.N. Ishihara, Renewable energy in the minerals industry: A review of global potential[J]. Journal of Cleaner Production, 2012, 32 32-44.

[3] R. Borup, J. Meyers, B. Pivovar, Y.S. Kim, R. Mukundan, N. Garland, D. Myers, M. Wilson, F. Garzon, D. Wood, P. Zelenay, K. More, K. Stroh, T. Zawodzinski, J. Boncella, J.E. McGrath, M. Inaba, K. Miyatake, M. Hori, K. Ota, Z. Ogumi, S. Miyata, A. Nishikata, Z. Siroma, Y. Uchimoto, K. Yasuda, K.I. Kimijima, N. Iwashita, Scientific aspects of polymer electrolyte fuel cell durability and degradation[J]. Chemical Reviews, 2007, 107 (10): 3904-3951.

[4] J. Stacy, Y.N. Regmi, B. Leonard, M. Fan, The recent progress and future of oxygen reduction reaction catalysis: A review[J]. Renewable and Sustainable Energy Reviews, 2017, 69 401-414.

[5] H. Lv, D. Li, D. Strmcnik, A.P. Paulikas, N.M. Markovic, V.R. Stamenkovic, Recent advances in the design of tailored nanomaterials for efficient oxygen reduction reaction[J]. Nano Energy, 2016, 29 149-165.

[6] V. Di Noto, E. Negro, K. Vezzù, L. Toniolo, G. Pace, Interplay between structural and electrochemical properties of Pt-Rh carbon nitride electrocatalysts for the oxygen reduction reaction[J]. Electrochimica Acta, 2011, 57 257-269.

[7] J. Greeley, I.E.L. Stephens, A.S. Bondarenko, T.P. Johansson, H.A. Hansen, T.F. Jaramillo, J. Rossmeisl, I. Chorkendorff, J.K. Nørskov, Alloys of platinum and early transition metals as oxygen reduction electrocatalysts[J]. Nature Chemistry, 2009, 1 (7): 552-556.

[8] X. Yu, S. Ye, Recent advances in activity and durability enhancement of Pt/C catalytic cathode in PEMFC: Part II: Degradation mechanism and durability enhancement of carbon supported platinum catalyst[J]. Journal of Power Sources, 2007, 172 (1): 145-154.

[9] M. Winter, R.J. Brodd, What are batteries, fuel cells, and supercapacitors?[J]. Chemical Reviews, 2004, 104 (10): 4245-4270.

[10] B. Wang, Recent development of non-platinum catalysts for oxygen reduction reaction[J]. Journal of Power Sources, 2005, 152 1-15.

[11] M. Shao, Q. Chang, J.-P. Dodelet, R. Chenitz, Recent advances in electrocatalysts for oxygen reduction reaction[J]. Chemical Reviews, 2016, 116 (6): 3594-3657.

[12] K. Gong, F. Du, Z. Xia, M. Durstock, L. Dai, Nitrogen-doped carbon nanotube arrays with high electrocatalytic activity for oxygen reduction[J]. Science, 2009, 323 (5915): 760-764.

[13] T. Sharifi, G. Hu, X. Jia, T. Wågberg, Formation of active sites for oxygen reduction reactions by transformation of nitrogen functionalities in nitrogen-doped carbon nanotubes[J]. ACS Nano, 2012, 6 (10): 8904-8912.

[14] L. Qu, Y. Liu, J.B. Baek, L. Dai, Nitrogen-doped graphene as efficient metal-free electrocatalyst for oxygen reduction in fuel cells[J]. ACS Nano, 2010, 4 (3): 1321-1326.

[15] Q. Wei, X. Tong, G. Zhang, J. Qiao, Q. Gong, S. Sun, Nitrogen-doped carbon nanotube and graphene materials for oxygen reduction reactions[J]. Catalysts, 2015, 5 (3): 1574-1602.

[16] L. Lai, J.R. Potts, D. Zhan, L. Wang, C.K. Poh, C. Tang, H. Gong, Z. Shen, J. Lin, R.S. Ruoff, Exploration of the active center structure of nitrogen-doped graphene-based catalysts for oxygen reduction reaction[J]. Energy and Environmental Science, 2012, 5 (7): 7936-7942.

[17] X. Wang, J.S. Lee, Q. Zhu, J. Liu, Y. Wang, S. Dai, Ammonia-treated ordered mesoporous carbons as catalytic materials for oxygen reduction reaction[J]. Chemistry of Materials, 2010, 22 (7): 2178-2180.

[18] J. Lu, X. Bo, H. Wang, L. Guo, Nitrogen-doped ordered mesoporous carbons synthesized from honey as metal-free catalyst for oxygen reduction reaction[J]. Electrochimica Acta, 2013, 108 10-16.

[19] L.F. Chen, X.D. Zhang, H.W. Liang, M. Kong, Q.F. Guan, P. Chen, Z.Y. Wu, S.H. Yu, Synthesis of nitrogen-doped porous carbon nanofibers as an efficient electrode material for supercapacitors[J]. ACS Nano, 2012, 6 (8): 7092-7102.

[20] S. Wang, C. Dai, J. Li, L. Zhao, Z. Ren, Y. Ren, Y. Qiu, J. Yu, The effect of different nitrogen sources on the electrocatalytic properties of nitrogen-doped electrospun carbon nanofibers for the oxygen reduction reaction[J]. International Journal of Hydrogen Energy, 2015, 40 (13): 4673-4682.

[21] M. Yang, D. Yang, H. Chen, Y. Gao, H. Li, Nitrogen-doped carbon nanotubes as catalysts for the oxygen reduction reaction in alkaline medium[J]. Journal of Power Sources, 2015, 279 28-35.

[22] L. Zhang, Z. Xia, Mechanisms of oxygen reduction reaction on nitrogen-doped graphene for fuel cells[J]. The Journal of Physical Chemistry C 2011, 115(22): 11170-11176.

[23] K. Selvakumar, S.M. Senthil Kumar, R. Thangamuthu, K. Ganesan, P. Murugan, P. Rajput, S.N. Jha, D. Bhattacharyya, Physiochemical investigation of shape-designed MnO_2 nanostructures and their influence on oxygen reduction reaction activity in alkaline solution[J]. The Journal of Physical Chemistry C, 2015, 119 (12): 6604-6618.

[24] T.C. Nagaiah, S. Kundu, M. Bron, M. Muhler, W. Schuhmann, Nitrogen-doped carbon nanotubes as a cathode catalyst for the oxygen reduction reaction in alkaline medium[J]. Electrochemistry Communications, 2010, 12 (3): 338-341.

[25] Y. Tang, B.L. Allen, D.R. Kauffman, A. Star, Electrocatalytic activity of nitrogen-doped carbon nanotube cups[J]. Journal of the American Chemical Society, 2009, 131 (37): 13200-13201.

[26] Z. Chen, D. Higgins, Z. Chen, Nitrogen doped carbon nanotubes and their impact on the oxygen reduction reaction in fuel cells[J]. Carbon, 2010, 48 (11): 3057-3065.

[27] J. Wu, W. Pisula, K. Müllen, Graphenes as potential material for electronics[J]. Chemical Reviews, 2007, 107 (3): 718-747.

[28] Y. Zhang, J. Ge, L. Wang, D. Wang, F. Ding, X. Tao, W. Chen, Manageable N-doped graphene for high performance oxygen reduction reaction[J]. Scientific Reports, 2013, 3

[29] Y. Shao, S. Zhang, M.H. Engelhard, G. Li, G. Shao, Y. Wang, J. Liu, I.A. Aksay, Y. Lin, Nitrogen-doped graphene and its electrochemical applications[J]. Journal of Materials Chemistry, 2010, 20 (35): 7491-7496.

[30] M. Park, T. Lee, B.S. Kim, Covalent functionalization based heteroatom doped graphene nanosheet as a metal-free electrocatalyst for oxygen reduction reaction[J]. Nanoscale, 2013, 5 (24): 12255-12260.

[31] S. Yasuda, L. Yu, J. Kim, K. Murakoshi, Selective nitrogen doping in graphene for oxygen reduction reactions[J]. Chemical Communications, 2013, 49 (83): 9627-9629.

[32] T. Xing, Y. Zheng, L.H. Li, B.C.C. Cowie, D. Gunzelmann, S.Z. Qiao, S. Huang, Y. Chen, Observation of active sites for oxygen reduction reaction on nitrogen-doped multilayer graphene[J]. ACS Nano, 2014, 8 (7): 6856-6862.

[33] D. Yu, L. Wei, W. Jiang, H. Wang, B. Sun, Q. Zhang, K. Goh, R. Si, Y. Chen, Nitrogen doped holey graphene as an efficient metal-free multifunctional electrochemical catalyst for hydrazine oxidation and oxygen reduction[J]. Nanoscale, 2013, 5 (8): 3457-3464.

[34] Z. Lin, M.-k. Song, Y. Ding, Y. Liu, M. Liu, C.-p. Wong, Facile preparation of nitrogen-doped graphene as a metal-free catalyst for oxygen reduction reaction[J]. Physical Chemistry Chemical Physics, 2012, 14 (10): 3381-3387.

[35] S.M. Unni, S. Devulapally, N. Karjule, S. Kurungot, Graphene enriched with pyrrolic coordination of the doped nitrogen as an efficient metal-free electrocatalyst for oxygen reduction[J]. Journal of Materials Chemistry, 2012, 22 (44): 23506-23513.

[36] Z. Lin, G.H. Waller, Y. Liu, M. Liu, C.-p. Wong, Simple preparation of nanoporous few-layer nitrogen-doped graphene for use as an efficient electrocatalyst for oxygen reduction and oxygen evolution reactions[J]. Carbon, 2013, 53 130-136.

[37] H.-P. Cong, P. Wang, M. Gong, S.-H. Yu, Facile synthesis of mesoporous nitrogen-doped graphene: An efficient methanol-tolerant cathodic catalyst for oxygen reduction reaction[J]. Nano Energy, 2014, 3 55-63.

[38] Z. Wang, B. Li, Y. Xin, J. Liu, Y. Yao, Z. Zou, Rapid synthesis of nitrogen-doped graphene by microwave heating for oxygen reduction reactions in alkaline electrolyte[J]. Chinese Journal of Catalysis, 2014, 35 (4): 509-513.

[39] J. Wu, L. Ma, R.M. Yadav, Y. Yang, X. Zhang, R. Vajtai, J. Lou, P.M. Ajayan, Nitrogen-doped graphene with pyridinic dominance as a highly active and stable electrocatalyst for oxygen reduction[J]. ACS Applied Materials and Interfaces, 2015, 7 (27): 14763-14769.

[40] N.P. Subramanian, X. Li, V. Nallathambi, S.P. Kumaraguru, H. Colon-Mercado, G. Wu, J.W. Lee, B.N. Popov, Nitrogen-modified carbon-based catalysts for oxygen reduction reaction in polymer electrolyte membrane fuel cells[J]. Journal of Power Sources, 2009, 188 (1): 38-44.

[41] H. Wang, T. Maiyalagan, X. Wang, Review on recent progress in nitrogen-doped graphene: synthesis, characterization, and its potential applications[J]. ACS Catalysis, 2012, 2 (5): 781-794.

[42] M. Hu, Z. Yao, X. Wang, Characterization techniques for graphene-based materials in catalysis[J]. AIMS Materials Science, 2017, 4 (3): 755-788.

[43] H. Kim, K. Lee, S.I. Woo, Y. Jung, On the mechanism of enhanced oxygen reduction reaction in nitrogen-doped graphene nanoribbons[J]. Physical Chemistry Chemical Physics, 2011, 13 (39): 17505-17510.

[44] R. Liu, D. Wu, X. Feng, K. Müllen, Nitrogen-doped ordered mesoporous graphitic arrays with high electrocatalytic activity for oxygen reduction[J]. Angewandte Chemie - International Edition, 2010, 49 (14): 2565-2569.

[45] Z. Yang, H. Nie, X.a. Chen, X. Chen, S. Huang, Recent progress in doped carbon nanomaterials as effective cathode catalysts for fuel cell oxygen reduction reaction[J]. Journal of Power Sources, 2013, 236 238-249.

[46] L. Dai, Y. Xue, L. Qu, H.-J. Choi, J.-B. Baek, Metal-free catalysts for oxygen reduction reaction[J]. Chemical Reviews, 2015, 115 (11): 4823-4892.

[47] D. Deng, X. Pan, L. Yu, Y. Cui, Y. Jiang, J. Qi, W.-X. Li, Q. Fu, X. Ma, Q. Xue, G. Sun, X. Bao, Toward N-doped graphene via solvothermal synthesis[J]. Chemistry of Materials, 2011, 23 (5): 1188-1193.

[48] A. Zhao, J. Masa, W. Schuhmann, W. Xia, Activation and stabilization of nitrogen-doped carbon nanotubes as electrocatalysts in the oxygen reduction reaction at strongly alkaline conditions[J]. Journal of Physical Chemistry C, 2013, 117 (46): 24283-24291.

[49] Y. Cheng, Y. Tian, X. Fan, J. Liu, C. Yan, Boron doped multi-walled carbon nanotubes as catalysts for oxygen reduction reaction and oxygen evolution reactionin in alkaline media[J]. Electrochimica Acta, 2014, 143 291-296.

[50] G. Fazio, L. Ferrighi, C. Di Valentin, Boron-doped graphene as active electrocatalyst for oxygen reduction reaction at a fuel-cell cathode[J]. Journal of Catalysis, 2014, 318 203-210.

[51] X. Bo, L. Guo, Ordered mesoporous boron-doped carbons as metal-free electrocatalysts for the oxygen reduction reaction in alkaline solution[J]. Physical Chemistry Chemical Physics, 2013, 15 (7): 2459-2465.

[52] Z.H. Sheng, H.L. Gao, W.J. Bao, F.B. Wang, X.H. Xia, Synthesis of boron doped graphene for oxygen reduction reaction in fuel cells[J]. Journal of Materials Chemistry, 2012, 22 (2): 390-395.

[53] L. Yang, S. Jiang, Y. Zhao, L. Zhu, S. Chen, X. Wang, Q. Wu, J. Ma, Y. Ma, Z. Hu, Boron-doped carbon nanotubes as metal-free electrocatalysts for the oxygen reduction reaction[J]. Angewandte Chemie - International Edition, 2011, 50 (31): 7132-7135.

[54] Z.W. Liu, F. Peng, H.J. Wang, H. Yu, W.X. Zheng, J. Yang, Phosphorus-doped graphite layers with high electrocatalytic activity for the O_2 reduction in an alkaline medium[J]. Angewandte Chemie - International Edition, 2011, 50 (14): 3257-3261.

[55] Z. Liu, F. Peng, H. Wang, H. Yu, W. Zheng, X. Wei, Preparation of phosphorus-doped carbon nanospheres and their electrocatalytic performance for O_2 reduction[J]. Journal of Natural Gas Chemistry, 2012, 21 (3): 257-264.

[56] Z. Liu, F. Peng, H. Wang, H. Yu, J. Tan, L. Zhu, Novel phosphorus-doped multiwalled nanotubes with high electrocatalytic activity for O_2 reduction in alkaline medium[J]. Catalysis Communications, 2011, 16 (1): 35-38.

[57] W. He, Y. Wang, C. Jiang, L. Lu, Structural effects of a carbon matrix in non-precious metal O2-reduction electrocatalysts[J]. Chemical Society Reviews, 2016, 45 (9): 2396-2409.

[58] Z. Yang, Z. Yao, G. Li, G. Fang, H. Nie, Z. Liu, X. Zhou, X.a. Chen, S. Huang, Sulfur-doped graphene as an efficient metal-free cathode catalyst for oxygen reduction[J]. ACS Nano, 2012, 6 (1): 205-211.

[59] J.-i. Ozaki, N. Kimura, T. Anahara, A. Oya, Preparation and oxygen reduction activity of BN-doped carbons[J]. Carbon, 2007, 45 (9): 1847-1853.

[60] S. Wang, E. Iyyamperumal, A. Roy, Y. Xue, D. Yu, L. Dai, Vertically aligned BCN nanotubes as efficient metal-free electrocatalysts for the oxygen reduction reaction: A synergetic effect by co-doping with boron and nitrogen[J]. Angewandte Chemie - International Edition, 2011, 50 (49): 11756-11760.

[61] Y. Zhao, L. Yang, S. Chen, X. Wang, Y. Ma, Q. Wu, Y. Jiang, W. Qian, Z. Hu, Can boron and nitrogen Co-doping improve oxygen reduction reaction activity of carbon nanotubes?[J]. Journal of the American Chemical Society, 2013, 135 (4): 1201-1204.

[62] C. You, S. Liao, H. Li, S. Hou, H. Peng, X. Zeng, F. Liu, R. Zheng, Z. Fu, Y. Li, Uniform nitrogen and sulfur co-doped carbon nanospheres as catalysts for the oxygen reduction reaction[J]. Carbon, 2014, 69 294-301.

[63] Y. Su, Y. Zhang, X. Zhuang, S. Li, D. Wu, F. Zhang, X. Feng, Low-temperature synthesis of nitrogen/sulfur co-doped three-dimensional graphene frameworks as efficient metal-free electrocatalyst for oxygen reduction reaction[J]. Carbon, 2013, 62 296-301.

[64] C.H. Choi, S.H. Park, S.I. Woo, Heteroatom doped carbons prepared by the pyrolysis of bio-derived amino acids as highly active catalysts for oxygen electro-reduction reactions[J]. Green Chemistry, 2011, 13 (2): 406-412.

[65] J. Liu, P. Song, Z. Ning, W. Xu, Recent advances in heteroatom-doped metal-free electrocatalysts for highly efficient oxygen reduction reaction[J]. Electrocatalysis, 2015, 6 (2): 132-147.

[66] S. Dou, A. Shen, Z. Ma, J. Wu, L. Tao, S. Wang, N-, P- and S-tridoped graphene as metal-free electrocatalyst for oxygen reduction reaction[J]. Journal of Electroanalytical Chemistry, 2015, 753 21-27.

[67] S. Bag, B. Mondal, A.K. Das, C.R. Raj, Nitrogen and sulfur dual-doped reduced graphene oxide: synergistic effect of dopants towards oxygen reduction reaction[J]. Electrochimica Acta, 2015, 163 16-23.

[68] C. You, X. Jiang, X. Wang, Y. Hua, C. Wang, Q. Lin, S. Liao, Nitrogen, sulfur Co-doped carbon derived from naphthalene-based covalent organic framework as an efficient catalyst for oxygen reduction[J]. ACS Applied Energy Materials, 2018, 1 (1): 161-166.

[69] C. Yang, H. Jin, C. Cui, J. Li, J. Wang, K. Amine, J. Lu, S. Wang, Nitrogen and sulfur co-doped porous carbon sheets for energy storage and pH-universal oxygen reduction reaction[J]. Nano Energy, 2018, 54 192-199.

[70] R. Li, Z. Wei, X. Gou, Nitrogen and phosphorus dual-doped graphene/carbon nanosheets as bifunctional electrocatalysts for oxygen reduction and evolution[J]. ACS Catalysis, 2015, 5 (7): 4133-4142.

[71] K. Lv, H. Zhang, S. Chen, Nitrogen and phosphorus co-doped carbon modified activated carbon as an efficient oxygen reduction catalyst for microbial fuel cells[J]. RSC Advances, 2018, 8 (2): 848-855.

[72] L. Wang, Z. Sofer, R. Zboril, K. Cepe, M. Pumera, Phosphorus and halogen co-doped graphene materials and their electrochemistry[J]. Chemistry - A European Journal, 2016, 22 (43): 15444-15450.

[73] H. Abou-Rachid, A. Hu, V. Timoshevskii, Y. Song, L.S. Lussier, Nanoscale high energetic materials: A polymeric nitrogen chain N_8 confined inside a carbon nanotube[J]. Physical Review Letters, 2008, 100 (19):

[74] B. Hirshberg, R.B. Gerber, A.I. Krylov, Calculations predict a stable molecular crystal of N_8[J]. Nat. Chem., 2014, 6 (1): 52-56.

[75] Z. Wu, E.M. Benchafia, Z. Iqbal, X. Wang, N_8^- polynitrogen stabilized on multi-wall carbon nanotubes for oxygen-reduction reactions at ambient conditions[J]. Angewandte Chemie - International Edition, 2014, 53 (46): 12555-12559.

[76] F. Barat, B. Hickel, J. Sutton, Flash photolysis of aqueous solutions of azide and nitrate ions[J]. Journal of the Chemical Society D: Chemical Communications, 1969, (3): 125b-126.

[77] A. Treinin, E. Hayon, Spectroscopic observation of the azide radical in solution[J]. The Journal of Chemical Physics, 1969, 50 (1): 549-550.

[78] E. Hayon, M. Simic, Absorption spectra and kinetics of the intermediate produced from the decay of azide radicals[J]. Journal of the American Chemical Society, 1970, 92 (25): 7486-7487.

[79] S.M. Peiris, T.P. Russell, Photolysis of compressed sodium azide (NaN_3) as a synthetic pathway to nitrogen materials[J]. Journal of Physical Chemistry A, 2003, 107 (6): 944-947.

[80] B.A. Thrush, The Detection of free radicals in the high intensity photolysis of hydrogen azide[J]. Proceedings of the Royal Society of London A: Mathematical, Physical and Engineering Sciences, 1956, 235 (1200): 143-147.

[81] N. Hansen, A.M. Wodtke, Velocity map ion imaging of chlorine azide photolysis: Evidence for photolytic production of cyclic-N_3[J]. Journal of Physical Chemistry A, 2003, 107 (49): 10608-10614.

[82] S.L. Chou, J.I. Lo, M.Y. Lin, Y.C. Peng, H.C. Lu, B.M. Cheng, Production of N3 upon photolysis of solid nitrogen at 3 K with synchrotron radiation[J]. Angewandte Chemie - International Edition, 2014, 53 (3): 738-741.

[83] I. Burak, A. Treinin, Spectrum of N_3^- in solution[J]. The Journal of Chemical Physics, 1963, 39 (1): 189-196.

[84] W.D. Closson, H.B. Gray, [ILL] [ILL] [ILL] and spectra of the azide ion and alkyl azides[J]. Journal of the American Chemical Society, 1963, 85 (3): 290-294.

[85] J.R. McDonald, J.W. Rabalais, S.P. McGlynn, Electronic spectra of the azide ion, hydrazoic acid, and azido molecules[J]. The Journal of Chemical Physics, 1970, 52 (3): 1332-1340.

[86] I. Burak, A. Treinin, The photochemistry of N_3^- in aqueous solution at 254 mμ[J]. Journal of the American Chemical Society, 1965, 87 (18): 4031-4036.

[87] M.H. Thiemens, T. Jackson, Production of isotopically heavy ozone by ultraviolet light photolysis of O2[J]. Geophysical Research Letters, 1987, 14 (6): 624-627.

[88] W. Han, W. Zhu, P. Zhang, Y. Zhang, L. Li, Photocatalytic degradation of phenols in aqueous solution under irradiation of 254 and 185 nm UV light[J]. Catalysis Today, 2004, 90 (3-4): 319-324.

[89] H. Jin, H. Huang, Y. He, X. Feng, S. Wang, L. Dai, J. Wang, Graphene quantum dots supported by graphene nanoribbons with ultrahigh electrocatalytic performance for oxygen reduction[J]. Journal of the American Chemical Society, 2015, 137 (24): 7588-7591.

[90] S. Wang, D. Yu, L. Dai, Polyelectrolyte functionalized carbon nanotubes as efficient metal-free electrocatalysts for oxygen reduction[J]. Journal of the American Chemical Society, 2011, 133 (14): 5182-5185.

[91] R. Silva, D. Voiry, M. Chhowalla, T. Asefa, Efficient metal-free electrocatalysts for oxygen reduction: polyaniline-derived N- and O-doped mesoporous carbons[J]. Journal of the American Chemical Society, 2013, 135 (21): 7823-7826.

[92] A. Holewinski, J.-C. Idrobo, S. Linic, High-performance Ag-Co alloy catalysts for electrochemical oxygen reduction[J]. Nature Chemistry, 2014, 6 (9): 828-834.

[93] Y. Li, Y. Zhao, H. Cheng, Y. Hu, G. Shi, L. Dai, L. Qu, Nitrogen-doped graphene quantum dots with oxygen-rich functional groups[J]. Journal of the American Chemical Society, 2012, 134 (1): 15-18.

[94] C.-Y. Li, J.-C. Dong, X. Jin, S. Chen, R. Panneerselvam, A.V. Rudnev, Z.-L. Yang, J.-F. Li, T. Wandlowski, Z.-Q. Tian, *In situ* monitoring of electrooxidation processes at gold single crystal surfaces using shell-isolated nanoparticle-enhanced Raman spectroscopy[J]. Journal of the American Chemical Society, 2015, 137 (24): 7648-7651.

[95] T.A. Galloway, L.J. Hardwick, Utilizing *in situ* electrochemical SHINERS for oxygen reduction reaction studies in aprotic electrolytes[J]. The Journal of Physical Chemistry Letters, 2016, 7 (11): 2119-2124.

[96] Y.F. Huang, P.J. Kooyman, M.T. Koper, Intermediate stages of electrochemical oxidation of single-crystalline platinum revealed by *in situ* Raman spectroscopy[J]. Nature communications, 2016, 7 12440.

[97] W.-L. Dai, Y. Dong, Y. Cao, J.-F. Deng, K.-N. Fan, Y.-Y. Liao, B.-F. Hong, *In situ* Raman studies on the interaction of oxygen and methanol with an iodine-modified electrolytic silver catalyst[J]. Journal of Raman Spectroscopy, 2002, 33 (5): 318-324.

[98] R. Chen, H. Li, D. Chu, G. Wang, Unraveling oxygen reduction reaction mechanisms on carbon-supported fe-phthalocyanine and co-phthalocyanine catalysts in alkaline solutions[J]. Journal of Physical Chemistry C, 2009, 113 (48): 20689-20697.

[99] E.D. Stevens, H. Hope, A study of the electron‐density distribution in sodium azide, NaN_3[J]. Acta Crystallographica Section A, 1977, 33 (5): 723-729.

[100] X. Wang, J. Li, H. Zhu, L. Chen, H. Lin, Polymerization of nitrogen in cesium azide under modest pressure[J]. Journal of Chemical Physics, 2014, 141 (4):

[101] V. Timoshevskii, W. Ji, H. Abou-Rachid, L.S. Lussier, H. Guo, Polymeric nitrogen in a graphene matrix: An ab initio study[J]. Physical Review B - Condensed Matter and Materials Physics, 2009, 80 (11):

[102] X. Shi, B. Liu, S. Liu, S. Niu, S. Liu, R. Liu, B. Liu, Polymeric nitrogen A7 layers stabilized in the confinement of a multilayer BN matrix at ambient conditions[J]. Scientific reports, 2018, 8 (1): 13758-13758.

[103] S. Niu, S. Liu, B. Liu, X. Shi, S. Liu, R. Liu, M. Yao, T. Cui, B. Liu, High energetic polymeric nitrogen sheet confined in a graphene matrix[J]. RSC Advances, 2018, 8 (54): 30912-30918.

[104] S. Liu, M. Yao, F. Ma, B. Liu, Z. Yao, R. Liu, T. Cui, B. Liu, High energetic polymeric nitrogen stabilized in the confinement of boron nitride nanotube at ambient conditions[J]. The Journal of Physical Chemistry C, 2016, 120 (30): 16412-16417.

[105] A.K. Geim, K.S. Novoselov, The rise of graphene[J]. Nature Materials, 2007, 6 (3): 183-191.

[106] D. Chen, L. Tang, J. Li, Graphene-based materials in electrochemistry[J]. Chemical Society Reviews, 2010, 39 (8): 3157-3180.

[107] B. Seger, P.V. Kamat, Electrocatalytically active graphene-platinum nanocomposites. Role of 2-D carbon support in PEM fuel cells[J]. The Journal of Physical Chemistry C, 2009, 113 (19): 7990-7995.

[108] M. Hu, K.S. Hui, K.N. Hui, Role of graphene in MnO_2/graphene composite for catalytic ozonation of gaseous toluene[J]. Chemical Engineering Journal, 2014, 254 237-244.

[109] D. Geng, Y. Hu, Y. Li, R. Li, X. Sun, One-pot solvothermal synthesis of doped graphene with the designed nitrogen type used as a Pt support for fuel cells[J]. Electrochemistry Communications, 2012, 22 65-68.

[110] Y. Sun, C. Du, G. Han, Y. Qu, L. Du, Y. Wang, G. Chen, Y. Gao, G. Yin, Boron, nitrogen co-doped graphene: a superior electrocatalyst support and enhancing mechanism for methanol electrooxidation[J]. Electrochimica Acta, 2016, 212 313-321.

[111] X. Bo, M. Li, C. Han, L. Guo, The influence of boron dopant on the electrochemical properties of graphene as an electrode material and a support for Pt catalysts[J]. Electrochimica Acta, 2013, 114 582-589.

[112] Y. Sun, C. Du, M. An, L. Du, Q. Tan, C. Liu, Y. Gao, G. Yin, Boron-doped graphene as promising support for platinum catalyst with superior activity towards the methanol electrooxidation reaction[J]. Journal of Power Sources, 2015, 300 245-253.

[113] T. Varga, G. Ballai, L. Vásárhelyi, H. Haspel, Á. Kukovecz, Z. Kónya, Co_4N/nitrogen-doped graphene: A non-noble metal oxygen reduction electrocatalyst for alkaline fuel cells[J]. Applied Catalysis B: Environmental, 2018, 237 826-834.

[114] Y. Xu, Y. Mo, J. Tian, P. Wang, H. Yu, J. Yu, The synergistic effect of graphitic N and pyrrolic N for the enhanced photocatalytic performance of nitrogen-doped graphene/TiO_2 nanocomposites[J]. Applied Catalysis B: Environmental, 2016, 181 810-817.

[115] M. Hu, Z. Yao, X. Wang, Graphene-based nanomaterials for catalysis[J]. Industrial and Engineering Chemistry Research, 2017, 56 (13): 3477-3502.

[116] D. Li, X. Duan, H. Sun, J. Kang, H. Zhang, M.O. Tade, S. Wang, Facile synthesis of nitrogen-doped graphene via low-temperature pyrolysis: the effects of precursors and annealing ambience on metal-free catalytic oxidation[J]. Carbon, 2017, 115 649-658.

[117] J. Wu, D. Zhang, Y. Wang, B. Hou, Electrocatalytic activity of nitrogen-doped graphene synthesized via a one-pot hydrothermal process towards oxygen reduction reaction[J]. Journal of Power Sources, 2013, 227 185-190.

[118] N.I. Kovtyukhova, P.J. Ollivier, B.R. Martin, T.E. Mallouk, S.A. Chizhik, E.V. Buzaneva, A.D. Gorchinskiy, Layer-by-layer assembly of ultrathin composite films from micron-sized graphite oxide sheets and polycations[J]. Chemistry of Materials, 1999, 11 (3): 771-778.

[119] H.-L. Guo, P. Su, X. Kang, S.-K. Ning, Synthesis and characterization of nitrogen-doped graphene hydrogels by hydrothermal route with urea as reducing-doping agents[J]. Journal of Materials Chemistry A, 2013, 1 (6): 2248-2255.

[120] X. Bai, Y. Shi, J. Guo, L. Gao, K. Wang, Y. Du, T. Ma, Catalytic activities enhanced by abundant structural defects and balanced N distribution of N-doped graphene in oxygen reduction reaction[J]. Journal of Power Sources, 2016, 306 85-91.

[121] L. Lai, J.R. Potts, D. Zhan, L. Wang, C.K. Poh, C. Tang, H. Gong, Z. Shen, J. Lin, R.S. Ruoff, Exploration of the active center structure of nitrogen-doped graphene-based catalysts for oxygen reduction reaction[J]. Energy and Environmental Science, 2012, 5 (7): 7936-7942.

[122] C. Vallés, J. David Núñez, A.M. Benito, W.K. Maser, Flexible conductive graphene paper obtained by direct and gentle annealing of graphene oxide paper[J]. Carbon, 2012, 50 (3): 835-844.

[123] L. Sun, L. Wang, C. Tian, T. Tan, Y. Xie, K. Shi, M. Li, H. Fu, Nitrogen-doped graphene with high nitrogen level via a one-step hydrothermal reaction of graphene oxide with urea for superior capacitive energy storage[J]. RSC Advances, 2012, 2 (10): 4498-4506.

[124] X. Zeng, Z. Wang, N. Meng, D.T. McCarthy, A. Deletic, J.-h. Pan, X. Zhang, Highly dispersed TiO_2 nanocrystals and carbon dots on reduced graphene oxide: ternary nanocomposites for accelerated photocatalytic water disinfection[J]. Applied Catalysis B: Environmental, 2017, 202 33-41.

[125] C. Huang, C. Li, G. Shi, Graphene based catalysts[J]. Energy and Environmental Science, 2012, 5 (10): 8848-8868.

[126] Z. Lin, Y. Liu, Y. Yao, O.J. Hildreth, Z. Li, K. Moon, C.-p. Wong, Superior capacitance of functionalized graphene[J]. The Journal of Physical Chemistry C, 2011, 115 (14): 7120-7125.

[127] T. Lin, F. Huang, J. Liang, Y. Wang, A facile preparation route for boron-doped graphene, and its CdTe solar cell application[J]. Energy and Environmental Science, 2011, 4 (3): 862-865.

[128] C. Zhu, H. Li, S. Fu, D. Du, Y. Lin, Highly efficient nonprecious metal catalysts towards oxygen reduction reaction based on three-dimensional porous carbon nanostructures[J]. Chemical Society Reviews, 2016, 45 (3): 517-531.

[129] J. Tang, J. Liu, C. Li, Y. Li, M.O. Tade, S. Dai, Y. Yamauchi, Synthesis of nitrogen-doped mesoporous carbon spheres with extra-large pores through assembly of diblock copolymer micelles[J]. Angewandte Chemie-International Edition, 2015, 54 (2): 588-593.

[130] Y. Wang, H. Liu, K. Wang, S. Song, P. Tsiakaras, 3D interconnected hierarchically porous N-doped carbon with NH_3 activation for efficient oxygen reduction reaction[J]. Applied Catalysis B: Environmental, 2017, 210 57-66.

[131] S.-S. Li, H.-P. Cong, P. Wang, S.-H. Yu, Flexible nitrogen-doped graphene/carbon nanotube/Co_3O_4 paper and its oxygen reduction activity[J]. Nanoscale, 2014, 6 (13): 7534-7541.

[132] L. Zhang, Z. Xia, Mechanisms of oxygen reduction reaction on nitrogen-doped graphene for fuel cells[J]. The Journal of Physical Chemistry C, 2011, 115 (22): 11170-11176.

[133] R. Chen, H. Li, D. Chu, G. Wang, Unraveling oxygen reduction reaction mechanisms on carbon-supported Fe-phthalocyanine and Co-phthalocyanine catalysts in alkaline solutions[J]. The Journal of Physical Chemistry C, 2009, 113 (48): 20689-20697.

[134] M. Hu, Z. Yao, L. Li, Y.-H. Tsou, L. Kuang, X. Xu, W. Zhang, X. Wang, Boron-doped graphene nanosheet-supported Pt: a highly active and selective catalyst for low temperature H_2-SCR[J]. Nanoscale, 2018, 10 (21): 10203-10212.

[135] H. Li, B. Liu, Y. Wang, S. Yin, X. Ma, X. Wang, Q. Wu, R. shen, H. Chen, A facile one-step hydrothermal synthesis of a B-doped graphene/rod-shaped TiO_2 nanocomposite[J]. RSC Advances, 2014, 4 (72): 37992-37997.

[136] Y. Yang, J. Zhang, X. Wu, Y. Fu, H. Wu, S. Guo, Composites of boron-doped carbon nanosheets and iron oxide nanoneedles: fabrication and lithium ion storage performance[J]. Journal of Materials Chemistry A, 2014, 2 (24): 9111-9117.

[137] D.Y. Usachov, A.V. Fedorov, A.E. Petukhov, O.Y. Vilkov, A.G. Rybkin, M.M. Otrokov, A. Arnau, E.V. Chulkov, L.V. Yashina, M. Farjam, V.K. Adamchuk, B.V. Senkovskiy, C. Laubschat, D.V. Vyalikh, Epitaxial B-graphene: large-scale growth and atomic structure[J]. ACS Nano, 2015, 9 (7): 7314-7322.

[138] J. Guerrero-Contreras, F. Caballero-Briones, Graphene oxide powders with different oxidation degree, prepared by synthesis variations of the Hummers method[J]. Materials Chemistry and Physics, 2015, 153 209-220.

[139] C. Nethravathi, M. Rajamathi, Chemically modified graphene sheets produced by the solvothermal reduction of colloidal dispersions of graphite oxide[J]. Carbon, 2008, 46 (14): 1994-1998.

[140] Z.L. Wang, D. Xu, Y. Huang, Z. Wu, L.M. Wang, X.B. Zhang, Facile, mild and fast thermal-decomposition reduction of graphene oxide in air and its application in high-performance lithium batteries[J]. Chemical Communications, 2012, 48 (7): 976-978.

[141] D. Wei, Y. Liu, Y. Wang, H. Zhang, L. Huang, G. Yu, Synthesis of N-doped graphene by chemical vapor deposition and its electrical properties[J]. Nano Letters, 2009, 9 (5): 1752-1758.

[142] T. Humberto, L. Ruitao, T. Mauricio, S.D. Mildred, The role of defects and doping in 2D graphene sheets and 1D nanoribbons[J]. Reports on Progress in Physics, 2012, 75 (6): 062501.